Precision measurements of $\sin(2\beta)$ with the LHCb experiment

Dissertation
zur Erlangung des akademischen Grades
Dr. rer. nat.

vorgelegt von

Gerwin Meier
geboren in Kiel

Lehrstuhl für Experimentelle Physik V
Fakultät Physik
Technische Universität Dortmund
2023

Der Fakultät Physik der Technischen Universität Dortmund zur Erlangung des akademischen Grades eines Doktors der Naturwissenschaften vorgelegte Dissertation.

Ursprünglicher Betreuer: Prof. Dr. B. Spaan

1. Gutachter: Prof. Dr. J. Albrecht
2. Gutachter: Dr. C. Delitzsch

Vorsitzender der Prüfungskommission: Prof. Dr. H. Hövel
Vertreter der wissenschaftlichen Mitarbeiter*innen: Dr. C. Sternemann

Datum des Einreichens der Arbeit: 06.12.2023
Datum der mündlichen Prüfung: 15.03.2024

Abstract

High-precision measurements of observables of the Standard Model of particle physics, like the CKM matrix parameters, are key to answering the open questions of particle physics. The most precise CKM angle $\sin(2\beta)$ can be optimally determined by a decay-time dependent measurement of *CP* violation in $B^0 \to \psi K^0_S$ decays. In this thesis data from $B^0 \to J/\psi(\to \mu\mu)K^0_S$, $B^0 \to \psi(2S)(\to \mu\mu)K^0_S$ and $B^0 \to J/\psi(\to ee)K^0_S$ decays is analysed with $K^0_S \to \pi^+\pi^-$ collected at a centre-of-mass energy of $\sqrt{s} = 13$ TeV with *pp* collisions by the LHCb experiment between 2015 and 2018. The data corresponds to an integrated luminosity of $6\,\mathrm{fb}^{-1}$ and results in the combination of all three decays for the *CP* violation parameters in

$$\begin{aligned} S_{\psi K^0_S} &= 0.717 \pm 0.013\,(\text{stat.}) \pm 0.008\,(\text{syst.})\,, \\ C_{\psi K^0_S} &= 0.008 \pm 0.012\,(\text{stat.}) \pm 0.003\,(\text{syst.})\,, \end{aligned}$$

where S corresponds to $\sin(2\beta)$. This is consistent with the Standard Model predictions and with previous measurements. Furthermore, this is the most precise single measurement and more precise than the current world average.

Zusammenfassung

Hochpräzessionsmessungen von Observablen des Standardmodells der Teilchenphysik, wie die Parameter der CKM-Matrix, sind entscheidend, um offene Fragen der Teilchenphysik zu beantworten. Der am genauesten gemessene CKM Winkel $\sin(2\beta)$ kann optimal gemessen werden mit Zerfallszeit-abhängigen *CP*-verletzenden Messungen in $B^0 \to \psi K^0_S$ Zerfällen. In dieser Arbeit wurden Daten von $B^0 \to J/\psi(\to \mu\mu)K^0_S$, $B^0 \to \psi(2S)(\to \mu\mu)K^0_S$ und $B^0 \to J/\psi(\to ee)K^0_S$ Zerfällen mit $K^0_S \to \pi^+\pi^-$ analysiert. Diese wurden aufgenommen bei einer Schwerpunktsenergie von $\sqrt{s} = 13$ TeV mit *pp* Kollisionen am LHCb-Experiment zwischen 2015 und 2018. Die Daten entsprechen einer integrierten Luminosität von $6\,\mathrm{fb}^{-1}$ und resultieren in der Kombination von allen drei Zerfällen für die *CP*-verletzenden Parameter in

$$\begin{aligned} S_{\psi K^0_S} &= 0.717 \pm 0.013\,(\text{stat.}) \pm 0.008\,(\text{syst.})\,, \\ C_{\psi K^0_S} &= 0.008 \pm 0.012\,(\text{stat.}) \pm 0.003\,(\text{syst.})\,, \end{aligned}$$

wobei S $\sin(2\beta)$ entspricht. Das ist konsistent mit den Vorhersagen des Standardmodells und vorherigen Messungen. Die Messung erreicht die größte Genauigkeit einer Einzelmessung und ist genauer als der Weltmittelwert.

Contents

1 Introduction

To understand how macroscopic objects work, it is usually helpful to look into the smallest parts of the objects. For example, from the outside, it is not apparent how the mechanism of a mechanical watch, called calibre, and the hands' movement are operating. However, a closer look at the smallest parts within the watch, the mainspring, the wheel train out of gears, a balance wheel analogous to a pendulum and the screws to fix everything in its place, gives insight into the functionality. The same can be applied to our universe. The smallest parts are the quarks, leptons and gauge bosons. Analogous to the instruction manual the Standard Model of particle physics (SM) is the fundamental theory to describe these particles and their interactions [1–5]. This way, it provides insights into how the smallest parts of the universe operate and behave.

The SM was developed in the middle of the 20th century and has been tested throughout all aspects. The predictions of the SM, like the broken charge (C) symmetry and charge-parity (CP) symmetry [6,7] or that the hadrons are composed of quarks [8,9], could be verified. Moreover, all described particles were measured, lately the top quark [10,11], the tau neutrino [12] and the Higgs boson [13,14]. No other fundamental particles were found and observables were measured to a stunning precision of up to 10^{-9}, *e.g.* the branching fraction of $B_s^0 \to \mu\mu$ decays [15,16].

However, some aspects of nature cannot be explained by the SM, *e.g.* gravitation is not included. Therefore, the predictions are only valid for small masses and cannot expanded to the macroscopic world. Furthermore, the mass of neutrinos, which was found in the oscillation of solar neutrinos [17–19], is not described and the SM only accounts for 5 % of the observable energy in the universe [20]. The other 95 % can be divided into dark matter with 27 % and dark energy with 68 %. There is no candidate in the SM yet to account for the dark matter, which is needed to explain the rotation curves of some galaxies, and no fundamental force can describe the dark energy, which is needed to explain the accelerated expansion of the universe [21,22]. Another open question is the baryon or matter-antimatter asymmetry [23]. No antimatter clusters are observed until today and the whole universe is built out of matter. However, 13.8 billion years ago, in the Big Bang [24], an equal amount of matter and antimatter was created. The procedure of a matter-antimatter asymmetry can be explained by $C\!P$ violation [25], but the amount of $C\!P$ violation in the SM is too small to be the only explanation for the observed amount of matter left in the universe.

Due to all these open questions, extending the SM and searching for physics beyond the Standard Model (BSM) is necessary. There are two general ways to look for BSM with accelerators: direct or indirect searches. In direct searches, the new particles are produced directly, which means that the energy delivered by the particle accelerator has to be at least as high as the mass of these particles. In most BSM theories, the new particles' mass is in the magnitude of TeV or higher [26]. The largest particle accelerator, the Large Hadron Collider (LHC), has at the moment a centre-of-mass energy of 13.6 TeV. In addition, there are plans to build a new particle accelerator with increased energy of around 100 TeV beginning in the middle of 2040 or later [27,28]. The upside of direct searches is that the properties of new particles can be measured directly. However, the downside is that every increase in energy is very expensive, costing tens of billions. Indirect searches use a different approach, where new particles are produced only virtually in the decay chain of particles. The properties of observables slightly change in the presence of these new particles, which can be detected in high-precision measurements. The virtual particles can have higher energies due to Heisenberg's uncertainty principle if they interact on a tiny time frame [29], which already today allows for a sensitivity of a few 100 TeV. Due to the reach of these higher energies for possible new particles, precision measurements are the best opportunity to find differences between experimental results and theoretical predictions of the SM. These differences are then hints where the current theory can be improved.

One topic of possible precision measurements is the matter-antimatter asymmetry. This asymmetry can partly be described by *CP* violation, which is introduced in the SM in the Cabibbo-Kobayashi-Maskawa matrix (CKM) [30,31]. One observable of this CKM matrix is the angle β or $\sin(2\beta)$. Precision measurements of this observable allow to determine the amount of *CP* violation and check whether the current model is correct. The decay channel that both from the experimental and from the theoretical point of view is most sensitive to $\sin(2\beta)$ is $B^0 \to \psi K^0_S$ since it has a high statistic with a clear and efficient selection, can be calculated perturbatively and mainly depends on $\sin(2\beta)$ alone.

The LHCb detector at the LHC is designed and well equipped for precision measurements, especially for $B^0 \to \psi K^0_S$ decays. This is primarily due to the excellent particle identification and high vertex resolution. Previous measurements used the data collected in the first data-taking period (Run 1) between 2011 and 2012 [32,33] and achieved a slightly smaller sensitivity than the measurements by the BaBar and Belle experiments [34,35] at the e^+e^- colliders. The results between the LHCb experiment and the e^+e^- colliders differ by almost 2σ. Therefore, the result from the data recorded in the second data-taking period (Run 2) between 2015 and 2018 by the LHCb experiment presented in this thesis can give insights into whether there is a fundamental difference between these experiments or a statistical fluctuation. The data was collected at a centre-of-mass energy of 13 TeV and corresponds to an integrated luminosity of 6 fb^{-1}, which doubles the amount of data analysed in the previous LHCb measurements.

The theoretical properties of all fundamental particles and their interactions are described at the beginning of this thesis in Ch. 2. Furthermore, the symmetries in the SM, the CKM matrix including the *CP* violation types, the time evolution of neutral hadrons and the unique properties of $B^0 \to \psi K^0_S$ decays are explained in this chapter. The basics of the theoretical background are completed with a short description of the LHCb detector as well as the handling and simulation of the huge data samples in Ch. 3. An overview of the analysed data and the strategy is described in Ch. 4, while in Ch. 5 a description of the selection of signal and background data is given. The model for the invariant mass of the B^0 mesons is discussed in Ch. 6, including an estimate of the number of signal decays in the data. The description of the decay time is included in Ch. 7, while the flavour tagging, the determination of whether the initial particle is a particle or anti-particle, is described in Ch. 8. The extraction of the *CP* violation parameters is explained in Ch. 9 and the determination of the systematic uncertainties as well as cross-checks of the results are given in Ch. 10. In the end, in Ch. 11, a combination of the *CP* violation parameters of all three decay channels is described as well as a combination with previous measurements of the LHCb experiment. Finally, the thesis is concluded in Ch. 12 with a summary of the whole analysis and an outlook of future measurements.

Author's contribution to the analysis

Particle physics analyses are based on joint efforts from a team of analysts. This results in papers with over 1000 authors in the LHCb experiment. In important measurements, working in a team of 10 to 20 people from various international institutes in close collaboration is common. The analysis presented in this thesis is worked on in a smaller team only at the technical university in Dortmund with mainly three persons. The author's colleagues were Patrick Mackowiak and Vukan Jévtic, resulting in a doctoral thesis [36] and a doctoral thesis in preparation [37]. To understand the entire analysis, not only the parts the author mainly worked on, but also the other aspects of the analysis are discussed. The author's main contributions are the aspects of the $B^0 \to J/\psi(\to ee)K^0_S$ decays, the time-dependent selection and reconstruction efficiency, the portability check of prompt decays to signal decays, the evaluation of the systematic uncertainties and various cross-checks with different assumptions for the CP violation model. Other parts, like the implementation of the CP violation model or the interpretation of the results, were prepared together.

The analysis is published in the Physics Review Letter journal [38].

2 The Standard Model of particle physics

The Standard Model is today's most accurate theory to describe elementary particles and their interactions. It describes three of the four fundamental forces in the universe, namely the electromagnetic, the weak and the strong forces and its measurements reach one of the highest precision within all physics fields. However, some observations cannot be described by the SM, *e.g.* the matter-antimatter asymmetry or the presence of dark matter and dark energy, which accounts for 95 % of the energy balance in the universe [20–23, 25]. The analysis presented in this thesis study one aspect of the matter-antimatter asymmetry. Therefore, a short introduction about the theory and the particles described by the SM is given in this chapter. More detailed information about all aspects of the SM can be found in Refs [1, 2] and the specific details about *CP* violation are given in Refs. [3–5].

The description of the SM starts with the fundamental particles and interactions in Sec. 2.1, followed by a short introduction of relevant symmetries in this thesis in Sec. 2.2. The quark mixing matrix is introduced in Sec. 2.3, while the time evolution of neutral B^0 mesons is described in Sec. 2.4. In Sec. 2.5 the three types of *CP* violation are explained and in the end in Sec. 2.6 specific details about the analysed decay $B^0 \to \psi K^0_S$ and why this decay is optimal to search for the matter-antimatter asymmetry are discussed.

2.1 Fundamental particles and their interactions

The elementary particles described in the SM can be seen in Fig. 2.1. For each of the twelve elementary fermions, spin $^1/_2$ particles presented in red and green on the left side, an anti-particle exists with opposite charge-related quantum numbers. The fermions contain six quarks and six leptons. The six quarks can be divided into three generations, each with one up-type and one down-type quark, where the generations are differentiated by the mass of the quarks. The quarks are called up-quark (u), down-quark (d), charm-quark (c), strange-quark (s), top-quark (t) and bottom-quark (b). Each quark has one of three colour charge types: red, blue and green. Via this colour charge, the quarks couple to the strong force and thus to one of the eight gluons (g). The gluons are bosons, spin one particles marked in blue in Fig. 2.1, and the mediators of the strong interaction. They have one colour and one anti-colour charge and are the only particles except for the Higgs boson, which have a self-interaction. All quarks always form a bounded state with no colour

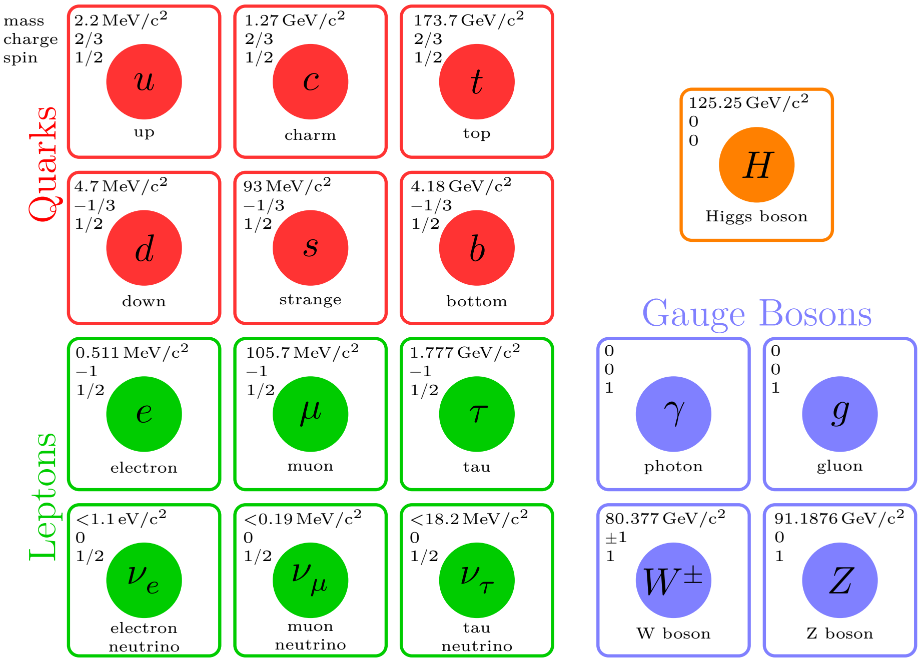

Figure 2.1: All fundamental particles and their interaction bosons with their mass, charge and spin. Layout taken from Ref. [39] and numbers from Ref. [40]

charge left, a so-called hadron, due to the strong interaction. This phenomenon is called confinement [41]. The most common hadrons are the mesons formed by one quark and one anti-quark and baryons formed by three quarks or anti-quarks. Nevertheless, tetraquarks and pentaquarks with four or five quarks were observed, too; see, for example, Ref. [42, 43]. The electric charge of the up-type quarks is ${}^{2}\!/\!{}_{3}e$ with the elementary charge e and of the down-type quarks $-{}^{1}\!/\!{}_{3}e$. This way, the hadrons always have an integer electric charge. The six leptons can be classified into three charged particles, the electron (e), muon (μ) and tauon (τ), and three neutral particles, the corresponding neutrinos (ν_e, ν_μ, ν_τ). The mediator of the electromagnetic force is the massless photon (γ), a spin one boson, and couples to the electric charge. The massive W^+, W^- and Z bosons with spin one are the mediators of the weak interactions, which couple to the weak hypercharge of all twelve fermions. The last particle described in the SM is the Higgs boson with spin zero, in orange in Fig. 2.1. It was discovered in 2012 [13, 14] and is the mediator of the Higgs field. It is introduced due to the Higgs mechanism [44], which explains the mass of the fermions and bosons through the Yukawa interaction.

An intuitive and easy way to illustrate processes of fundamental particles and their interactions are Feynman diagrams [45]. In these diagrams, each type of the fundamental particles and each mathematical rule of their interaction is drawn differently such that these diagrams visualise the mathematical instructions to calculate the probability amplitudes. Furthermore, it is possible to see at first glance, which processes are more likely than others. One of the most simple examples can be seen in Fig. 2.2, where an u quark decays into a d quark under emission of a charged W^+ meson. The decay rate probability of this process is proportional to the square of the electric charge constant e and the coupling of a u and d quark, which is roughly one.

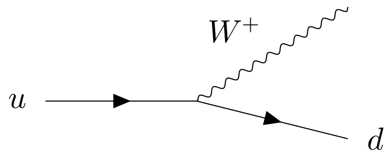

Figure 2.2: Feynman graph for an u quark decaying into a d quark under emission of a W^+ meson

2.2 Symmetries

Symmetries play a vital role in the understanding and developing of the SM because it is possible to predict observables from other measurements and thus, review different results. For example, due to the flavour symmetry, the light u, d and s quarks are interchangeable for the strong force, also called invariant under the flavour symmetry. This helps to interpret results because the amplitudes of decay channels involving these light quarks have a particular relation towards each other. With these relations, it is possible to entangle observables measured in two different decay channels like the branching fraction, the probability for a particle to decay into the given final state. Therefore, predicting the branching fraction of one decay channel from another is possible, while any deviation would be a sign of physics beyond the SM.

Important in the development of the SM are the three discrete symmetries parity operation (P), charge conjugation (C) and time reversal (T). The parity operation inverses all spatial coordinates like

$$P\psi(\vec{r},t) = \psi(-\vec{r},t).$$

In contrast, the charge conjugation transforms all charge-related quantum numbers and thus changes a particle into its anti-particle

$$C|p\rangle = |\overline{p}\rangle$$

and the time reversal inverse the time

$$T\psi(t) = \psi(-t).$$

In the past, it was thought that all forces would be invariant under parity as it is the case for the strong and electromagnetic forces. The thought is intuitive because a parity transformation of our world can be seen as a world in a mirror and in our macroscopic world a mirrored image is interpreted as normal. However, in 1956 it was found that the weak interaction violates the parity symmetry [6]. This was honoured by a noble prize the year later. This also means that the charge conjugation is violated in the weak interaction. But still, it was postulated that the combination of both symmetries would remain symmetric for the weak interaction [46]. Nevertheless, in 1964 it was found that the weak force is not invariant under a $\mathcal{CP}$ transformation [7], which also resulted in a noble prize. In the SM only the combination of all three discrete symmetries, the CPT symmetry, is invariant, which leads to the same mass of particles and anti-particles [47–49].

2.3 Quark mixing

All quarks can change their flavour via the weak interaction under the emission of a charged W boson. The rate of this process is proportional to one element of the CKM matrix. For example, the process in Fig. 2.2 is proportional to V_{ud}. The CKM matrix is the link between the weak force eigenstates, denoted with a prime, and the mass eigenstates of the quarks. It can be written as

$$\begin{pmatrix} d' \\ s' \\ b' \end{pmatrix} = \begin{pmatrix} V_{ud} & V_{us} & V_{ub} \\ V_{cd} & V_{cs} & V_{cb} \\ V_{td} & V_{ts} & V_{tb} \end{pmatrix} \begin{pmatrix} d \\ s \\ b \end{pmatrix} . \tag{2.1}$$

A complex 3×3 matrix has 18 free parameters, but due to its unitarity and five relative phases between the six quark fields, it can be described with only four different parameters, *e.g.* three angles $\varPhi_1$, $\varPhi_2$, $\varPhi_3$ and one complex phase δ. The complex phase is mandatory for all $\mathcal{CP}$ violating processes. With these four parameters and the abbreviations $c_i = \cos(\varPhi_i)$ and $s_i = \sin(\varPhi_i)$ the CKM matrix can be expressed as

$$V_{\text{CKM}} = \begin{pmatrix} c_1 & -s_1 c_3 & -s_1 s_3 \\ s_1 c_2 & c_1 c_2 c_3 - s_2 s_3 e^{i\delta} & c_1 c_2 s_3 + s_2 c_3 e^{i\delta} \\ s_1 s_2 & c_1 s_2 c_3 + c_2 s_3 e^{i\delta} & c_1 s_2 s_3 - c_2 c_3 e^{i\delta} \end{pmatrix} . \tag{2.2}$$

A more common parametrisation is introduced by Wolfenstein [50] in terms of $\alpha = V_{us} \approx 0.22$

$$V_{\text{CKM}} = \begin{pmatrix} 1-\alpha^2/2 & \alpha & \alpha^3 A\,(\rho - i\eta) \\ -\alpha & 1-\alpha^2/2 & \alpha^2 A \\ \alpha^3 A\,(1-\rho-i\eta) & -\alpha^2 A & 1 \end{pmatrix} + \mathcal{O}(\alpha^4). \tag{2.3}$$

It is highly hierarchic with nearly unity at the main diagonal and strongly decreasing values of the entries towards the off-diagonals. The three independent unitary conditions $\sum_i = V_{ij} V_{ik}^* = 0$ with $j \neq k$ can be represented as triangles in the complex $\overline{\rho} - \overline{\eta}$ plane with the relation to the Wolfenstein parameter α as

$$\overline{\rho} = \rho(1 - \alpha^2/2), \tag{2.4}$$
$$\overline{\eta} = \eta(1 - \alpha^2/2). \tag{2.5}$$

The area of these triangles expresses the amount of *CP* violation in the SM [51, 52]. Although the area for these triangles is always the same, the ratio of the side lengths differs significantly. Therefore, it is useful to use the condition

$$V_{ud}V_{ub}^* + V_{cd}V_{cb}^* + V_{td}V_{tb}^* = 0, \tag{2.6}$$

where all sides and angles are of comparable size. Normalised to $V_{cd}V_{cb}^*$ the triangle can be seen in Fig. 2.3. The angles are defined as

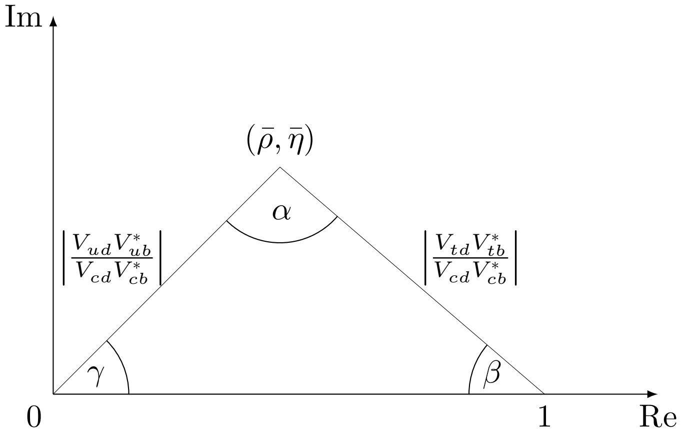

Figure 2.3: Schematic view of the CKM triangle in the complex plane using the unitary condition from Eq. (2.6).

$$\alpha = \arg\left(-\frac{V_{td}V_{tb}^*}{V_{ud}V_{ub}^*}\right), \tag{2.7}$$

$$\beta = \arg\left(-\frac{V_{cd}V_{cb}^*}{V_{td}V_{tb}^*}\right), \tag{2.8}$$

$$\gamma = \arg\left(-\frac{V_{ud}V_{ub}^*}{V_{cd}V_{cb}^*}\right). \tag{2.9}$$

With experimental measurements the side lengths and angles can be determined such that the triangle is overconstrained. Therefore, measurements of these parameters are perfect candidates to test the SM as a not closing triangle would violate the unitarity of the CKM triangle which is a clear sign for new physics.

2.4 Time evolution of neutral B^0 mesons

The time evolution of an initial B^0 ($\overline{B}^0$) state is described by the Schrödinger equation [53–55] as

$$i\frac{d}{dt}\begin{pmatrix}|B^0(t)\rangle\\|\overline{B}^0(t)\rangle\end{pmatrix} = \left(\boldsymbol{M} - \frac{i}{2}\boldsymbol{\Gamma}\right)\begin{pmatrix}|B^0(t)\rangle\\|\overline{B}^0(t)\rangle\end{pmatrix}, \tag{2.10}$$

where $\boldsymbol{M}$ is the mass matrix and $\boldsymbol{\Gamma}$ is the decay matrix. The mass and lifetime of B^0 and $\overline{B}^0$ mesons are the same due to the *CPT* invariance, which leads to the same diagonal entries of $\boldsymbol{M}$ and $\boldsymbol{\Gamma}$. The non-zero off-diagonal elements allow for the oscillation between B^0 and $\overline{B}^0$ mesons, also called mixing. With this, the mass eigenstates B^0_{H} and B^0_{L} are defined as

$$|B^0_{\mathrm{H}}\rangle = p|B^0\rangle - q|\overline{B}^0\rangle, \tag{2.11}$$

$$|B^0_{\mathrm{L}}\rangle = p|B^0\rangle + q|\overline{B}^0\rangle, \tag{2.12}$$

with the mixing parameters

$$\frac{q}{p} = \frac{\Delta m + \frac{i}{2}\Delta\Gamma}{2(M_{12} - \frac{i}{2}\Gamma_{12})}. \tag{2.13}$$

The mean and difference of the mass and decay width are defined as

$$\Delta m = m_{\mathrm{H}} - m_{\mathrm{L}}, \tag{2.14}$$

$$\Delta\Gamma = \Gamma_{\mathrm{L}} - \Gamma_{\mathrm{H}}, \tag{2.15}$$

$$m = \frac{m_{\mathrm{H}} + m_{\mathrm{L}}}{2}, \tag{2.16}$$

$$\Gamma = \frac{\Gamma_{\mathrm{L}} + \Gamma_{\mathrm{H}}}{2}. \tag{2.17}$$

The mass difference Δm can be interpreted as the mixing frequency, while the width difference $\Delta\Gamma$ is negligible in the B^0 system. The time evolutions of the mass eigenstates are

$$|B_{\mathrm{L,H}}(t)\rangle = e^{-(im_{\mathrm{L,H}}+\Gamma_{\mathrm{H,L}}/2)t}|B_{\mathrm{L,H}}\rangle. \tag{2.18}$$

Using Eqs. (2.11) and (2.18) the time evolutions of the flavour eigenstates are defined as

$$|B^0(t)\rangle = g_+(t)|B^0\rangle + \frac{p}{q}g_-(t)|\overline{B}^0\rangle, \tag{2.19}$$

$$|\overline{B}^0(t)\rangle = \frac{p}{q}g_-(t)|B^0\rangle + g_+(t)|\overline{B}^0\rangle, \tag{2.20}$$

with

$$g_+(t) = e^{-imt}e^{-\Gamma t/2}\left[\cosh\frac{\Delta\Gamma t}{4}\cos\frac{\Delta m t}{4} - i\sinh\frac{\Delta\Gamma t}{4}\sin\frac{\Delta m t}{4}\right], \tag{2.21}$$

$$g_-(t) = e^{-imt}e^{-\Gamma t/2}\left[-\sinh\frac{\Delta\Gamma t}{4}\cos\frac{\Delta m t}{4} + i\cosh\frac{\Delta\Gamma t}{4}\sin\frac{\Delta m t}{4}\right]. \tag{2.22}$$

In experiments the *CP* violation parameters cannot measured directly. Only decay width differences can be detected. However, it is possible to calculate the *CP* violation parameters through the decay rates, the squared amplitudes. With the simplification for the mixing parameters and decay amplitudes of B^0 and $\overline{B}^0$ mesons

$$\lambda_f = \frac{q}{p}\frac{\overline{A}_f}{A_f} \tag{2.23}$$

and the *CP* observables

$$A_{\Delta\Gamma} = \frac{-2\,\mathrm{Re}\,\lambda_f}{1+|\lambda_f|^2}, \tag{2.24}$$

$$C_f = \frac{1-|\lambda_f|^2}{1+|\lambda_f|^2}, \tag{2.25}$$

$$S_f = \frac{2\,\mathrm{Im}\,\lambda_f}{1+|\lambda_f|^2} \tag{2.26}$$

the decay rates are given as

$$\begin{aligned}\Gamma(B^0(t)\to f) \propto{}& e^{\Gamma t}|A_f|^2(1+|\lambda_f|^2)\\ &\left[\cosh\frac{\Delta\Gamma t}{2} + \mathcal{A}_{\Delta\Gamma}\sinh\frac{\Delta\Gamma t}{2} + C_f\cos(\Delta m t) - S_f\sin(\Delta m t)\right],\end{aligned} \tag{2.27}$$

$$\begin{aligned}\Gamma(\overline{B}^0(t)\to f) \propto{}& e^{\Gamma t}|A_f|^2(1+|\lambda_f|^2)\left|\frac{p}{q}\right|^2\\ &\left[\cosh\frac{\Delta\Gamma t}{2} + \mathcal{A}_{\Delta\Gamma}\sinh\frac{\Delta\Gamma t}{2} - C_f\cos(\Delta m t) + S_f\sin(\Delta m t)\right].\end{aligned} \tag{2.28}$$

It can be seen that the decay rates depend on trigonometric functions of the mass and decay width difference. Each summand corresponds to a different property of the B^0 meson, *e.g.* the sin and sinh terms correspond to the interference between the direct decay of the B^0 meson and the decay after the oscillation to its anti-particle. In contrast, the cos and cosh terms correspond to decays with and without oscillation of the B^0 meson. This way, these decay rates depend nearly only on one term for specific decay channels.

2.5 Types of *CP* violation

CP violation can occur in three different states in the SM. First, direct *CP* violation, where the decay amplitude of a particle into a final state is different if all particles and anti-particles are swapped. The second type is the indirect *CP* violation, where the mass eigenstate of the particle is not the *CP* eigenstate. This leads to a different probability for mixing of neutral particles into their anti-particles and vice-versa. The third option is *CP* violation in the interference between the direct decay of a particle and the decay of that particle after oscillating into its anti-particle. Each type is explained in more detail in the following.

Direct *CP* violation

Direct *CP* violation is present if the decay amplitude A_f for a particle decaying into a final state f is different to the decay amplitude $\overline{A}_{\overline{f}}$ for the anti-particle decaying into the anti-particle final state $\overline{f}$. These decay amplitudes depend on two phases. The weak phase ϕ enters through the CKM matrix and has the opposite sign for both decays while the strong phase δ has the same sign for both decays. The two phases have to have different values, which can be seen in the squared decay amplitudes

$$\left|A_f\right|^2 - \left|\overline{A}_{\overline{f}}\right|^2 = -4\sum_i \sum_{i<j} |A_i| \left|A_j\right| \sin(\delta_i - \delta_j) \sin(\phi_i - \phi_j). \tag{2.29}$$

This type of *CP* violation was first observed in the kaon system [56], well studied in the B^0 system and recently discovered in the neutral charm sector [57]. Mixing of the initial states is not needed for the occurrence of direct *CP* violation. Therefore, it is the only type of *CP* violation that can be measured with charged particles.

Indirect *CP* violation

Indirect *CP* violation or *CP* violation in the mixing occurs when the mass eigenstates differ from the *CP* eigenstates and, therefore,

$$\left|\frac{q}{p}\right| \neq 1 \tag{2.30}$$

holds. More concrete is the fact that this also means that the probability that B^0 mesons oscillate into its anti-particle is the same as the probability that $\overline{B}^0$ mesons oscillate in B^0 mesons:

$$\mathcal{P}(B^0 \to \overline{B}^0, t) \neq \mathcal{P}(\overline{B}^0 \to B^0, t). \tag{2.31}$$

Indirect *CP* violation is observed in the kaon system [7] but the current sensitivity is not enough in the B^0 system, as it is highly suppressed in the SM.

CP violation in the interference of decay and decay after mixing

For decays, where the initial neutral particle and its anti-particle can decay into the same final state, another type of *CP* violation can occur. In this case, there are two different decay paths possible. Either the particle can decay directly ($B^0 \to f$) or first oscillate into its anti-particle and then decay into the final state ($B^0 \to \overline{B}^0 \to f$). If neither direct nor indirect *CP* violation is present, a relative phase between these two decay paths is still possible. This is called *CP* violation in the interference between decay and decay after mixing. Mathematically, this means that

$$\arg(\lambda_f) + \arg(\lambda_{\overline{f}}) \neq 0 \tag{2.32}$$

or for the case that the final state is a *CP* eigenstate, it is only necessary that

$$\mathrm{Im}(\lambda_{CP}) \neq 0 \tag{2.33}$$

holds. Experimentally, the *CP* violation can be determined with a time-dependent measurement with the form

$$A_{CP}(t) = \frac{\Gamma(\overline{B}^0(t) \to f_{CP}) - \Gamma(B^0(t) \to f_{CP})}{\Gamma(\overline{B}^0(t) \to f_{CP}) + \Gamma(B^0(t) \to f_{CP})} = \frac{S\sin(\Delta m t) - C\cos(\Delta m t)}{\cosh(\frac{\Delta\Gamma t}{2}) + \mathcal{A}_{\Delta\Gamma}\sinh(\frac{\Delta\Gamma t}{2})}. \tag{2.34}$$

With the approximation of no direct *CP* violation, $C = 0$, and $\Delta\Gamma = 0$, which is valid in the B^0 system, and the relation $S = \sin(2\beta)$ for the CKM angle β this leads to

$$A_{CP}(t) = \sin(2\beta)\sin(\Delta m t) \tag{2.35}$$

with a straightforward connection between a measured time-dependent asymmetry and the angle β of the CKM triangle.

2.6 The decay $B^0 \to \psi K^0_\mathrm{S}$

The best decay channel to measure the CKM angle β is $B^0 \to \psi K^0_\mathrm{S}$. This is the case because the decay is Cabibbo-favoured, meaning that it depends only on quadratically on the Wolfenstein parameter α, occurs at tree level, see Fig. 2.4, and the direct and indirect *CP* violation is suppressed. Furthermore, the final state is symmetrical and thus, a *CP* eigenstate and both the B^0 and $\overline{B}^0$ meson decay in the same final state. The *CP* violation is present in the interference between decay and decay after mixing. The K^0_S meson is not a flavour eigenstate and, therefore, does not occur in Fig. 2.4 but in the same way, as in the B^0 system, the K^0 and $\overline{K}^0$ mesons are the flavour eigenstates and in a superposition of the mass eigenstates

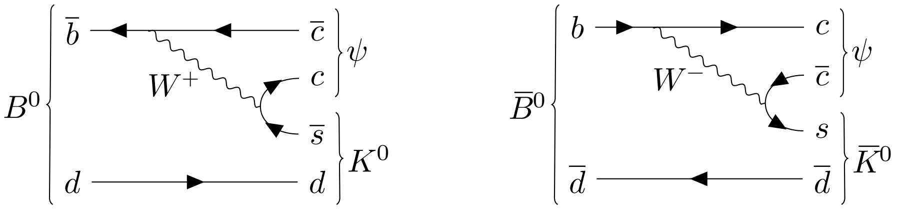

Figure 2.4: Feynman graph at tree level of $B^0 \to \psi K^0_\mathrm{S}$ and $\overline{B}^0 \to \psi K^0_\mathrm{S}$.

$$|K^0_\mathrm{S}\rangle = p_K|K^0\rangle - q_K|\overline{K}^0\rangle. \tag{2.36}$$

Using Eq. (2.13) and taking the involved CKM matrix elements into account the *CP* violation describing parameter simplifies to

$$\lambda_{\psi K^0_\mathrm{S}} = -\frac{V^*_{tb}V_{td}}{V_{tb}V^*_{td}}\frac{V^*_{cd}V_{cb}}{V_{cd}V^*_{cb}}. \tag{2.37}$$

Considering only tree level the absolute value of $\lambda_{\psi K^0_\mathrm{S}}$ is one and the real part is vanishing. Therefore, the *CP* parameters are given by

$$\mathcal{A}_{\Delta\Gamma} = 0, \tag{2.38}$$

$$C_{\psi K^0_\mathrm{S}} = 0, \tag{2.39}$$

$$S_{\psi K^0_\mathrm{S}} = \operatorname{Im}\lambda_{\psi K^0_\mathrm{S}} = \sin\left(\arg\left(-\frac{V^*_{tb}V_{td}}{V_{tb}V^*_{td}}\frac{V^*_{cd}V_{cb}}{V_{cd}V^*_{cb}}\right)\right) \tag{2.40}$$

$$= \sin\left[\arg\left(-\left(\frac{V^*_{cd}V_{cb}}{V_{tb}V^*_{td}}\right)^2\right)\right] = \sin 2\beta. \tag{2.41}$$

The simplification to take only tree level processes into account is valid up to 1° [58–60] for the value of β, which is near the current world average and therefore only an effective angle β_eff is measured

$$\beta_\mathrm{eff} = \beta + \Delta\beta. \tag{2.42}$$

The correction can be determined using the decays $B^0 \to J/\psi\pi^+\pi^-$ or $B^0_s \to \psi K^0_\mathrm{S}$, where higher-order effects of penguin contributions play a significant role. The B^0 and B^0_s meson decays are related due to the isospin or U-spin symmetry. In these symmetries the simplification is used that the mass of u and d quarks or d and s quarks is the same. The differences in the effective measurement of β can be used to constrain the parameter $\Delta\beta$.

Experimental status of quark mixing parameters

Besides, the measurement presented in this thesis of $\sin(2\beta)$ and its corresponding *CP* violation parameter $S_{\psi K^0_\mathrm{S}}$ are other measurements. For example within the LHCb experiment the data collected in 2011 and 2012 with the same three final states resulted in two published papers [32, 33] with the values 0.73 and around 0.83 for S in the $J/\psi(\to \mu\mu)K^0_\mathrm{S}$ and both other final states. The parameter C was compatible with 0 in all final states. The other two experiments with the most sensitivity are BaBar and Belle at SLAC and KEKB [61–63]. Both are e^+e^- colliders and operate at the $\Upsilon(4S)$ resonance, where dominantly $B^0\overline{B}^0$ pairs are produced. The results for the *CP* violation parameter S have a tension of nearly 2σ with the LHCb experiments [34, 35]. The statistical uncertainty limits all these measurements with a sensitivity of around 0.03 to 0.04 with the most sensitivity from the $J/\psi(\to \mu\mu)K^0_\mathrm{S}$ final state. The data collected between 2015 and 2018 by the LHCb experiment has around double the amount of the previous measurement, and the analysis plays an important role in solving the discrepancy.

Together with other measurements $\sin(2\beta)$ helps constrain the CKM triangle's shape since there are more independent measurements than parameters to characterise the CKM triangle fully. A global fit of all measurements and its uncertainties for the position of the apex is shown in Fig. 11.1.

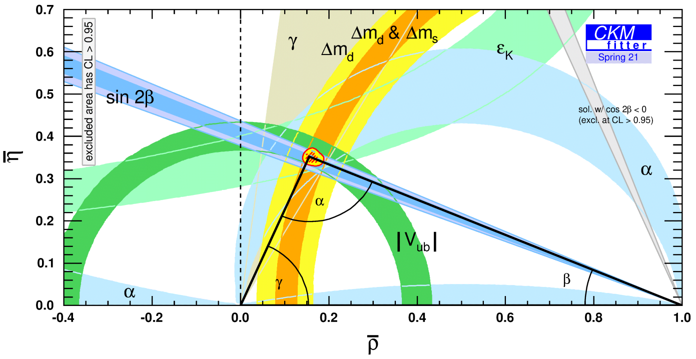

Figure 2.5: Unitarity triangle in the complex plane $(\bar{\rho}, \bar{\eta})$ with coloured constraints from measurements of various quantities taken from Ref. [64]. The red-shaded and yellow areas around the apex correspond to the 68% and 95% confidence levels of the combination.

The other parameters are measured for example in $B \to \pi\pi$ decays [65–67] for the angle α, in $B \to DK$ decays [68, 69] for γ and semileptonic b-hadron decays [70] and with the oscillation frequency of the B^0 and B_s^0 meson [71] for both sides.

If new measurements reveal that the apex is not closed, it would be a clear sign for physics beyond the SM as its unitarity is an integral property of the theory of *CP* violation and the weak interaction.

3 The LHCb experiment

The largest collaboration to study the fundamental particles and their exchanges is CERN, the European Organisation for Nuclear Research, near Geneva, Switzerland. The main experimental setup is the Large Hadron Collider (LHC), where protons are accelerated to nearly light speed and collide at four points with the main experiments ATLAS [72], ALICE [73], CMS [74] and LHCb [75]. The ATLAS and CMS experiments are mainly built to search for new particles, while the ALICE experiment is focused on quark-gluon plasma, the state of the universe few moments after its creation. In contrast, the LHCb experiment is focused on performing tests of the Standard Model of particle physics (SM), especially with hadrons containing b and c quarks. These tests include the search for rare decays and precision measurements of *CP*-violating processes. These are indirect measurements for New Physics beyond the Standard Model (BSM), which can be used to probe for heavy particles far beyond the current energy scales of any colliders.

The LHCb detector will be described briefly in Sec. 3.1 while an extended description is given in Ref. [75]. A short characterisation of the different track types inside the detector is given in Sec. 3.2 and the trigger system to reduce the amount of data which will be stored is discussed in Sec. 3.3. An overview of the used simulations concludes this chapter in Sec. 3.4.

3.1 The LHCb detector

In pp collisions with high energies B mesons are mainly produced by gg fusion with a huge boost in the forward or backward region. Therefore, the LHCb detector is built as a single-arm forward spectrometer covering only 4.5 % of the possible volume, which, however, accounts for around 25 % of all produced B mesons. In this way, the amount of available money can be better utilised to build more precise detector components and gain overall more suitable data. The LHCb detector can be seen in Fig. 3.1, with an angular acceptance in the horizontal plane from 10 to 300 mrad and in the vertical plane from 10 to 250 mrad, while the pseudorapidity range is $2 < \eta < 5$.

For physics analyses it is essential to determine which particles are detected and what the kinematic and topological properties are. Different parts of the detector are specialised to measure these properties. On the one hand, there are the subdetectors for the tracking, explained in Sec. 3.1.1, and on the other hand, the subdetectors for particle identification and energy measurement, shown in Sec. 3.1.2.

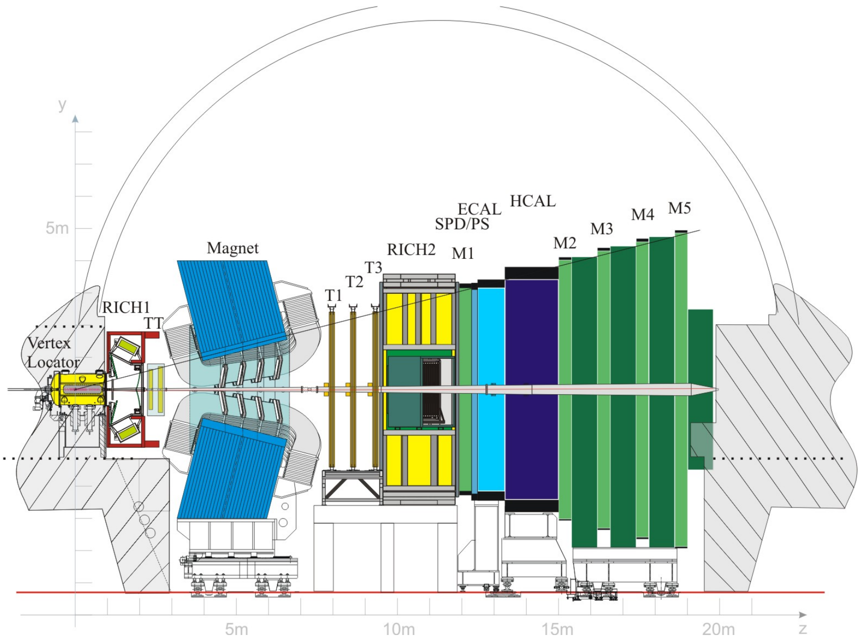

Figure 3.1: Schematic view on the LHCb detector in the yz-plane [75] with the abbreviation for each component explained in more detail in Sec. 3.1.1 and Sec. 3.1.2.

3.1.1 Track reconstruction

The primarily used subdetectors for particle tracking are the vertex locator (VELO), the Tracker Turicensis (TT), the magnet and the tracking stations (T1-T3). With 7 mm distance, the closest to the interaction point of the pp collision is the VELO. Its purpose is to detect the primary vertex (PV), the pp collision point, as well as the secondary vertex (SV), the point where the first created particles decay. This is used to measure the decay length, which can be used to differentiate between signal and background candidates efficiently. It comprises semi-circular silicon strip sensors measuring the polar coordinates' radius and the azimuthal angle. There are 42 half disks in total used plus four radial sensors to measure pile-up, the presence of multiple pp collisions at the same time. In Fig. 3.2 the layout of the 42 half disks as well as one single half disk is visible. To form a track it is necessary to contain at least three hits in the half disks, which corresponds to an acceptance of 15 to 300 mrad in the xz and yz plane. Charged particles ionise these semiconductor detectors and create electron-hole pairs. Under the presence of an electric field the free electrons and holes move to the anodes and cathodes and a measurable current is induced. Silicon strip detectors are used due to their radiation robustness, high accuracy and good resolution. The track finding efficiency is over 98 % and the PV resolution is 13 µm in the plane transverse to the beam and 71 µm along the beam. A decay time resolution of 50 fs is achieved as well as only 1 % of ghost track reconstructions, where a track is reconstructed based on background noise and without a corresponding real particle. The impact parameter (IP) is the shortest

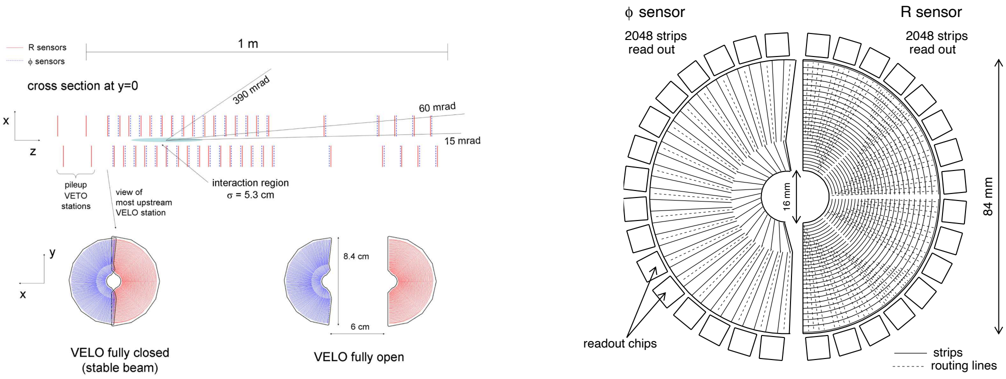

Figure 3.2: Schematic layout of the VELO subdetector on the left [75] and one half-disk of the VELO on the right [76].

distance between the PV and the trajectory of a particle. This is a good measure to distinguish particles originating from the PV or a different decay vertex, thus, signal from background particles. In the VELO its resolution of less than 35 µm with a transverse momentum (p_T) greater than 1 GeV/c is achieved [77, 78]. One peculiarity is that the VELO can be moved far away from the beam axis. This is used to be as close as possible to the beam during the data taking while minimising the radiation damage during the unstable beam conditions during the fill of the protons.

The beam conditions are permanently controlled by the beam condition monitor (BCM). It is built of two stations, upstream and downstream of the interaction point, with each eight radiation-hard diamond sensors. These sensors measure the particle flux and trigger a beam dump into a graphite block if it exceeds a threshold.

The TT is placed before the magnet and has the same detection type as the VELO with silicon strips. It has four layers with a ±5° rotation of the inner two layers in the xy-plane and a 30 cm gap in the middle. The foremost use cases are the transverse momentum measurement for the L0, see Sec. 3.3, the tracking of long-lived particles, which do not decay inside the VELO and of low momentum particles, which are bent out of the acceptance by the magnet. The achieved tracking efficiency is about 99.7 % and the track resolution around 53 µm [79].

The dipole magnet with a total length of 5 m and an integrated field strength of 4 T m bends charged particles in the x direction of the xz-plane, see Fig. 3.3 for the magnetic field along the z-axis for at different trajectories. This enables the determination of the momentum of the particles using the curvature radius. The field strength is chosen to enable a momentum resolution $\Delta p/p$ of 0.5 % for particles up to 20 GeV/c and 0.8 % up to 100 GeV/c [80]. The polarity is switched periodically to enable studies of possible charge-dependent detection asymmetries.

Last in the row of used subdetectors for the tracking are the tracking stations T1-T3. Each of these three stations consists like the TT of four layers, where the two middle ones are rotated by ±5 % in the vertical axis. Each layer is built of

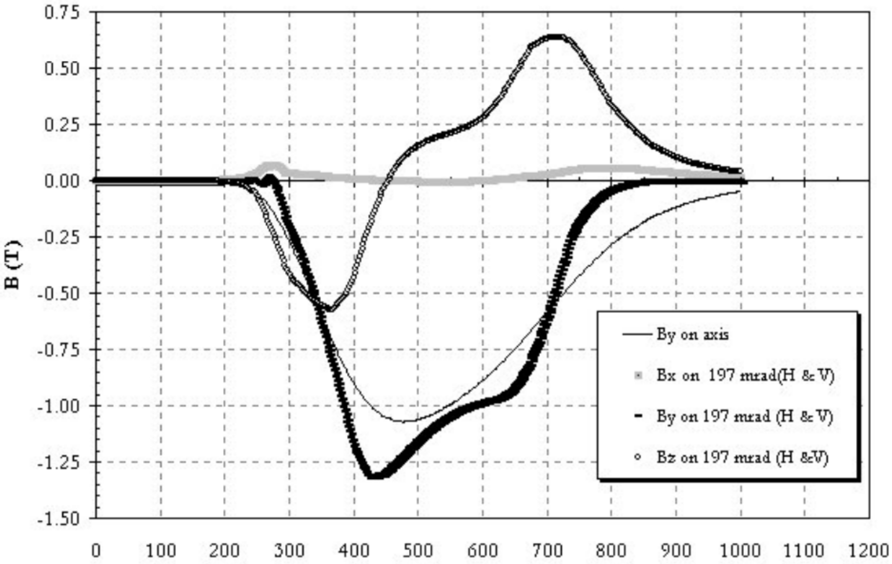

Figure 3.3: The strength of the magnetic field along the z-axis for particles at the y-axis and slightly off-centred at all three axes [81]. The strength in the x-axis is insignificant, and thus, a bending towards this axis is achieved.

two movable parts to have the possibility of maintenance and is split into the Inner Tracker (IT) and Outer Tracker (OT). The IT is again a silicon strip detector shaped like a cross around the beam pipe, which covers only 1.3 % of the sensitive area but 20 % of the produced charged particles. Its track efficiency is around 99.8 % and the track resolution is about 50 to 55 µm [78, 82]. The OT is build of straw drift tubes filled by 70 % Ar, 28.5 % CO_2 and 1.5 % O_2. The charged particles ionise the gas and the freed electrons move towards the anode at the centre of the straw with a voltage of 1550 V. The drift times of the electrons are proportional to the distance of the ionisation and in combination with the beam crossing signal time, the particle's position is determined. Each layer is filled with two times two staggered straw tube monolayers with a length of each 2.4 m. With 53760 straw tubes and an inner diameter of 4.9 cm an active area of 5971×4850 mm is achieved. The maximum drift resolution of 2.55 ns give a spatial resolution of 171 µm and a momentum resolution of 0.4 % [83].

3.1.2 Particle identification

For particle identification the ring-imaging cherenkov detectors (RICH1 and RICH2), the calorimeter system consisting of the scintillating pad detector (SPD), the preshower (PS) and the electromagnetic and hadronic calorimeter (ECAL and HCAL), as well as the muon stations (M1 - M5) are used. In the following, a more detailed description is given.

The two RICH detectors use the same procedure but are designed for two different momentum ranges of 1 to 60 GeV/c and 15 to 100 GeV/c, achieved by different gases, C_4F_{10} and CF_4 respectively. The underlying method is that particles with a higher velocity than the light in these gases emit photons in a specific angle θ_c. These photons are bent by a mirror system of spherical and plane mirrors to one of the 196 (RICH1) and 288 (RICH2) hybrid photodetectors (HPDs) [84]. The HPDs are maintained in a CO_2 atmosphere separated by quartz windows. They have a magnetic shield, which reduces the magnetic field from 60 mT down to 2.4 mT for RICH1 and from 15 mT down to between 0.2 and 0.6 mT in RICH2. The reduction of the magnetic field is necessary to prevent the electrons used in the HPDs from bending too much. The measured angle θ_c is anticorrelated to the refractive index n and the velocity

$$\cos(\theta_c) = \frac{1}{n\beta},$$

with $\beta = v/c$, equivalent to the momentum divided by the energy. In combination with the momentum measurement of the tracking detectors, the particle's energy and mass can be determined. With these information it is possible to identify the particle. It is primarily used to distinguish charged hadrons like pions, kaons and protons, but partly, it is also possible to detect charged muons. In Fig. 3.4 the distinguished reconstructed Cherenkov angles for different particles can be seen as a function of track momentum of recorded data in RICH1.

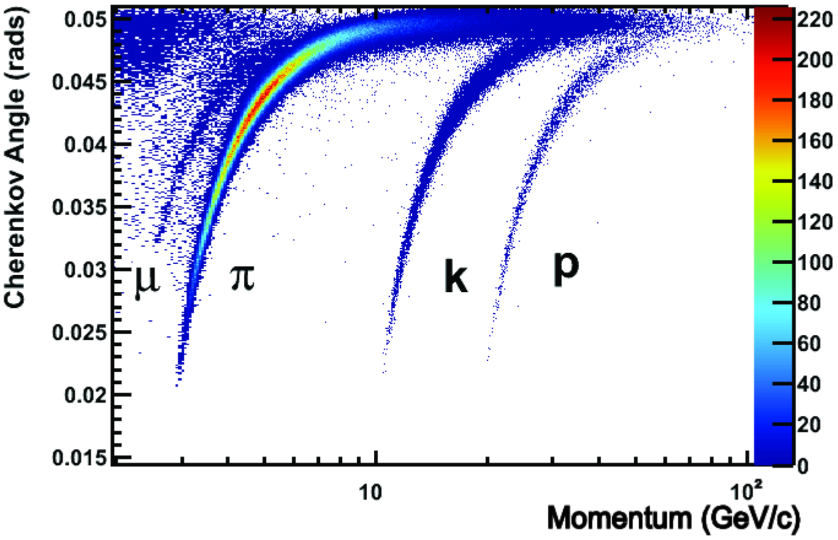

Figure 3.4: Reconstructed Cherenkov angle as a function of track momentum in the C_4F_{10} radiator of RICH1 [84]. Clear bands of protons, kaons and pions as well as a noisy band of muons are visible.

One of the five muon stations is placed after the RICH2 and the other ones are most downstream of the detector. In total, 1368 multi-wire proportional chambers (MWPCs) with an area of 435 m^2 are used [85]. The chambers are filled by 40 % Ar, 50 % CO_2 and 10 % CF_4. Each station can be divided into four regions with lower resolution in each region from inner to outer. The linear dimension of these regions is in the ratio of 1:2:4:8. A Granularity of 6 mm in the most inner region of M2 up to 62 mm in the second region of M5 is achieved. The pad segmentation in the bending horizontal plane is finer than in the vertical plane. After each of the stations M2, M3 and M4 80 cm thick iron absorbers are placed to ensure that only muons are detected in the last muon stations. Since muons interact so slightly with material, they are the only particles not stopped in these absorbers. That is why the latter muon stations provide an excellent way to identify muons. The first muon station after the RICH2 is installed to measure the transverse momentum. The MWPCs work similarly to the drift tubes of the OT. The muons ionise the gas, where one muon creates on average 50 free electrons, which drift to the wire due to the electric field. These electrons induce a negative current on the wire, proportional to the muon energy.

The calorimeter system is built as a succession of an absorber, where the particles deposit energy as photons, and a scintillating plane, where the photons are transmitted to photomultipliers (PMs). The purpose is to reconstruct precise kinematical parameters like energy and transverse energy. The SPD is 6.2×8.4 m long in x and y and 1.655 m deep in z [86]. It uses an iron absorber and mainly distinguishes between neutral and charged particles. The PS has the same size and structure as the SPD and distinguishes between electrons, photons and pions. This is done by the thin lead layer, where the pions produce only very few secondary particles; therefore, no extensive showers are detected compared to the electrons and photons. The difference between the latter two is the deposited energy of the charged electron through the PS. The ECAL is 6.3×7.8×0.835 m long in x, y and z and is divided into 3312 separate modules of square sections. It is split into three main sections with higher to lower granularity from closer to further away from the beam pipe. The shashlik technique with alternating lead absorber and scintillating fibres is repeated 66 times with a 120 µm TYVEC paper sheet separation. It distinguishes between electrons and hadrons and has an energy resolution of $(13.5 \pm 0.7)\,\%/\sqrt{\mathrm{E}} + (5.2 \pm 0.1)\,\% + (320 \pm 30)\,\mathrm{MeV/E}$ [86]. The HCAL is built with iron as absorbers and split into two sections closer and further away from the beam pipe. The dimensions are 6.8×8.4×1.655 m in x, y and z and in a first test beam, the resolution is measured to be $(67 \pm 5)\,\%/\sqrt{\mathrm{E}} + (9 \pm 2)\,\%$ [87].

3.2 Track types

Depending on which subdetectors are used in the reconstruction, there are five track types at the LHCb experiment. They are visualised in Fig. 3.5. Out of these five track types, three are used in the analysis presented in this thesis. They are defined as follows:

Long track (L): A long track is reconstructed by the VELO and tracking stations after the magnet. This track type has the most accurate information and, therefore, the smallest uncertainty. Due to the reconstruction in the VELO the mother particle has to have a sufficiently short lifetime.

Downstream track (D): A downstream track is measured in the TT and the tracking stations after the magnet. There is no information from the VELO because either the mother particle has a long lifetime or the pseudorapidity is higher than the VELO acceptance.

Upstream track (U): Upstream tracks are only reconstructed in the VELO and the TT. These tracks are most likely bent out of the acceptance by the magnet due to their low momentum. The momentum resolution is noticeably worse compared to long and downstream tracks.

The other two possible reconstruction types are velo tracks (V) and t tracks (T), where only the VELO or the tracking stations are used for the reconstruction. However, these types are not used in the analysis presented in this thesis.

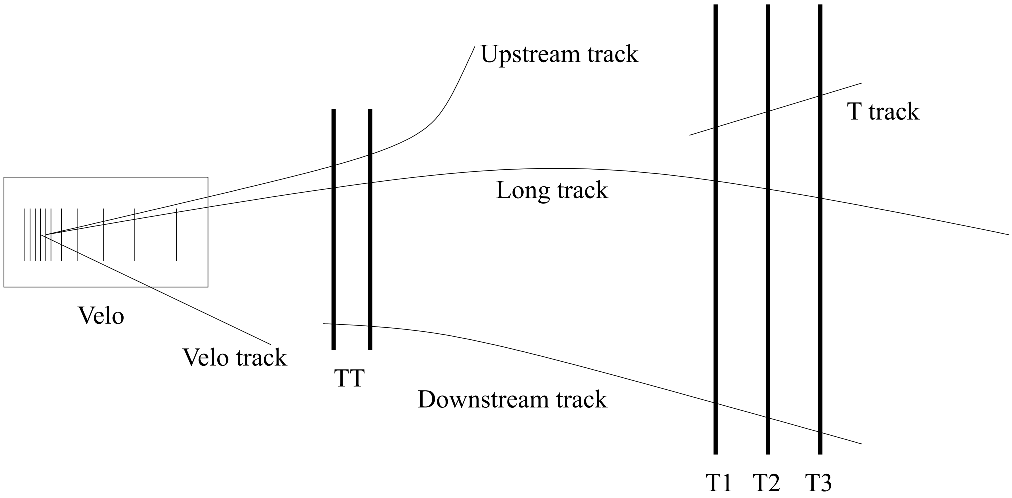

Figure 3.5: Sketch of the LHCb subdetectors mainly used for the tracking with the different track types reconstructed at the LHCb experiment taken from Ref. [88]

3.3 Trigger system

The trigger system in the LHCb experiment is used to reduce the incoming data for events with signal-like attributes. The scheme of the used steps can be seen in Fig. 3.6. The *pp* collisions occur at a rate of 40 MHz and the data-taking rate is reduced to 1 MHz after the hardware trigger L0. The next step is the software trigger corresponding to the HLT1 and HLT2, where the data is reduced to 12.5 kHz and saved to storage. The trigger decision to save or discard the event is based on the properties of the tracks. The L0 trigger does not reconstruct the whole event with track combinations or the track quality due to the limited time. Therefore, only basic requirements from information from the calorimeters and the muon stations are applied. For example, the muon L0 trigger in 2016 is only saving the

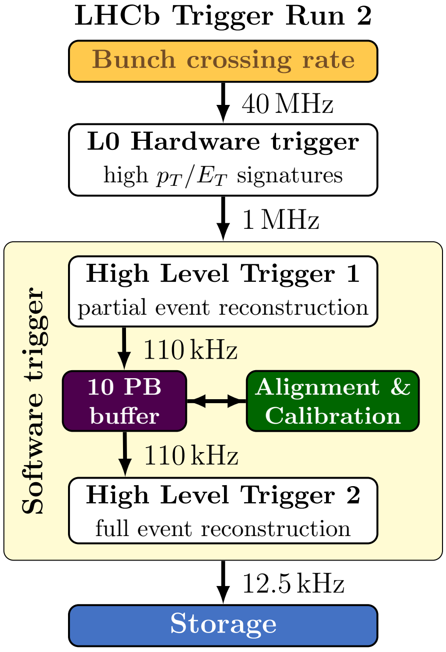

Figure 3.6: Overview of the LHCb trigger system. Reproduced from Ref. [89].

event if one muon in the event fulfils the requirement $p_{\mathrm{T}} > 1.8\,\mathrm{GeV/c}$. In the HLT trigger stages the event is reconstructed and more complex requirements are imposed like particle identification variables, the decay topology or the output from machine learning algorithms. In the end, each trigger decision is split into three different categories, whether the triggered particle is associated to the signal decay (TOS), a decay independent of the signal (TIS) or the full event (DEC).

3.4 LHCb simulation

A crucial part of analyses are simulations of signal and background attributes. At the LHCb experiment Monte Carlo simulations are used, describing every aspect of recorded data. At first, the pp collisions are simulated with PYTHIA [90, 91] using the attributes described in [92]. This includes simple two-body decays up to multi-scattering. The decays of hadronic particles are simulated in EVTGEN [93], including descriptions of angular and time-dependent correlations as well as *CP* violation and the mixing of neutral mesons. In this step the underlying event is also generated, which is important for the flavour tagging, the identification of the initial flavour of the B^0 meson, which is explained in more detail in Ch. 8. Photon radiation of the final state particles is included with PHOTOS [94, 95]. The interaction of the detector with all particles is simulated with GEANT4 [96, 97] and for the digitisation in the detector BOOLE [98] is used. After that, the same steps as in the data are performed. The trigger decisions are applied in MOORE [98], the reconstruction of the particles and their tracks in BRUNEL [99] and the stripping is made with DaVinci [100].

The stripping is the final step in data processing, where various selection requirements are imposed throughout the data and the raw data is transformed into a more human-readable form. In addition, it is possible to recalculate properties like the flavour tagging variables if updated algorithms are available and perform a more precise reconstruction with the DecayTreeFitter (DTF) [101]. This is not always used because it is more computationally expensive and, therefore, impossible for every data. It is more accurate because second-order effects of correlations and uncertainties are considered. The second benefit of this tool is that the decay can be reconstructed while fixing some parameters, like the reconstructed mass of the J/ψ to its known mass or the origin vertex of the B^0 meson to the PV. This way, physics knowledge can increase the precision of reconstructed properties like the mass or decay time even more.

4 Overview of the analysis

The aim of the presented analysis is the measurement of the *CP* violation parameters S and C in three $B^0 \to \psi K^0_S$ decays, where the K^0_S meson decays into two oppositely charged pions and the ψ meson represents $J/\psi \to \mu\mu$, $J/\psi \to ee$ and $\psi(2S) \to \mu\mu$ decays. The data is collected by the LHCb experiment between 2015 and 2018, referred to as Run 2, corresponding to an integrated luminosity of $6\,\text{fb}^{-1}$. The pions can be categorised into different reconstruction types; see Sec. 3.2. The selected data contains either two downstream pions (DD) or two long tracks (LL) for all three decays. In addition, the $J/\psi \to \mu\mu$ data include K^0_S mesons reconstructed by a downstream and long track (LD) and an upstream and long track (UL). The data sample with $J/\psi \to \mu\mu$ decays gains additional 13% of data with these two reconstruction types. Moreover, they are used for the first time in analyses by the LHCb experiment. The same are not included in both other decays because these data samples are smaller and the effort to analyse these data samples is not worth the gain in the overall sensitivity.

The analysis is structured into different parts. At first, the stored candidates are selected to remove as many background candidates as possible while keeping most signal candidates; see Ch. 5. The next step is to describe the B^0 meson mass distribution, where sWeights are computed. These weights help to unfold only the signal candidates out of the data. This is shown in Ch. 6. Afterwards, the decay time of the B^0 mesons is studied in Ch. 7 because the *CP* violation parameters are extracted from a fit describing the decay time. The essential identification of the initial flavour of the B^0 mesons is followed and explained in Ch. 8. The used model with all external parameters to extract the *CP* violation parameters is shown in Ch. 9. Every analysis has systematic uncertainties due to the methodology and the uncertainties from external parameters. The amount of these systematic uncertainties is described in Ch. 10. In the same chapter the mandatory checks to validate the result are listed, too. The final results and a combination with previous measurements are listed in Ch. 11. In addition, a comparison with other experiments is performed and a preliminary new world average is estimated.

5 Preparation of the data

The branching fractions of the signal decays $B^0 \to J/\psi(\to \mu\mu)K^0_\mathrm{S}(\to \pi^+\pi^-)$ and $B^0 \to J/\psi(\to ee)K^0_\mathrm{S}(\to \pi^+\pi^-)$ are 1.84×10^{-5} for both J/ψ decays and around 1.61×10^{-6} for the $B^0 \to \psi(2S)(\to \mu\mu)K^0_\mathrm{S}(\to \pi^+\pi^-)$ decay. Thus, there are many *pp* collisions without any signal decay. Furthermore, the amount of recorded data from the *pp* collisions is so huge that it is impossible to store all of it. An efficient and time-saving selection is mandatory to reduce the amount of background contributions but keep as many signal candidates as possible. There are four main groups of possible backgrounds:

- Misidentified background,
- Partially reconstructed background,
- Combinatorial background,
- A combination of the backgrounds above.

Misidentified backgrounds are decays where at least one particle is wrongly identified, *e.g.* the decay $B^0 \to \psi K^*(\to K^\pm\pi^\mp)$ with a misidentification of the $K^\pm$ meson as a $\pi^\pm$ meson. Hence, the K^* meson would be reconstructed as a K^0_S meson, which results in the signal decay $B^0 \to \psi K^0_\mathrm{S}(\to \pi^+\pi^-)$. These backgrounds are suppressed, for example, due to the accurate particle identification in LHCb. Partially reconstructed backgrounds are decays where one or more particles are not reconstructed, *e.g.* $B^0 \to J/\psi K^0\pi^+\pi^-$. In this case, the neutral kaon is not reconstructed, which would mimic the signal decay $B^0 \to \psi K^0_\mathrm{S}(\to \pi^+\pi^-)$. The advantage is that the mass of such reconstructed B^0 mesons is decreased by the mass of the K^0 meson because the reconstructed invariant mass of the B^0 meson would miss the mass of the K^0 meson. That is why these backgrounds are not always reconstructed in the same mass range as the signal decay, and it is possible to remove them by a requirement on the B^0 meson mass. Combinatorial background is the most common type of background candidates. In *pp* collisions many particles are created, especially pions. Two pions may be associated with the signal decay but originate directly from the *pp* collision or another decay. Although this decay could be similar to the signal decay, it must be removed. The last group is the combination of the previous backgrounds, which can be dealt with in the same way as explained above.

In the following sections, the selection criteria and methods used are explained, beginning with one-dimensional requirements of decay particle properties in Sec. 5.1

and a multivariate selection in Sec. 5.2. It is followed by a multiple-candidate selection in Sec. 5.3 and specific vetoes in Sec. 5.4. Finally, the efficiencies of all selection steps are given in Sec. 5.5.

5.1 Basic selection requirements

At first, fundamental requirements, so-called stripping requirements, are imposed to reduce the amount of data. The requirements are based on the reconstructed-mass of the combined particles, the decay time of the B^0 and K^0_S meson, the vertex and track quality, the particle identification of the electrons, the momentum of the final state particles and the separation of the pions from the PV. These requirements help to distinguish between signal and background candidates because, *e.g.*, the background tracks are distant from each other as they originate from different vertices. On the left side of Fig. 5.1 the data for the electron channel can be seen after the selection. The number of combinatorial background candidates is still so high that no signal component is visible. Therefore, additional requirements are imposed and the current ones are tightened to reduce the background even more. With this selection, it is possible to see the signal component in the mass distribution on the right side of Fig. 5.1. For both muon channels additional requirements are not needed due to the more efficient selection of the muons.

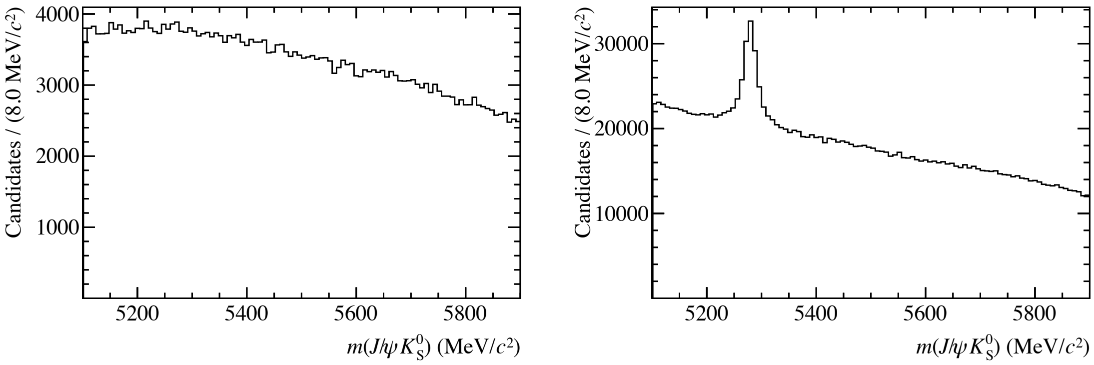

Figure 5.1: Mass distribution of $B^0 \to J/\psi(\to ee)K^0_S$ candidates, where the J/ψ and K^0_S are set to their known mass from [40] (left) before and (right) after the first basic selection requirements. On the left side only a fraction of the whole data is shown but the distribution looks the same.

The next selection criteria applied are the trigger lines. As explained in Sec. 3.3 there are three trigger stages with several trigger lines per stage. One trigger line is a batch of requirements imposed on track properties, particle identification variables, the topology of the event or multivariate learners. All used trigger lines are shown in Table 5.1. The lines for both muon channels are mainly based on the properties of the muons, while a variety of lines are selected for the electron channel. This is

Table 5.1: Trigger lines for the analysed modes. One line must be triggered on signal (TOS) in each trigger stage for the muon channels. For $B^0 \to J/\psi(\to ee)K^0_S$ the lines take the full event (DEC) into account. The numbers in the parentheses indicate the years, where the lines are used if they are not used in all years.

stage	$B^0 \to J/\psi K^0_S$	$B^0 \to \psi(2S)K^0_S$	$B^0 \to J/\psi(\to ee)K^0_S$
L0	Muon DiMuon L0MuonHigh	Muon DiMuon L0MuonHigh	Electron Hadron Muon DiMuon Photon JetEl MuonNoSPD(15) MuonEW(16-18)
HLT1	DiMuonHighMass TrackMuon	DiMuonHighMass TrackMuon	TrackMVA TwoTrackMVA
HLT2	DiMuonJPsi DiMuonDetachedJPsi	DiMuonPsi2S DiMuonDetachedHeavy	Topo[2,3]Body RadiativeIncHHGamma(15) Topo[E,EE]2Body(16-18)

due to the more challenging selection of electrons. The choice of the trigger lines in the electron channel is made in a recursive procedure to maximise the number of signal decays:

1. Apply the full selection to data without any particular trigger requirement
2. Apply each possible line, fit the $m(J/\psi K^0_S)$ data with the nominal Probability Density Function (PDF) described in Ch. 6 and count the signal decays
3. Choose the line with the highest yield and add this line to the used trigger lines
4. Redo the previous steps until the added yield is below 0.5 % of the possible signal yield

This way, the amount of signal candidates is maximised while the background contributions are removed.

Afterwards, further loose requirements are applied. This includes a global reconstruction quality, a tightened reconstructed-mass range, a selection of used PVs with the smallest distance to the B^0 meson flight trajectory, which reduces the number of wrongly associated PVs, and the requirement that the DTF reconstruction fit with fixed masses and fixed PV converges. Furthermore, the simulation sample is required to contain signal decays or at least signal-like reconstructed candidates, where one particle is not associated with the true signal decay but the reconstructed

B^0 meson mass is close to the true mass. This is enforced by the true information of the simulation.

After the entire selection and before the *CP* fit, additional requirements are applied. The decay time of the B^0 meson has to be in the range from 0.2 to 15 ps, and only tagged candidates are selected; that are candidates where at least one tagging algorithm, explained in Ch. 8, gives a decision whether the parent particle is a B^0 or $\overline{B}^0$ meson.

5.2 Multivariate selection

Multivariate classifiers are perfect tools to distinguish signal from background components. Due to their non-linearity and multidimensionality, they are highly efficient and commonly used in high-energy physics analyses. One example of a multivariate classifier is a boosted decision tree (BDT), which is a build-up of simple decision trees. Decision trees divide the data into two samples, which are divided again into two samples as long as desired. The partitioning is fulfilled by requirements on the data properties. In the end, each sample is classified either by absolute terms, *e.g.* classified as signal or background, or by a number, representing how likely the sample corresponds to the signal or background. A sketch of a decision tree can be seen in Fig. 5.2. The rectangles show the requirements for each event. Whether the requirement is fulfilled, the event is selected into the left or right part. In the end, each event got assigned the weight in the leaves, denoted by the rhombuses. In this example, the requirements are imposed on the transverse momentum of the K^0_S meson and the pseudorapidity of the B^0 meson.

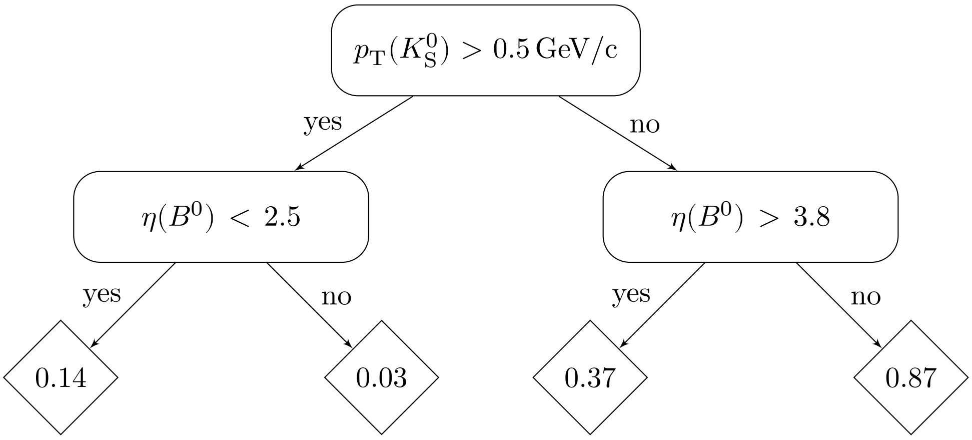

Figure 5.2: Sketch of a decision tree where the data are divided two times, first by the transverse momentum of the K^0_S meson and second by the pseudorapidity of the B^0 meson.

Decision trees are supervised learners, meaning the training data are labelled as whether they belong to signal or background candidates. With these labels, it is possible to evaluate the error metric, the number of right and wrong assigned candidates, and to compute the weights in the leaves, which are correlated to the error metric.

In the following, the principle and the parameters of the used BDT are explained, followed by the choice of the training variables and the evaluation of the most efficient requirement on the output of the trained BDT.

Boosted decision trees

Boosted decision trees are groups of simple decision trees where one decision tree is added in each iteration. The total weight of an event is the normalised sum of weights from each decision tree. Thereby, a BDT has the advantage of using multiple variables and their correlation to distinguish signal from background without needing as many splitting steps as input variables.

To remove the huge amount of mainly combinatorial background the XGBoost algorithm [102] is used. Because the XGBoost algorithm is a supervised learner, simulated signal decays are chosen as signal proxy, while the background proxy is recorded data, where the reconstructed invariant $\mathrm{m}(\psi K_{\mathrm{S}}^{0})$ mass is in the range from 5450 to 5900 MeV/c^2. The signal and background samples are reduced to have the same number of signal and background events. This is done to avoid a classification more likely towards the proxy with more input data. To fully exploit the training data, the kFolding method [103] with $k = 5$ is used. This means that the whole data set is split into five equally sized parts, where four are used in the training of the BDT and one is used for the evaluation. It is repeated five times, such that each part is once used for the evaluation. This method has the advantage that more data can be used in the training of the BDT, which is essential for its performance. The BDT prediction is the average of the five classifiers. However, it is ensured that only those BDTs are used where the event was not part of the training sample. In addition, the kFolding method helps to avoid overtraining, where the BDT classifies on specific attributes in the training sample, which cannot be generalised to other data sets. This is ensured since the final BDT prediction is averaged over five single predictions. Early stopping is implemented, which means that the training of new trees is stopped once the performance of the evaluation did not improve in the last 50 iterations. The BDT uses the best iteration afterwards. The tree depth is limited to four, the learning rate, which reduces the impact of the next iteration, is set to 0.04 and the evaluation metric is the fraction of wrong-classified events. The evaluation metric and the BDT response for one of the five BDTs are shown in Fig. 5.3 for the track type DD of $B^0 \to J/\psi(\to ee)K_{\mathrm{S}}^{0}$ candidates. In the BDT output, it can be seen that the distributions of the training and test samples match well, and a good separation is possible. The error rate shrinks rapidly in the first 200 iterations and flattens afterwards. The error rates of the training and test samples diverge at some point, which is, however, not alarming because the performance on the test sample is not decreasing. The other final states and track types look similar, except that the number of used iterations increases with the

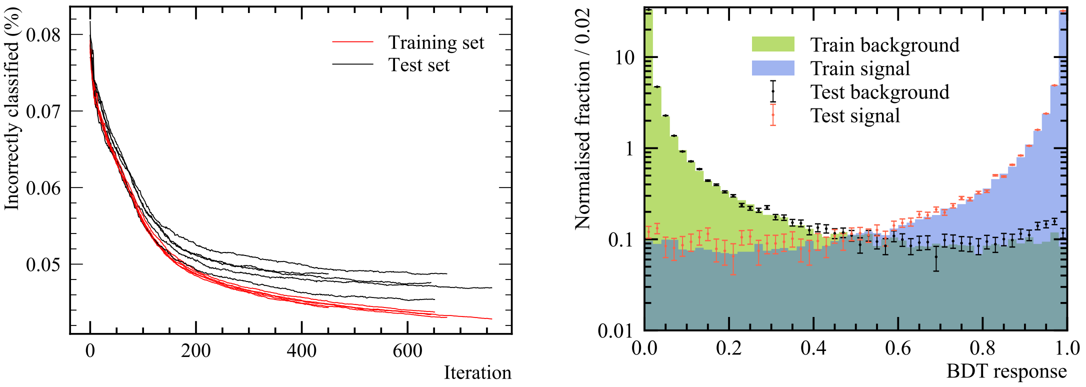

Figure 5.3: Error rate evolutions and BDT outputs for the complete $B^0 \to J/\psi(\to ee)K^0_S$ Run 2data set for DD. The BDT output is shown for one of the five BDTs of the k-folding. The distributions for the remaining BDTs and for LL look similar. The abbreviations FP and FN are false positive and false negative, respectively.

input data size.

Training variables

One important part of utilising multivariate learners is the choice of the input variables or features. They have to fulfil the following specifications:

- The features have to be well-modelled in simulation so the classifier does not train on differences between data and simulated data.
- The distributions of signal and background have to be significantly different to have a possibility to distinguish signal and background candidates, called separation power.
- The correlation among the features should not be too high, over 95 %, because these features do not contribute with additional information and only increase the computing time.
- The features must not be correlated to the invariant B^0 mass to not classify on the different mass of the signal and background proxy.
- The features must not be correlated to the B^0 decay time to avoid falsifying the proper shape. Complete independence, however, cannot be achieved and is later modelled by an empirical acceptance function, which is explained in more detail in Sec. 7.1.

For the first specification, the signal component has to be extracted from the data. Thus, the sPlot method [104, 105] is used, where weights are computed, which project the signal component out of the data. Therefore, it is necessary to model the distribution of the signal and background component in one variable. The easiest way is the description of the invariant mass $\mathrm{m}(\psi K^0_\mathrm{S})$. The data consists of background candidates described by an exponential function and signal candidates modelled by the sum of two Gaussian functions, which share the mean. One example where the signal and background distributions are similar is the vertex χ^2 of the K^0_S and can be seen at the top in Fig. 5.4. A poorly described variable in the simulation, the track χ^2 of the e^-, can be seen at the bottom left and at the bottom right the transverse momentum of the e^- is shown, which is well described and has a high separation power.

In the end, the training variables consist of impact parameters, the shortest distances from the particle trajectory to the PV, transverse momenta, momenta in z-direction, vertex qualities, pseudorapidities, flight distances, decay times and the shortest distances of two particle trajectories. The distributions of these variables are different for each final state and track type. Therefore, individual BDTs are trained, and the chosen variables differ for each track type and between the muon and electron channels. In the end, between 18 and 24 variables are selected.

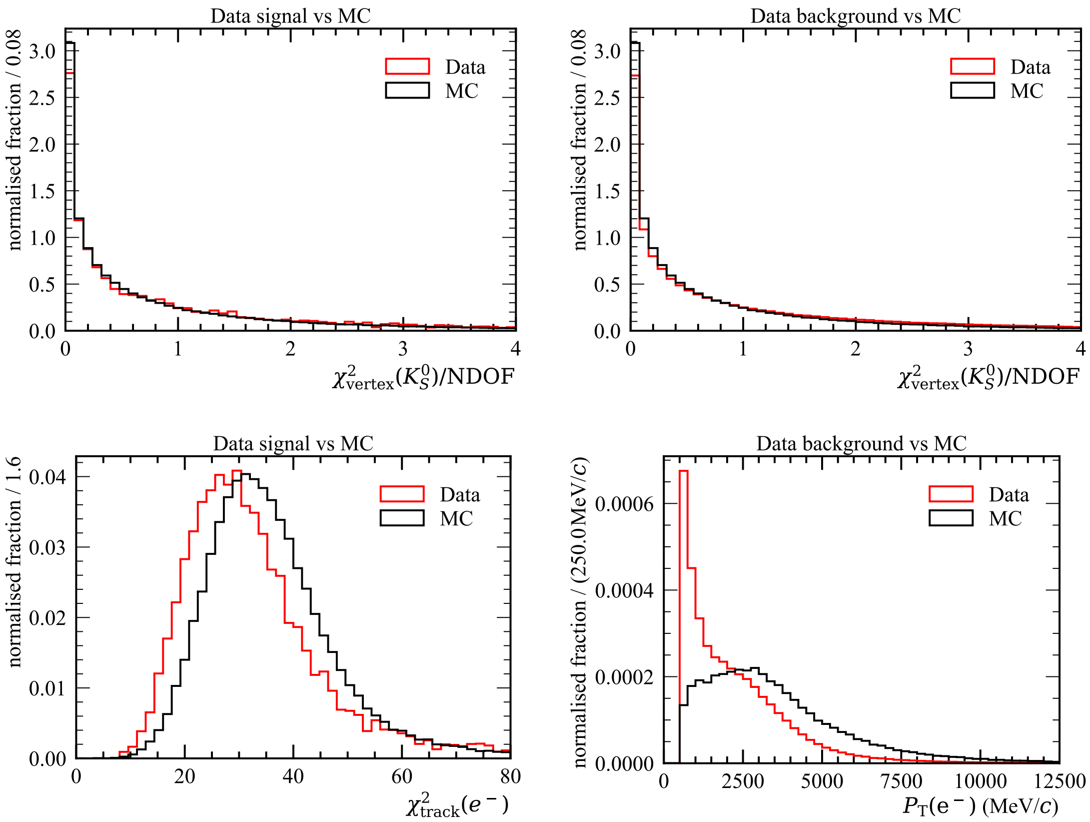

Figure 5.4: Recorded and simulated data distributions before the BDT selection of DD reconstructed $B^0 \to J/\psi(\to ee)K^0_S$ decays of (upper-left and upper-right) the vertex χ^2 per degree of freedom of the K^0_S without differences in signal and background data, (lower-left) the poorly described track fit χ^2 of the e^- in simulated data, and (lower-right) the transverse momentum of the e^-, which is well described and has a high separation power between signal and background data.

Requirement on the BDT output

After the training of the BDT, the selection is based on the BDT output. The best value is evaluated with the figure of merit (FoM):

$$\text{FoM}(c) = \frac{S(c)}{\sigma\left(S(c)\right)}, \tag{5.1}$$

where $S(c)$ and $\sigma\left(S(c)\right)$ are the number of signal decays and its uncertainty, respectively, where the BDT output is greater than c. The FoM is chosen to maximise the signal sensitivity. The number of signal decays is determined in a fit to the data with an integral over the signal PDF in the smallest reconstructed-mass range of 95 % of simulated signal candidates. The reconstructed-mass model is explained in detail in Ch. 6 because the simpler model described above can no longer describe the data after a requirement on the BDT output. The values of the

FoM are shown in Fig. 5.5 with single dots. It can be seen that these FoM fluctuate due to the not perfectly stable fit. It was tested that it is possible to solve these instabilities with a better choice of starting parameters for each fit. However, this is time-consuming and does not improve the selection. Instead, a cubic spline is used to smooth the result and determine the maximum from this line. Moreover, the maximum of the FoM is on a plateau with several fits, which means that the exact requirement on the BDT does not change the selection significantly.

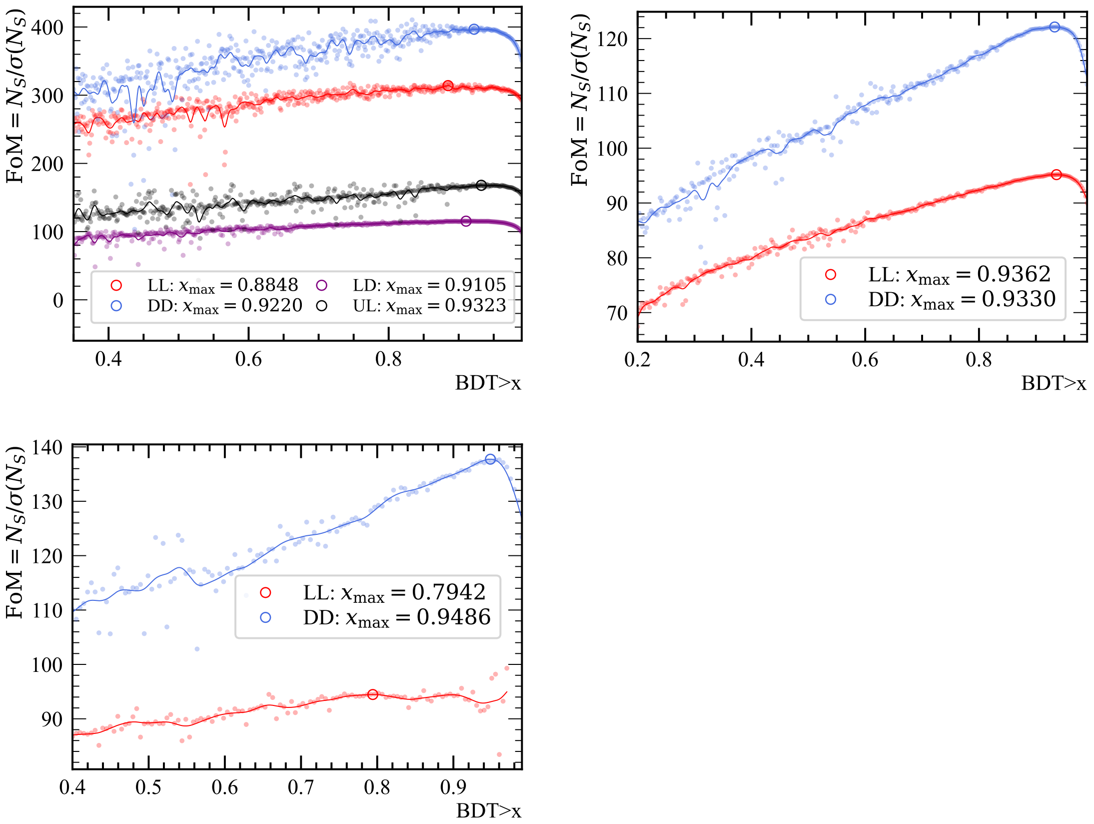

Figure 5.5: Figures of merit for the modes (upper-left) $B^0 \to J/\psi(\to \mu\mu)K^0_S$, (upper-right) $B^0 \to \psi(2S)K^0_S$ and (lower-left) $B^0 \to J/\psi(\to ee)K^0_S$ as a function of the BDT requirement with 500, 300 and 120 single fits marked with diminished dots to the invariant mass of the B^0 meson, respectively. Due to statistical fluctuations, the best parameters in these fit varies and, thus, the FoM. The solid line is a cubic spline for each single data point to comprehend this.

5.3 Multiple-candidate removal

In some events, it is possible to reconstruct multiple signal candidates. This happens if two or more final state particles pass the selection and form a signal candidate, *e.g.* one J/ψ candidate can be combined with two different K^0_S candidates. It is extremely rare that multiple signal decays occur in the same event and, therefore, only the candidate with the highest transverse momentum of the B^0 meson is chosen. This has the advantage that the data is unbiased and has a higher effective tagging efficiency to identify the initial flavour of the B^0 meson. The fraction of these candidates after the selection is below 1 %, which can be seen in Table 5.2 for each final state for all years combined.

Table 5.2: Amount of multiple candidates after the BDT selection and the fraction of multiple candidates for all years combined for each final state. The uncertainty of the fraction originates from the statistics of the data.

Multiplicity	$B^0 \to J/\psi(\to \mu\mu)K^0_S$	$B^0 \to \psi(2S)K^0_S$	$B^0 \to J/\psi(\to ee)K^0_S$
2	3479	354	632
3	39	1	3
4	2	0	1
5+	1	0	0
Total	3567	356	641
Fraction [%]	0.719 ± 0.012	0.657 ± 0.035	0.533 ± 0.021

5.4 Background vetoes

Some misidentified or partially reconstructed decays still remain after the previous selection requirements. Therefore, specific vetoes are applied to keep most of the signal and remove these backgrounds. The decay $B^0 \to \psi K^*(892)^0(\to K^\pm\pi^\mp)$ mimics the signal decay if the kaon is misidentified as a pion. The straightforward requirement on the particle identification of the pions is insufficient, but the K^{*0} meson is short-lived in contrast to the K^0_S meson. Thus, a lifetime requirement of $t_K > 0.5\,\text{ps}$ is very efficient. In Fig. 5.6 the $B^0 \to J/\psi(\to \mu\mu)K^0_S$ LL data without this veto and the removed data can be seen. The removed data at $5180\,\text{MeV/c}^2$ is true misidentified background. In contrast, the data directly at the mass of the signal are either true signal candidates or prompt background candidates, which are not removed beforehand. The efficiency is evaluated on simulated signal data and estimated to be around 98 %, so no further improvements were made. The rejection is calculated on simulated $B^0 \to J/\psi(\to \mu^+\mu^-)K^*(892)^0(\to K^\pm\pi^\mp)$ decays with the same selection as for the signal and is found to be about 99.7 %.

Another misidentified background is $\Lambda^0_b \to \psi\Lambda(\to p\pi^-)$ with the misidentification of the proton as a pion. The background is clearly visible in the K^0_S mass spectrum if the signal data kinematics is refitted under the assumption that the positively charged pion has the proton mass; see the left side of Fig. 5.7. The veto is arranged such that misidentified pion candidates in the mass range

$1100 < m(p\pi) < 1130\,\mathrm{MeV}/c^2$ have to have a low probability of being protons. The vetoed data can be seen on the right side of Fig. 5.7. The efficiency on simulated signal data is over 98.5 %, while it is on $\Lambda_b^0 \to J/\psi(\to \mu\mu)\Lambda(\to p\pi^-)$ simulation with the same previous selection only around 2.6 %. The remaining candidates are below the statistical fluctuations of the combinatorial background and can, therefore, be described within the model of these candidates.

The decay $B^\pm \to J/\psi K^\pm$ can be reconstructed as the signal if the kaon is misidentified as a pion, and a random pion in the event is also associated with the decay. This background can be removed with a signal efficiency of over 99 % by a requirement on the particle identification of the pions to be unlikely a kaon. The UL data, which are mainly affected by this background, of $B^0 \to J/\psi(\to \mu\mu)K_S^0$ for all years before this veto can be seen in Fig. 5.8 as well as the inversely vetoed data to illustrate the effect of this requirement.

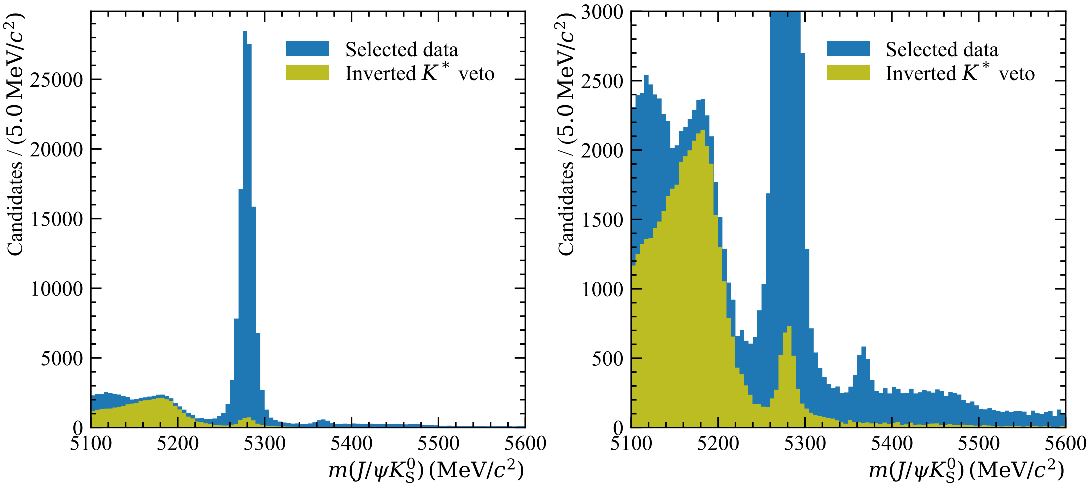

Figure 5.6: Invariant B^0 meson mass of LL reconstructed K_S^0 mesons in $B^0 \to J/\psi(\to \mu\mu)K_S^0$ decays for all years combined after the $K^*(892)^0$ veto and the vetoed data. The right plot is a zoomed-in version of the left plot.

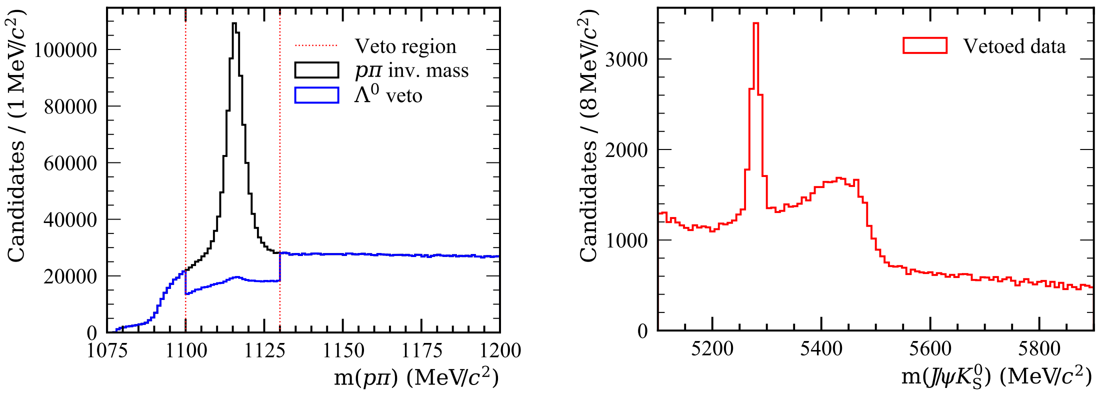

Figure 5.7: Invariant mass spectrum of the K^0_S meson, where the mass hypothesis for one pion is set to the proton for $B^0 \to J/\psi(\to \mu\mu)K^0_S$ decays for all years combined. In this way, true lambda decays are visualised. The mass is shown on the left before and after the veto and on the right the vetoed data in the nominal invariant mass of the B^0 meson.

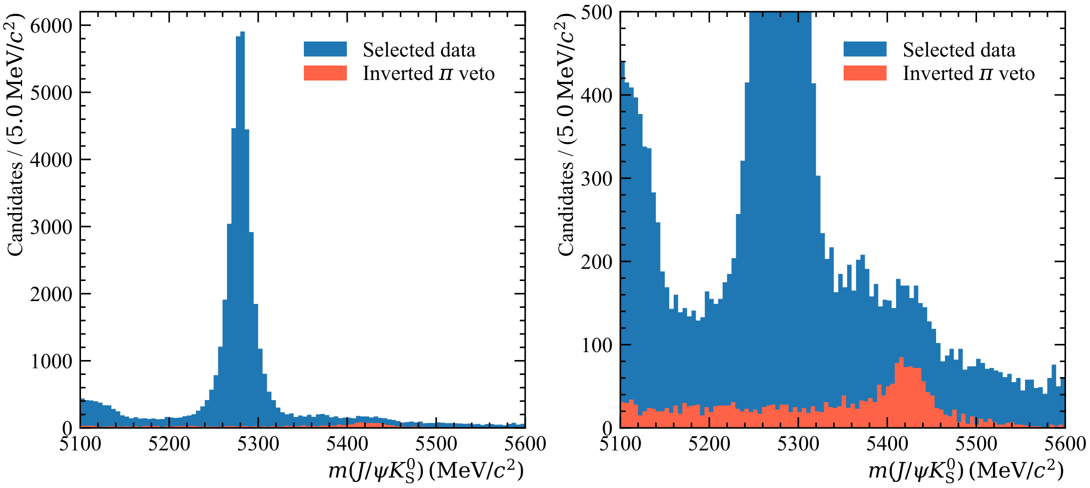

Figure 5.8: Invariant B^0 meson mass of UL reconstructed K^0_S mesons in $B^0 \to J/\psi(\to \mu\mu)K^0_S$ decays for all years combined after the veto against $B^+ \to J/\psi K^+$ decays. The right plot is a zoomed-in version of the left plot.

5.5 Selection efficiencies

To evaluate the performance of the selection, it is necessary to calculate the signal efficiency. This is done on simulated signal data, where the numbers of candidates are counted before and after the requirements. The efficiencies of each selection step for $B^0 \to J/\psi(\to \mu\mu)K^0_S$ decays are given in Table 5.3, where the geometry efficiency is due to the geometric acceptance of the detector and evaluated on simulation and the detector model. The lowest efficiency is given by the stripping

Table 5.3: Selection and reconstruction efficiencies for $B^0 \to J/\psi(\to \mu\mu)K^0_S$ candidates determined on simulation with the uncertainties calculated as described in Ref. [106].

Selection	Efficiency [%]			
	LL	DD	LD	UL
Geometry	19.897 ± 0.083			
Stripping + reco.	2.2615 ± 0.0030	5.187 ± 0.004	0.3499 ± 0.0012	0.7513 ± 0.0017
Kinematic and topology	96.393 ± 0.025	97.952 ± 0.013	95.20 ± 0.07	97.36 ± 0.04
Trigger	75.39 ± 0.06	74.63 ± 0.04	76.64 ± 0.15	76.88 ± 0.10
Λ^0_b veto	99.051 ± 0.015	98.209 ± 0.014	99.254 ± 0.034	98.585 ± 0.032
BDT	87.96 ± 0.05	79.37 ± 0.04	79.96 ± 0.16	79.52 ± 0.11
K^{*0} veto	97.961 ± 0.024	100.0 ± 0.0001	99.972 ± 0.008	99.205 ± 0.027
π veto	99.536 ± 0.012	100.0 ± 0.0001	99.709 ± 0.024	99.818 ± 0.013
Decay time	98.814 ± 0.018	98.507 ± 0.014	99.25 ± 0.04	99.605 ± 0.019
Mult. cand.	99.678 ± 0.010	99.689 ± 0.007	99.25 ± 0.04	98.839 ± 0.033
Only tagged cand.	84.20 ± 0.06	87.04 ± 0.04	84.56 ± 0.16	82.20 ± 0.12
Total	0.2304 ± 0.0011	0.5026 ± 0.0022	0.03347 ± 0.00022	0.0703 ± 0.0004

selection and reconstruction, which is expected due to the challenging reconstruction and the huge amount of background candidates which have to be removed by the stripping. The efficiencies for $B^0 \to \psi(2S)K^0_S$ decays are similar with slightly higher trigger efficiencies. This originates from the higher momentum of the muons due to the higher mass of the $\psi(2S)$ meson compared to the J/ψ meson. For $B^0 \to J/\psi(\to ee)K^0_S$ decays the efficiencies are listed in Table 5.4. The kinematic and topology efficiency difference in LL and DD is mainly due to a flight distance

Table 5.4: Selection and reconstruction efficiencies for $B^0 \to J/\psi(\to ee)K^0_S$ candidates determined on simulation with the uncertainties calculated as described in Ref. [106]. The difference in the kinematic and topology efficiency is mainly caused by the flight distance requirements on the LL and DD kaons.

Selection	Efficiency [%]	
	LL	DD
Geometry	19.75 ± 0.05	
Stripping + reco.	1.4619 ± 0.0033	4.015 ± 0.005
Kinematic and topology	54.57 ± 0.11	62.35 ± 0.07
Trigger	46.68 ± 0.15	41.42 ± 0.08
Λ^0_b veto	99.384 ± 0.035	98.321 ± 0.034
BDT	94.55 ± 0.10	76.91 ± 0.11
K^{*0} veto	99.887 ± 0.015	100.0 ± 0.0008
π veto	99.517 ± 0.032	100.0 ± 0.0008
Decay time	100.0 ± 0.0018	99.9944 ± 0.0024
Mult. cand.	99.937 ± 0.012	99.763 ± 0.015
Only tagged cand.	89.23 ± 0.14	90.37 ± 0.09
Total	0.06126 ± 0.00034	0.1396 ± 0.0006

requirement on the K_S^0 meson. Furthermore, the total efficiency is lower than in both muon channels due to the more difficult selection and reconstruction of electrons.

6 Parametrisation of the invariant mass

No efficient selection is possible where all background candidates are entirely removed. Hence, background candidates are still present after the full selection, described in Ch. 5, which should not be considered in the final measurement. As mentioned in Sec. 5.2, the extraction of sWeights solves this problem because the sWeights can unfold the signal and background distributions statistically. The invariant mass of the B^0 meson is an excellent variable to model both signal and background components. The kinematic and the invariant mass distributions differ between the track types. That is why the sWeights are determined separately for each track type. In this chapter, only the $B^0 \to J/\psi(\to ee)K^0_\mathrm{S}$ candidates are discussed in detail, while the results for both muon channels are compared with these results. At first, the signal and background models and the determination of the mass shapes are explained and in the end, the number of signal candidates is given for each track type.

Model of the signal component

In contrast to the data before the BDT selection, the signal B^0 meson after the entire selection can no longer be described by two Gaussian functions. Therefore, the more complex double-sided Hypatia function [107] is used. In a simplified version, it is defined as:

$$H(m-\mu,\sigma,\alpha_1,n_1,\alpha_2,n_2,\lambda) \propto \begin{cases} A(B-(m-\mu))^{-n_1} & m-\mu < -\alpha_1\sigma \\ A'(B'+(m-\mu))^{-n_2} & m-\mu > \alpha_2\sigma \\ \left(1-\frac{(m-\mu)^2}{2\sigma^2(1+\lambda)}\right)^{\lambda-\frac{1}{2}} & \text{otherwise} \end{cases} \tag{6.1}$$

The parameters A, B, A' and B' are not constants but depend on the other parameters and ensure the differentiability and continuity of the Hypatia distribution. The tail parameters α_1, n_1, α_2 and n_2 determine the function's slope towards higher and lower masses. They are evaluated in a fit of simulated data and fixed later in the fit to the recorded data. The fit of $B^0 \to J/\psi(\to ee)K^0_\mathrm{S}$ simulated decays is performed in the range from 5000 to 5900 MeV/c^2 and can be seen in Fig. 6.1, while the other muonic final states look similar.

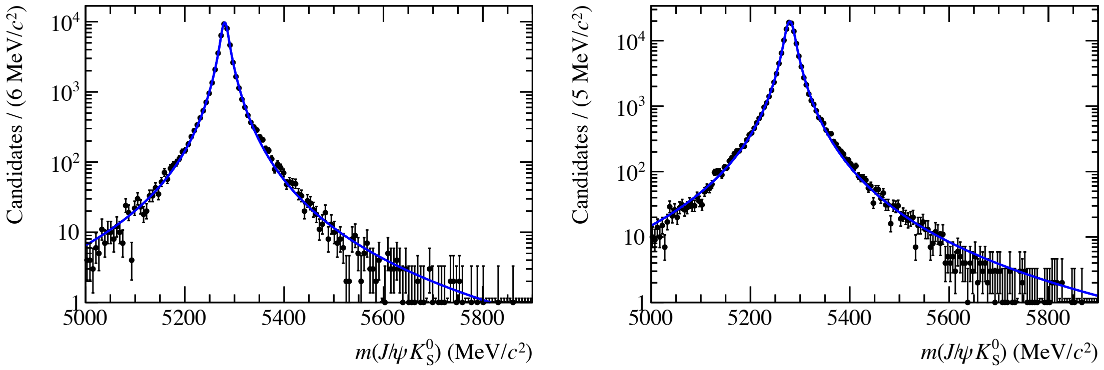

Figure 6.1: Invariant mass fit of simulated (left) LL and (right) DD $B^0 \to J/\psi(\to ee)K^0_S$ candidates where the signal (blue) is described by a Hypatia function.

Model of the background components

Since background candidates are still present in the data, the following three components have to be described in addition to the signal: The B^0_s component, the combinatorial background and a partially reconstructed background at low invariant masses. The B^0_s component is modelled in the same way as the B^0_d signal component. All parameters are shared except the mean, which is shifted by the $m(B^0_d) - m(B^0_s)$ mass difference [40]. The combinatorial background is described by an exponential function. The partially reconstructed background at lower masses is modelled by an exponential function, which turns into a Gaussian function for masses above a threshold T:

$$\mathcal{P}_{\text{part}}(m; \mu_{\text{part}}, \sigma_{\text{part}}, t_{\text{part}}) \propto \begin{cases} e^{\frac{1}{2}t^2_{\text{part}} - t_{\text{part}}\alpha} & m < T \\ e^{-\frac{1}{2}\alpha^2} & m \geq T \end{cases} \tag{6.2}$$

$$\alpha = \frac{m - \mu_{\text{part}}}{\sigma_{\text{part}}},\ t_{\text{part}} = \frac{T - \mu_{\text{part}}}{\sigma_{\text{part}}},$$

where μ_{part} and σ_{part} define the mean and width of the Gaussian component. The model is used because it is proven to be able to describe a potential partially reconstructed background from $B^{\pm/0} \to J/\psi(\to \mu\mu)K^{*\pm/0}(\to K^0(\to \pi^+\pi^-)\pi^{\pm/0})$ decays. This source of background occurs when the bachelor $\pi^{\pm/0}$ of the $K^{*\pm/0}$ is not reconstructed and, therefore, not considered in the calculation of the invariant mass of the B^0 meson. In this way, this background component has the same final state particles as the signal decay. The model has been validated by fitting a sample of partially reconstructed candidates generated using RapidSim [108] with a phase-space model. The result is shown in Fig. 6.2.

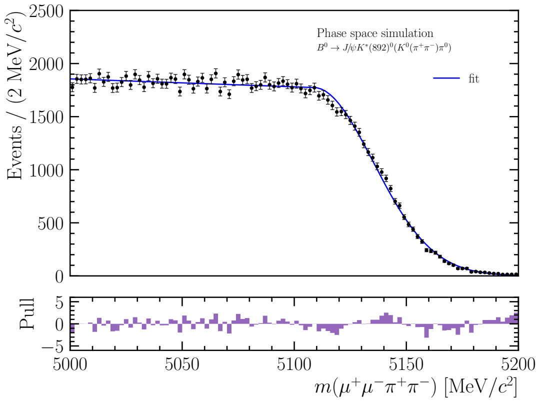

Figure 6.2: Invariant mass fit of simulated data generated using a phase-space model in RapidSim for the decay $B^0 \to J/\psi(\to \mu\mu)K^*(892)^0(\to K^0(\to \pi^+\pi^-)\pi^0)$, where one pion is not reconstructed. The fitted model is listed in Eq. (6.2).

Invariant mass fit on data

The invariant mass on data of the B^0 mesons is described by the sum of all four models explained above, namely the B^0 signal, the B_s^0 background, the combinatorial and the partially reconstructed background component. The fit is performed in the range from 5100 to 5900 MeV/c^2, while the sWeights are computed after projecting the PDF to the range from 5150 to 5900 MeV/c^2. By reducing the range, effects from the partially reconstructed background and the uncertainties on the sWeights are decreased. In Fig. 6.3 it can be seen that the model accurately describes the $B^0 \to J/\psi(\to ee)K_S^0$ candidates. The same is the case for both other muon final states. The difference in the mass resolution of reconstructed K_S^0 decays is slightly better for LL than for DD track types due to the information from the VELO. The effect is not significant because the decay vertex of the B^0 meson is mainly driven by the J/ψ meson and its both electrons, which are always created in the VELO. The mass resolution can be seen by comparing the resulting widths of the signal component of both track types. The comparison between the electron mode and both muon modes shows that the more difficult reconstruction and selection of electrons degrades the mass resolution and widens the width of the signal component. The mass resolution of the $B^0 \to \psi(2S)(\to \mu\mu)K_S^0$ decays is smaller than that of $B^0 \to J/\psi(\to \mu\mu)K_S^0$ decays due to the smaller phase-space of the $\psi(2S)$ and the higher momentum of the muons.

In summary, it is possible to describe the signal and all background components in the invariant mass of the B^0 mesons with the same model but separately for each final state and track type. This way, sWeights are computed to unfold the signal component in every other distribution, which is necessary for the fit to the decay time to determine the *CP* violation parameters.

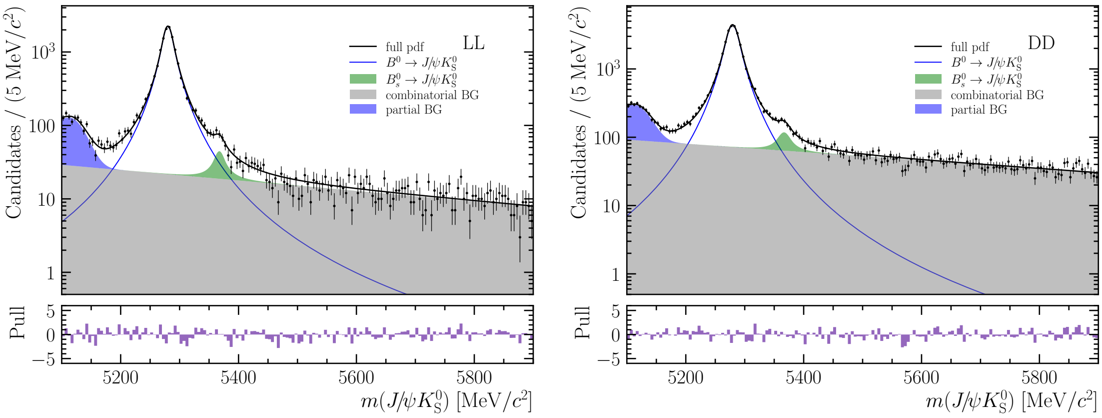

Figure 6.3: Invariant mass fit of selected data for (left) LL and (right) DD $B^0 \to J/\psi(\to ee)K^0_S$ candidates with (blue, solid) the signal component, (grey, filled) the combinatorial background, (purple, filled) the partially reconstructed low-mass background and (green, filled) the peaking $B^0_s \to J/\psi(\to ee)K^0_S$ background on the full range.

Number of signal candidates

The number of candidates for each component split into the two track types is shown in Table 6.1. It is visible that the LL reconstructed candidates have a better reconstruction because the ratio of signal over background candidates is significantly higher in LL with 5.1 compared to DD with 2.7. The numbers of all signal candidates for all final states are shown in Table 6.2, which sum up to 433520 total signal candidates after the whole selection. It can be seen that the highest sensitivity for the final result is achieved for $B^0 \to J/\psi(\to \mu\mu)K^0_S$ decays. Furthermore, the LD and UL reconstructed K^0_S mesons have a similar yield as all candidates from the $B^0 \to J/\psi(\to ee)K^0_S$ decays, which indicates the rewarding effort to include these candidates for the first time in an analysis from the LHCb experiment.

Compared to the previous analyses [32,33] measuring the *CP* violation parameters in the analysed decays, the number of signal candidates is more than tripled.

Table 6.1: Yields for the different components for LL and DD reconstructed candidates of $B^0 \to J/\psi(\to ee)K^0_S$ decays.

Track type	$N_{B^0 \to J/\psi(\to ee)K^0_S}$	$N_{B^0_s \to J/\psi(\to ee)K^0_S}$	N_{comb}	N_{partial}
LL	$13\,494 \pm 151$	163 ± 30	2428 ± 150	755 ± 58
DD	$29\,182 \pm 222$	363 ± 48	8551 ± 232	1588 ± 89

Table 6.2: Signal yields for $B^0 \to J/\psi(\to \mu\mu)K^0_{\mathrm{S}}$, $B^0 \to J/\psi(\to ee)K^0_{\mathrm{S}}$ and $B^0 \to \psi(2S)K^0_{\mathrm{S}}$ candidates for each track type.

Track type	$N_{B^0 \to J/\psi(\to \mu\mu)K^0_{\mathrm{S}}}$	$N_{B^0 \to J/\psi(\to ee)K^0_{\mathrm{S}}}$	$N_{B^0 \to \psi(2S)K^0_{\mathrm{S}}}$
LL	$88\,745 \pm 314$	$13\,494 \pm 151$	8158 ± 94
DD	$174\,447 \pm 480$	$29\,182 \pm 222$	$15\,230 \pm 134$
LD	$13\,906 \pm 134$		
UL	$27\,270 \pm 183$		

7 Decay time description

To extract the *CP* parameters from the ψK^0_S candidates, a fit to the decay time distribution of the B^0 meson is performed from 0.2 to 15 ps. In first order, the decay time can be described by an exponential function. However, there are complications which need to be taken into account. At first, the decay-time-dependent detector effects and background subtraction efficiencies change the pure exponential trend and play a substantial role at very short and high decay times. In addition, the finite decay time resolution of the detector smears the *CP* violation asymmetry and, therefore, directly decreases the value of $\sin(2\beta)$ if it is not described. Furthermore, the reconstruction of the decay time can introduce a bias, which needs to be considered as well.

In this chapter, the model of the decay time distribution is discussed in detail. In Sec. 7.1 the time-dependent selection and reconstruction efficiency, called acceptance, is described, while the decay time resolution due to the imperfect detector measurement is reported in Sec. 7.2. In the end, in Sec. 7.3 the decay time bias is evaluated on prompt data samples including a study to check if the decay time bias can be propagated from prompt data to signal data.

7.1 Decay time dependent efficiencies

Most background candidates are present at short decay times of the B^0 meson because most of the particles in an event are produced directly in the *pp* collision or from short-lived particles. Therefore, it is very effective to apply requirements that remove short-lived candidates. However, this also means the signal efficiency depends on the decay time. Furthermore, the reconstruction at short decay times is more difficult due to more difficult vertex separation, leading to a time-dependent efficiency.

To take this dependency into account an acceptance function is modelled using cubic spline functions [109,110]. The input variables for the cubic spline functions are the knot positions in the decay time and the coefficients corresponding to each knot. The number of knots and their positions cannot be evaluated simultaneously with the coefficients. Therefore, several knot positions and numbers of knots were tested first on simulated data and later on data collected by the LHCb experiment. On one hand, too few knots cannot describe the data well enough such that the acceptance is smooth and not oscillating. On the other hand, too many knots would allow the acceptance function to describe not only the selection and reconstruction efficiency but also any effects from the oscillation of the B^0 mesons and the *CP* violation. At short decay times more knots are chosen because there are the highest changes in the acceptance and the density of the knots is correlated to the accuracy. The seven resulting knot positions are fixed to 0.2, 0.4, 0.9, 1.6, 5.0, 10.0 and 15.0 ps since the cubic spline function with these seven knot positions can describe the simulated and collected data without oscillations. For technical reasons, one of the coefficients must be fixed as well. As only relative values contribute due to the normalisation the last coefficient is fixed to one. All other coefficients are left floating in the decay time model and the final *CP* violation model.

In Fig. 7.1 the acceptance for each year is shown for $B^0 \to J/\psi(\to \mu\mu)K^0_S$ decays, where the acceptance is calculated as the ratio of the blue data histogram and the decay PDF including effects from the resolution; see Sec. 7.2. For both other final states the acceptance looks similar. It can be seen that the acceptance function

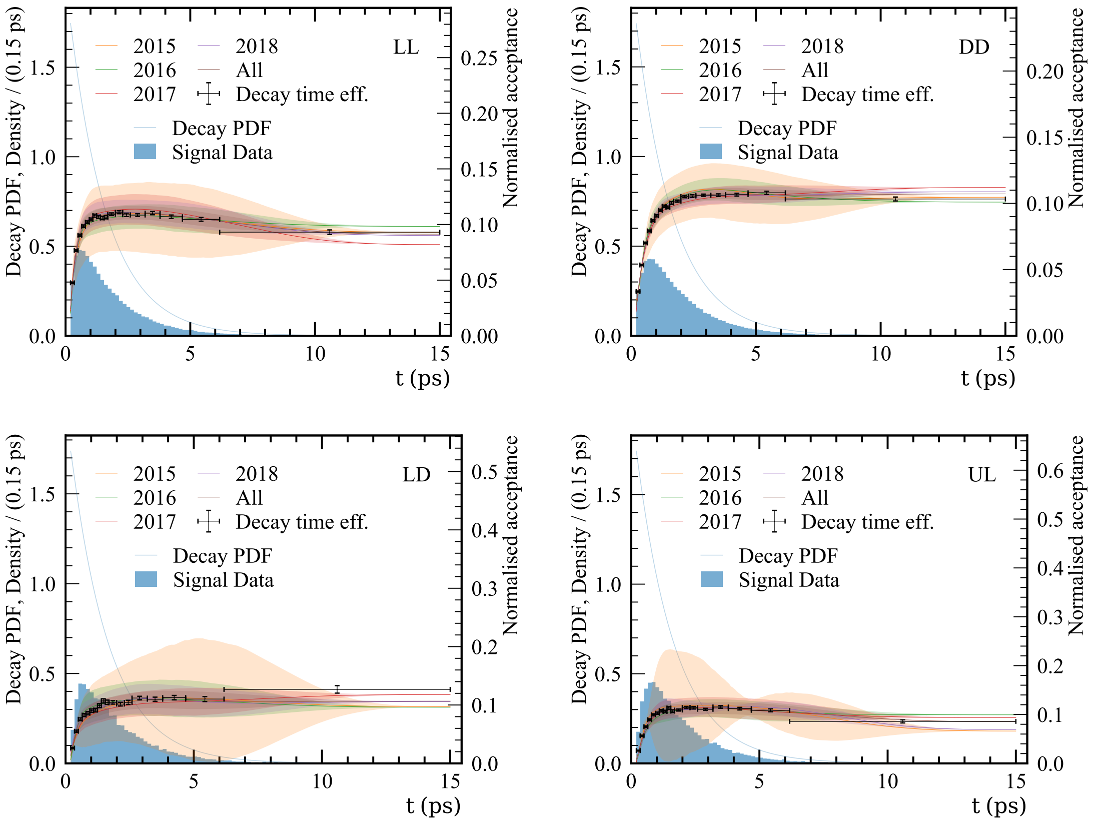

Figure 7.1: Acceptance functions for (orange) 2015, (green) 2016, (red) 2017, (purple) 2018 and (brown) all years combined with 1σ bands for (upper-left) LL, (upper-right) DD, (lower-left) LD and (lower-right) UL reconstructed K^0_S mesons in $B^0 \to J/\psi(\to \mu\mu)K^0_S$ decays. In blue the data and the decay PDF with resolution applied and in black the acceptance data. The data and acceptance functions are normalised such that the area under the curve between 0.2 and 10 ps is 1. The smallest data sets show fluctuations for small decay times.

has large uncertainties for the smallest data set of 2015, but nevertheless, all years match well. Therefore, one acceptance function is used for all years combined. In contrast, the acceptance varies for each track type significantly due to the different selections and separate cubic spline functions are required. The drop at large decay times, especially for LL and UL, was seen in previous studies with 2011 and 2012 data as well [32,111] and is caused by the reconstruction in the VELO. Fortunately, the cubic spline functions can describe this effect quite well. In addition, there is only a tiny fraction of data at these large decay times and any effect that is not modelled would not contribute significantly.

The acceptance functions for candidates, where the flavour tagging algorithms determine an initial flavour of the B^0 meson and those candidates, where no initial flavour could be determined, differ. This is the case because the determination of the flavour depends on the kinematical properties of the signal candidate and, thus, on the acceptance. More about this is explained in Ch. 8. Therefore, to estimate the CP violation parameters in the model, see Ch. 9, where the acceptance function is essential, only candidates are used where the flavour is identified.

In total, there are eight acceptance functions, one for each track type and each final state with the same seven fixed knot positions and different floating coefficients.

7.2 Decay time resolution

The determination of the vertex position and the momentum is finite in the LHCb experiment. Thus, the resolution of the decay time is measurable and needs to be considered in the description of the decay time as it directly influences the CP violation asymmetry and the value of $\sin(2\beta)$. On simulated samples the resolution can be estimated using the difference between the true and the reconstructed decay time. The distribution is described by the sum of three Gaussian functions. This results in a resolution averaged over all candidates. However, a more precise approach is to use a different resolution for each candidate. This can be achieved by an additional linear calibration of the decay time uncertainty through all candidates. The decay time resolution model of the j-th candidate can then be written as

$$\mathcal{R}(t'_j - t - \mu_{\text{bias}}|\sigma_{t_j}) = \sum_{g=1}^{3} f_g \cdot G(t'_j - t - \mu_{\text{bias}}; \sigma'_{g,t_j}), \quad \sigma'_{g,t_j} = c_g \sigma_{t_j} + b_g \,, \tag{7.1}$$

whereby the parameters b_g and c_g define the linear calibration and f_g the fraction of the g-th Gaussian function G. The last fraction is defined as $f_3 = 1 - \sum_{j=1}^{3-1} f_j$ to ensure the normalisation. The results are shown for DD reconstructed $B^0 \to J/\psi(\to \mu\mu)K^0_\text{S}$ and $B^0 \to J/\psi(\to ee)K^0_\text{S}$ candidates in Fig. 7.2. The mean is left floating for $B^0 \to J/\psi(\to ee)K^0_\text{S}$ candidates because a non-negligible bias was found, which is not present in both muon channels. This bias is one order of magnitude smaller than the bias found in data, described in Sec. 7.3. Therefore, no further change is needed to account for it.

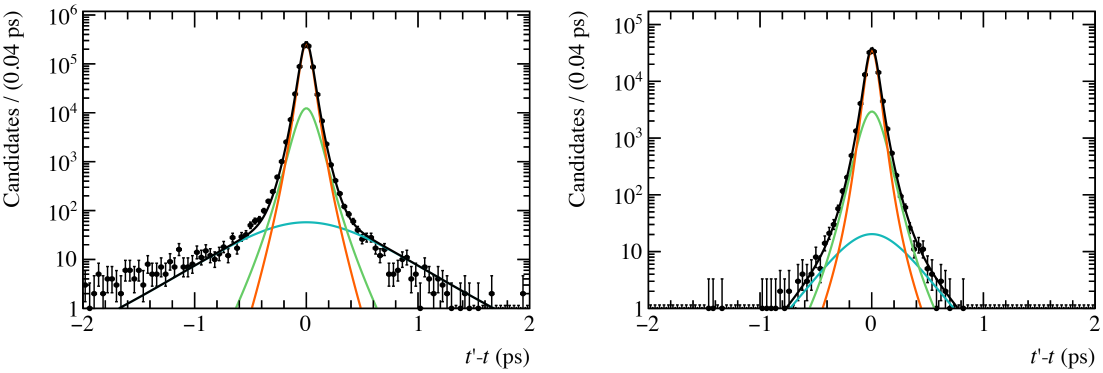

Figure 7.2: Per-candidate fit to the decay time resolution on signal simulation for DD reconstructed (left) $B^0 \to J/\psi(\to \mu\mu)K^0_\mathrm{S}$ and (right) $B^0 \to J/\psi(\to ee)K^0_\mathrm{S}$ candidates with (black) the sum of three Gaussian functions and (coloured) the single Gaussian functions.

The effect of the finite resolution on the decay time can be estimated with the dilution D given by

$$D = \int_{-\infty}^{\infty} \mathcal{R}(t)\cos(\Delta m t)\mathrm{d}t, \tag{7.2}$$

with the resolution function $\mathcal{R}$ and the oscillation frequency Δm. A value of one corresponds to a perfect resolution. In the case of a resolution model described by Gaussian functions the dilution simplifies to

$$D = \sqrt{\frac{1}{N}\sum_j^N D_j^2}, \tag{7.3}$$

where N is the total number of candidates and D_j is the per-event dilution of the candidate. It is calculated as

$$D_j = \exp\left(-\frac{1}{2}\sigma_j^2 \Delta m^2\right), \tag{7.4}$$

with the calibrated per-event resolution σ_j. The dilution is listed separately for all decays and each track type in Table 7.1. The dilution is nearly one for all channels, and thus, the effect on the resolution is negligible. A possible check for the dilution on simulated candidates is to use the difference between true and measured lifetime, Δt_j. The dilution is computed as

$$D = \sqrt{\frac{1}{N}\sum_j^N \cos^2(\Delta m \Delta t_j)}. \tag{7.5}$$

The results are similar with sub-permille differences and over 99.9 %. The negligible effects from the resolution are caused by the relatively short oscillation frequency

Table 7.1: Dilution in % for each decay channel and track type, evaluated on signal simulation using a per-event resolution. The uncertainties originate from the parameter uncertainties in the model from Eq. (7.1) and the results shown in Fig. 7.2.

Track type	LL	DD	LD	UL
$B^0 \to J/\psi(\mu^+\mu^-)K^0_S$	99.9397 ± 0.0016	99.9607 ± 0.0010	99.9370 ± 0.0026	99.922 ± 0.006
$B^0 \to J/\psi(e^+e^-)K^0_S$	99.956 ± 0.005	99.9656 ± 0.0017		
$B^0 \to \psi(2S)K^0_S$	99.9501 ± 0.0020	99.9639 ± 0.0014		

$\Delta m = (0.5065 \pm 0.0019)\,\mathrm{ps}^{-1}$ [40] of the B^0 mesons, which results in a long oscillation period of around 2000 fs. In comparison, the effective resolution of the detector calculated from the total dilution and the oscillation frequency as

$$\sigma_{\mathrm{eff}} = \sqrt{\frac{-2\ln(D_{\mathrm{total}})}{\Delta m^2}}. \tag{7.6}$$

results in between 53 to 76 fs, which is more than one order of magnitude lower than the oscillation period.

In summary, the finite resolution of the detector can be estimated and is taken into account with fixed parameters in the final *CP* violation fit, although the effect is negligible.

7.3 Decay time bias on prompt data

Effects on the decay time that exist in data but are not in simulations are studied with prompt data. Prompt data refers to data where no real B^0 meson is present, but the J/ψ and K^0_S mesons are produced directly from the *pp* collision. This study is only performed for $J/\psi \to \mu\mu$ decays, the channel with the highest statistics. Both other final states are expected to behave the same because the resolution models are similar as well as the resulting effective resolution. Furthermore, the decay time is mainly affected by the reconstruction of particles in the VELO, which are the same for $J/\psi \to \mu\mu$ and $\psi(2S) \to \mu\mu$ decays. The uncertainty of the reconstruction of electrons is worse and, therefore, effects on the decay time are more blurred in $J/\psi \to ee$ decays. The resolution can be estimated from the negative reconstructed decay times as the true decay time is zero. The selection of the signal candidates from Ch. 5 is adapted to avoid requirements on the decay time. To account for the background contributions the resolution model contains three exponential functions, which are unnecessary for simulated decays. Except that the model is the same as in Sec. 7.2. One example of the resolution is shown in Fig. 7.3. The mean of the resolution is shifted around 10 fs towards negative decay times, which is caused by a VELO misalignment in the reconstruction. To account for this, the data is split into 20 equally filled bins of the decay time uncertainty and the mean is evaluated in each bin. A quadratic function describes the dependency, which can be seen for

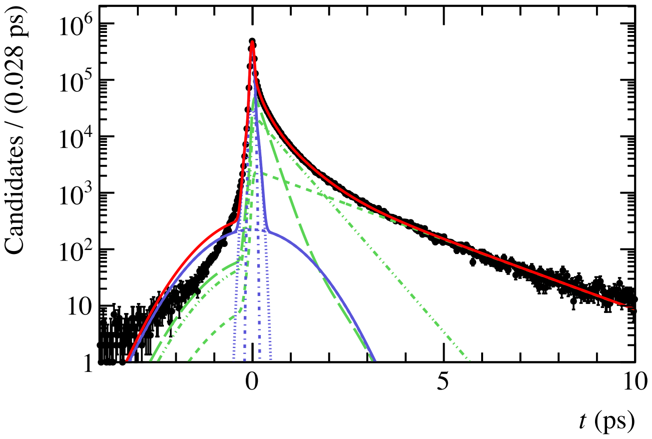

Figure 7.3: Fit to the mean decay time resolution on prompt J/ψ data for LL reconstructed $B^0 \to J/\psi(\to \mu\mu)K^0_S$ candidates with the sum of three Gaussian functions (purple, solid) and the single Gaussian functions (purple, dashed like) with three exponential functions (green, dashed like) and the overall model in red.

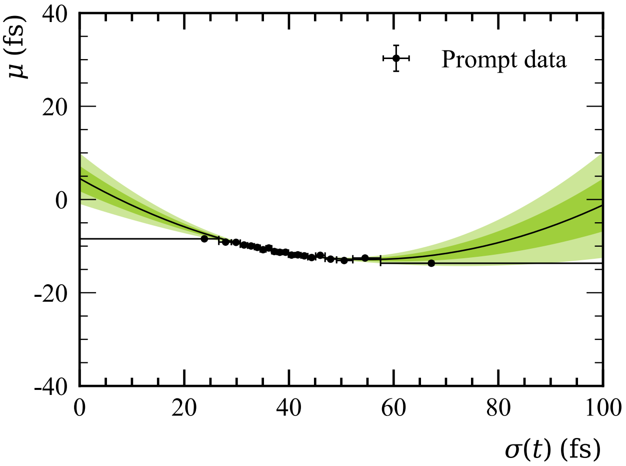

Figure 7.4: Mean of the resolution for different bins of the decay time uncertainty estimate for LL reconstructed candidates. A quadratic function with 1σ and 2σ uncertainty bands describes the data points.

LL reconstructed candidates on the right side of Fig. 7.4. These functions are used to calibrate the decay time in the *CP* violation model. In addition, it was checked that the procedure to use a linear calibration for the decay time uncertainty holds in the estimation of the per-event decay time resolution. More information about this approach can be found in Ref. [36].

The decay time bias is estimated relying entirely on prompt data and it is necessary to prove that the decay time bias is the same on prompt and detached data samples. The leading source for the decay time bias is the VELO misalignment, more specifically, the misalignment of the x-coordinate [71]. To test this effect, simulated prompt and signal data are generated, where the x-layer of the VELO halves is shifted from 0 to 9 µm in steps of 1 µm. After the same selection described above the resolution is modelled with three Gaussian functions for all simulated samples, where all Gaussian functions share the same mean. In Fig. 7.5 both prompt and detached simulated data samples with a shift of 8 µm are shown as an example. In Fig. 7.6 the mean of the resolution model is compared for each shift of the VELO.

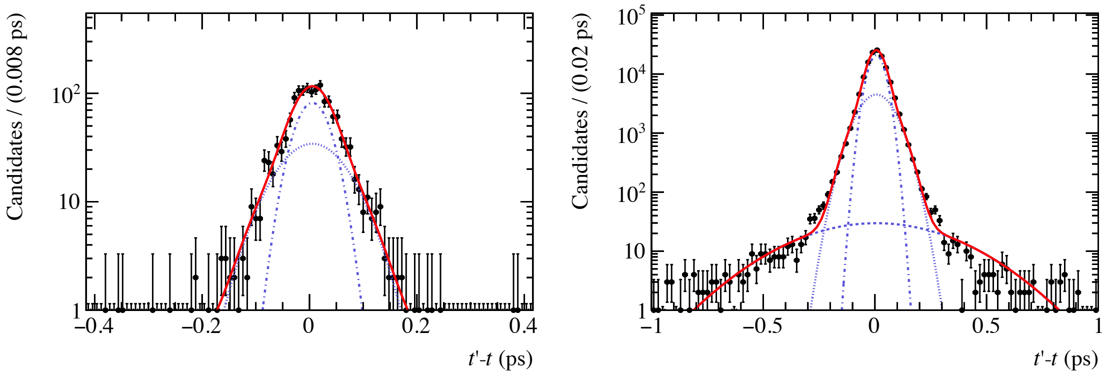

Figure 7.5: Fit to the mean decay time resolution on (left) prompt $J/\psi K^0_S$ simulation and (right) signal simulation with all track types combined with a VELO shift of 8 µm. The striped blue lines are the single Gaussian functions, the red line is the combination and the black points are the data points. The resolutions of the other VELO shifts look similar.

A clear linear dependency can be seen. The values for a linear model are

$$a = 0.000 \pm 0.000, \tag{7.7}$$

$$b = 1.116 \pm 0.081. \tag{7.8}$$

The values are compatible with unity and, therefore, the estimated mean on a prompt sample is the same on the signal sample and no calibration is needed. Furthermore, a systematic uncertainty for the decay time bias model is included; see Sec. 10.2 for more details. The uncertainties are bigger for the prompt sample because the amount of simulated samples is smaller. Since the calibration function is compatible with unity, no additional prompt data samples were simulated to decrease the uncertainty.

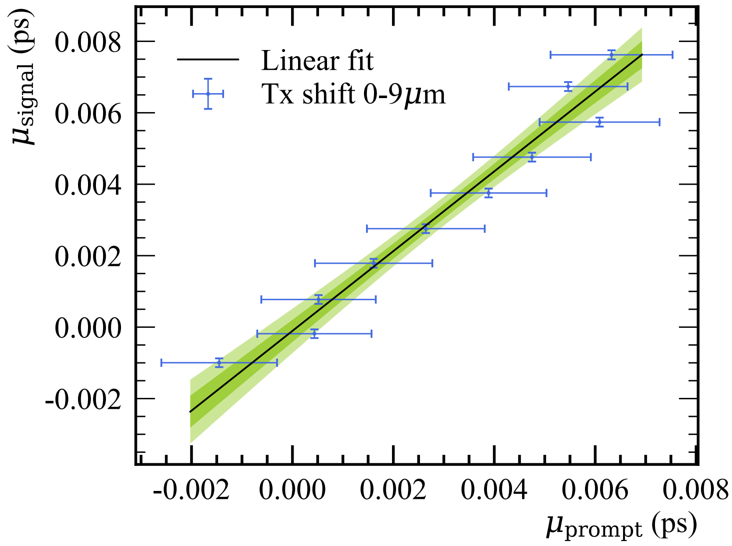

Figure 7.6: Mean bias from simulated prompt data on the x-axis and from simulated signal data on the y-axis, where the blue points and uncertainties result from fits to the decay time resolution with a floating mean. A linear calibration function describes the decay time bias from simulated prompt data to simulated signal data in black with one and two sigma bands in green.

8 Flavour tagging

For time-dependent *CP* violation measurements, it is important to know the initial flavour of the B^0 mesons. For some decays like $B^0 \to J/\psi K^{*0}$ this is straightforward because they are self-tagging, which means that the charge of the final state particles depends on the flavour of the initial B^0 meson. In this example, the K^{*0} meson from a B^0 meson decays into a K^+ and π^- meson. In contrast, the $\overline{K}^{*0}$ meson from a $\overline{B}^0$ meson decays into a K^- and π^+ meson and, therefore, the charge of the kaon and pion specify the flavour of the initial meson. This is not the case for other decays like $B^0 \to \psi K^0_\mathrm{S}$ because its final state is the same for an initial B^0 and $\overline{B}^0$ meson. Thus, it is more complex and needs another approach. This approach requires self-tagging control channels to determine a calibration function. For these control channels the decays $B^0 \to J/\psi(\to \ell\ell)K^*(\to K^\pm\pi^\mp)$ and $B^\pm \to J/\psi(\to \ell\ell)K^\pm$ with $\ell = \mu,\ e$ are used.

Details about the approach and a general overview of the flavour tagging are given in Sec. 8.1, while the selection of the control channels is discussed in Sec. 8.2. The necessary reweighting of the control channels to the signal channels is explained in Sec. 8.3 and the calibration of the flavour tagging algorithms in Sec. 8.4.

8.1 Flavour tagging algorithms at LHCb

Several tagging algorithms are implemented in the software of the LHCb experiment to predict the flavour of mesons at production. These algorithms have two variables as output. First, the tag decision (d) for the flavour of the meson and second, a measure of the uncertainty that the tagging decision is wrong, the mistag η. The mistag is defined between 0 and 0.5, where 0 means no uncertainty of the tagging decision and 0.5, that the flavour of the initial meson is not known and no tag decision is made.

A sketch of a pp collision including the signal decay and all particles relevant for the flavour tagging at LHCb is shown in Fig. 8.1. In the pp collision b quarks are produced in a $b\overline{b}$ quark pair due to gluon gluon fusion. The $\overline{b}$ quark hadronises with a d quark to the signal B^0 meson. But the d quark cannot occur alone. It is created as a $d\overline{d}$ quark pair. The remaining $\overline{d}$ quark hadronise like the $\overline{b}$ quark, for example, with an u quark to a π^+ meson or with two $\overline{u}$ quarks to a $\overline{p}$ baryon. The implemented algorithms, also called taggers, referring to these particles are called SS Pion or SS Proton, where SS means same side (SS) because these particles originate to the b quark forming the signal B^0 meson. The charge of the pion or proton determines the flavour of the initial B^0 meson because they are connected

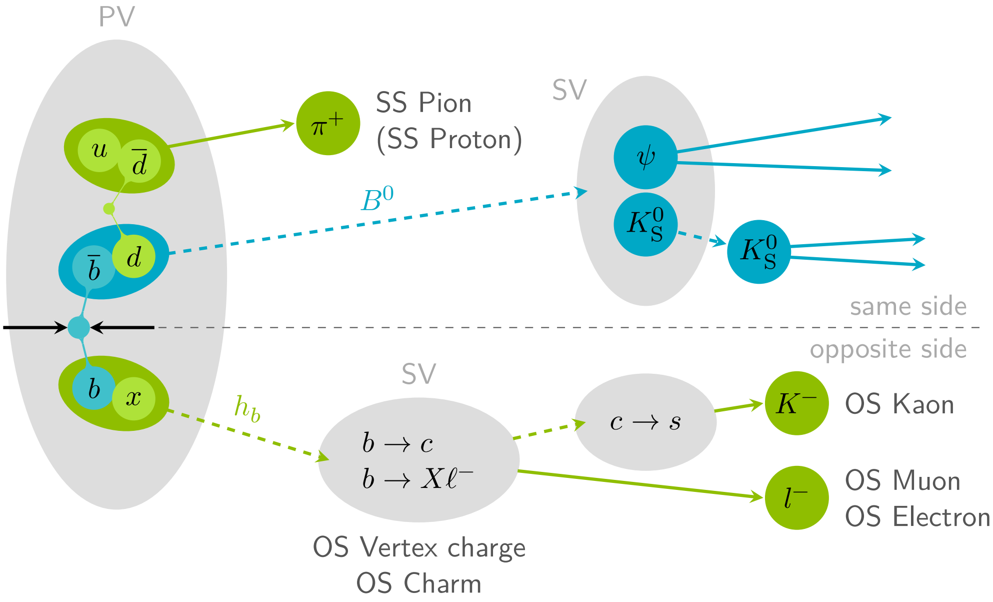

Figure 8.1: Sketch of a pp collision with all particles, which are analysed in the flavour tagging algorithms at the LHCb experiment.

through the $d\overline{d}$ quark pair. A negatively charged pion would need a d quark and for the B^0 meson would only remain a $\overline{d}$ quark, thus creating a $\overline{B}^0$ meson. This way, obtaining information about the initial flavour is possible, although the signal decay is not self-tagging.

Besides these algorithms, there are opposite side (OS) taggers as well. They are called OS because they use the b quark created by the pp collision at the beginning and did not form the signal decay. The naming derives from the fact that the b quark is on the opposite side of the signal decay. This b quark also hadronises and decays likewise on the signal side. Out of the charges of the decay products the flavour of the b quark and, therefore, the flavour of the signal B^0 meson can be determined. Five algorithms related to possible decay products are available: OS kaon, OS muon, OS electron, OS charm and OS vertex charge.

One of the immense challenges is that there are so many tracks in one pp collision that the classification of all particles is very complicated. All particles in the event, excluding the signal particles, are classified as originating from the SS or OS of the $b\overline{b}$ quark pair or from any other decay in the event. This is done with specific selection requirements optimised centrally by colleagues at the LHCb experiment; see Ref. [112, 113] for example. The predicted mistag probability is evaluated with a multivariate classifier trained on variables to separate the tagging particles from the signal particles and on variables for particle identification. However, the predicted mistag is not accurate and must be calibrated. This is done on self-tagging calibration channels, where the true mistag ω is known and defined as

$$\omega = \frac{N_{\text{false}}}{N_{\text{false}} + N_{\text{true}}} \tag{8.1}$$

with incorrectly (correctly) tagged events N_{false} (N_{true}). The data is split into equally filled bins of the predicted mistag η, and the true mistag ω is calculated in each bin. These data points of η versus ω can be described by a quadratic or linear model, resulting in a calibration function where a true mistag probability is allocated for each predicted mistag. One example for the SS Pion is shown in Fig. 8.2. To avoid the calibrated values outside of the range between 0 and 0.5 a link function like the logistic function $f(x) = \frac{1}{1+e^{-x}}$ is applied. The linear model is defined as

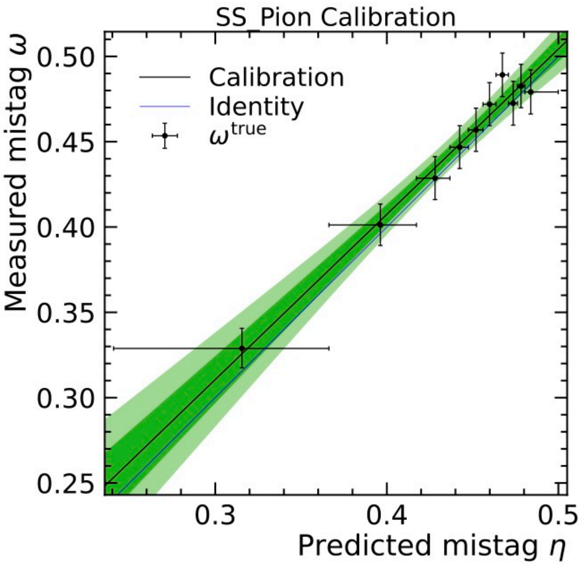

Figure 8.2: Flavour tagging mistag calibration of SS Pion using $B^0 \to J/\psi(\to ee)K^*(\to K^\pm\pi^\mp)$ decays. The calibration function is shown in black with the 1σ (dark green) and 2σ (light green) bands.

$$\omega(\eta) = p_0 + p_1(\eta - \langle\eta\rangle), \tag{8.2}$$

where the mean of the mistag ($\langle\eta\rangle$) is used to decrease the correlation between the parameters p_0 and p_1. The calibration is performed for B^0 and $\bar{B}^0$ tagged candidates separately and the mean and difference between both calibration function parameters, defined as

$$p_i = \frac{p_i^{B^0} + p_i^{\bar{B}^0}}{2}, \qquad \Delta p_i = p_i^{B^0} - p_i^{\bar{B}^0}, \qquad \text{with } i = 0,\, 1, \tag{8.3}$$

are included in the *CP* violation model, see Ch. 9. For a perfect tagger where the predicted mistag is equivalent to the true mistag, the flavour tagging calibration parameters would be defined as

$$\begin{aligned} p_0 &= \langle \eta \rangle, & p_1 &= 1, \\ \Delta p_0 &= 0, & \Delta p_1 &= 0. \end{aligned} \tag{8.4}$$

The whole calibration procedure is done with the *lhcb-ftcalib* software package [114].

At first, the calibration parameters are computed for all single taggers separately because they have different distributions of the predicted mistag η. Afterwards, the likelihood functions of each tagger for the flavour of the B^0 meson are combined into one likelihood function, which is used to estimate the combined tag decision and mistag. Thereby, possible different tagging decisions and the decrease for the overall mistag with the same decision of multiple taggers are considered. The combination is performed individually for all OS and SS taggers because the underlying physics processes are significantly different. Afterwards, the resulting two taggers must be calibrated again due to the varying correlation between the single taggers for each event. More detailed information about the calibration and combination can, for example, be found in Ref. [113].

To evaluate the performance of the flavour tagging some key properties are essential, *e.g.* the tagging efficiency ε_{tag}, which is the ratio of tagged and all candidates. This efficiency is different for B^0 and $\overline{B}^0$ candidates due to detection asymmetries of charged particles. Therefore, not only the mean of both tagging efficiencies $\langle \varepsilon_{\text{tag}} \rangle$ but also the difference $\Delta\varepsilon_{\text{tag}}$ is included in the *CP* violation model. Another relevant parameter is the flavour tagging dilution

$$D = 1 - 2\omega, \tag{8.5}$$

which represents the suppression of the measured *CP* parameters due to the imperfect tagging. At last, the effective tagging efficiency $\varepsilon_{\text{tag,eff}}$, sometimes named tagging power, is defined as the multiplication of tagging efficiency and squared dilution

$$\varepsilon_{\text{tag,eff}} = \varepsilon_{\text{tag}} D^2. \tag{8.6}$$

The tagging power is the proportion of events with the same statistical sensitivity as if this proportion would have perfect tagging.

8.2 Selection of control channels for flavour tagging

As described above in Sec. 8.1, control channels are necessary for the signal channels to calibrate the mistag because they are not self-tagging. The calibration channels are chosen to be similar to the signal channels but also with a high statistic to decrease the uncertainties of the resulting calibration parameters. For the same reason, identical calibration channels are used for both muonic signal channels.

The best-suited calibration channel is $B^{\pm} \to J/\psi(\to \ell\ell)K^{\pm}$ with $\ell = e,\ \mu$ due to possible efficient selection requirements, a similar topology and the disability of the $B^{\pm}$ meson to oscillate. Thus, the same flavour at production and decay. However, it is only used for the OS taggers because the initial $B^{\pm}$ meson has an u quark instead of a d quark and, thus, the SS flavour tagging particles are built differently. The OS taggers are unaffected as it only depends on the b quark. The $B^0 \to J/\psi(\to \ell\ell)K^*(\to K^{\pm}\pi^{\mp})$ decay with $\ell = e,\ \mu$ is used for the SS taggers with the same topology and comparable kinematic properties. These decays are not used for all taggers because they have a worse reconstruction and selection efficiency and a better statistical uncertainty significantly improves the flavour tagging calibration parameters.

Recorded data is used for the flavour tagging calibration instead of simulated samples because the simulation of the underlying event, which is essential for the tagging algorithms, is complicated and not perfectly reliable. However, the background candidates have to be removed from the data and a tight selection is mandatory. The selection is done in two steps. At first, basic one-dimensional requirements, the preselection, are applied to different variables, including trigger requirements, followed by a multivariate selection. The selection is analogous to the signal selection, which has the advantage that the distributions between signal and control channels are more similar and the portability of the flavour tagging calibration functions is better.

The preselection for the control channel $B^0 \to J/\psi(\to \mu\mu)K^*(\to K^{\pm}\pi^{\mp})$ is based on the reconstructed-mass of the combined mesons, the decay time of the B^0 meson, the shortest distance of the B^0 track to the PV and the vertex quality of the J/ψ and K^* meson. Moreover, requirements are applied to the transverse momentum of the pion, both kaons and the muon, to particle identification variables of the final state particles, the track quality of the kaon and pion and the separation of the final state particles from the PV. With these variables background candidates are reduced, *e.g.* the particle identification variables help to avoid misidentified background while the requirement of the decay time of the B^0 meson reduces the amount of combinatorial background. In the same way, the vertex quality or the track quality constrains the particles to originate from the same vertex and not from a different decay. The preselection for $B^{\pm} \to J/\psi(\to \mu\mu)K^{\pm}$ is very similar with additional requirements on the momentum of the kaon and a vertex quality on the B^0 meson. The preselection for the electron channels is slightly different, but mainly in the extent of the requirements above.

The applied trigger lines are the same as in the signal channel selection, which can be seen in Table 5.1. Furthermore, it is required that all DTF reconstructions converge on all candidates and the global reconstruction quality χ^2_{DTF} is below 50 with the constrained J/ψ mass.

The multivariate selection is based on an XGB classifier [102] with most parameters close to the multivariate selection as in the signal channels; see Sec. 5.2 for details. It is used a fivefold KFolding [103] with the simulation as the signal proxy and the upper sideband of the reconstructed-mass of the B^0 meson as the background proxy. The mass is required to be greater than 5400 MeV/c^2 (5350 MeV/c^2) in the muonic SS (OS) calibration channel and greater than 5450 MeV/c^2 for both electron calibration channels. The limits on the mass are higher for the electron channels because the signal shape is wider due to the worse reconstruction and no signal candidates should be used for the background proxy. In contrast to the signal channels, the figure of merit for the requirement on the BDT output is chosen to reach a sensitivity $\frac{S}{S+B}$ with the number of signal and background candidates S and B of 99.9 % (99 %) for the muonic SS (OS) calibration channel and 95 % for both electron calibration channels. This measure is used to achieve the goal of very pure signal samples without much background. After the full selection around 1.2 M (3.5 M) signal candidates are left for $B^0 \to J/\psi K^*$ ($B^\pm \to J/\psi K^\pm$) in the muon channel and around 89 k (142 k) candidates in the electron channel. The signal component is described with a double-sided crystal ball function [115], a very similar model as the Hypatia model explained in Ch. 6, and a Gaussian function, where the mean is shared. The background model includes the combinatorial background described by an exponential function, a partially reconstructed background at lower masses in the OS control channel and the $B_s^0 \to J/\psi(\to \ell\ell)K^*(\to K^\pm\pi^\mp)$ component in the SS control channel, which shares all parameters with the signal decay except the shifted mean to the B_s^0 meson mass. The invariant mass of the B^0 meson in the electron channels is computed with a fixed mass of the J/ψ to its known mass [40] for a better resolution. In the muon channels this is not required due to the more precise reconstruction of the muons. In Fig. 8.3 the B^0 mass is shown for $B^\pm \to J/\psi(\to ee)K^\pm$ and $B^0 \to J/\psi(\to ee)K^*(\to K^\pm\pi^\mp)$ after the entire selection. It can be seen that nearly only signal candidates are left after the selection.

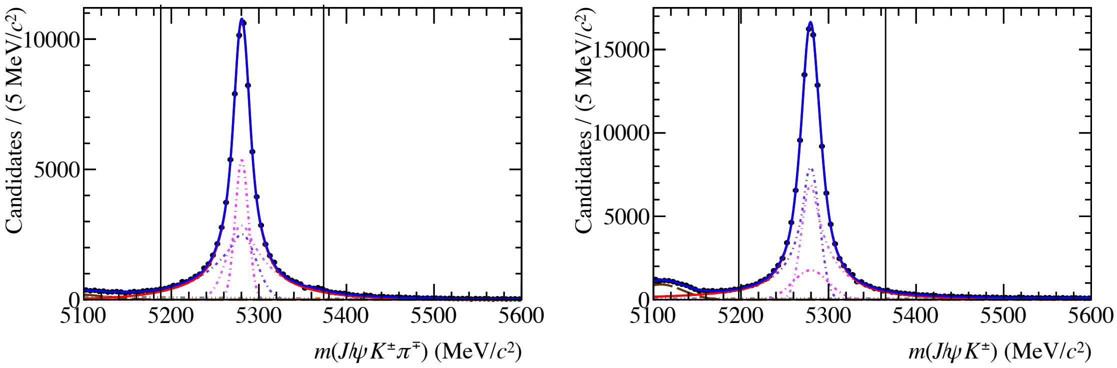

Figure 8.3: Invariant mass of $B^0 \to J/\psi(\to ee)K^*(\to K^\pm\pi^\mp)$ ($B^\pm \to J/\psi(\to ee)K^\pm$) candidates after the entire selection on the left (right) including the signal component (red), described by the sum of two crystal ball functions with tails toward lower and higher masses (blue and purple dotted) and a Gaussian function (pink dotted), B_s^0 mesons (orange) with the same model, combinatorial background (grey) with an exponential function and partial background (brown) modelled with a Gaussian function. The black lines indicate the interval where the number of candidates is evaluated for the FoM of the BDT.

In the muon channels this is even more the case. In the same way as in the signal channels, see Ch. 6, sWeights are computed from these mass distributions to unfold the signal component.

8.3 Reweighting of flavour tagging control channels

The flavour tagging mistag depends on the kinematic of the decay. However, the kinematic properties are different for the signal and control channels, which are used to calibrate the mistag. Therefore, it is necessary to take this into account. This is done by reweighting the distributions of the kinematic variables of the control channel to the signal channel. This means that weights are computed, which are applied to the distributions of the control channel, such that these distributions match the ones from the signal channel. More than one kinematic property correlates with the mistag and, thus, five variables are chosen, where all variables are reweighted simultaneously. The variables are the transverse momentum, the pseudorapidity and the ϕ angle in the detector of the B^0 meson as well as the number of tracks and number of reconstructed primary vertices in the event. The used reweighting procedure is BDT-based, referred to as GBReweighting [116]. It has the advantage of preventing the curse of dimension [117]. In Fig. 8.4 the pseudorapidity of the B^0 meson in the electron modes is shown before and after the reweighting. The distribution of the signal channel and both control channels before the reweighting have diverged. However, after the reweighting the distributions match well. The same applies to the other variables as well as both muon modes. The simulated control channels are reweighted, too, but the simulated signal samples are chosen to match.

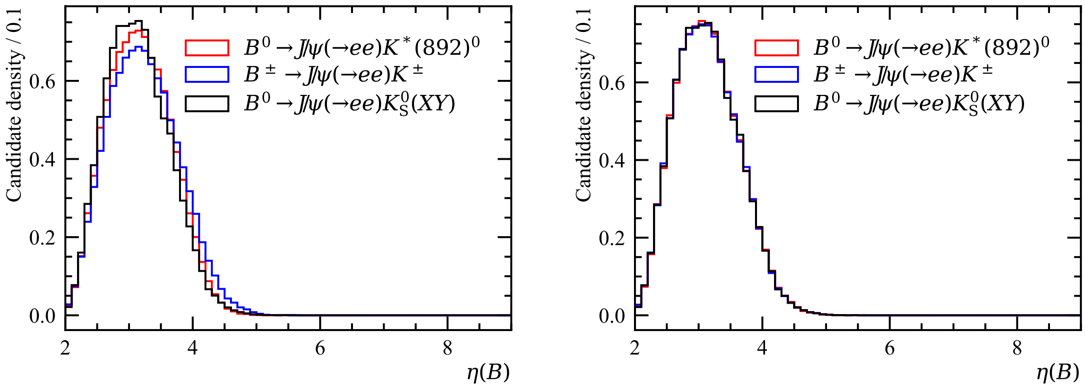

Figure 8.4: Pseudorapidity $\eta(B^0)$ (left) before reweighting and (right) after reweighting for (red) $B^0 \to J/\psi(\to ee)K^*(\to K^\pm\pi^\mp)$, (blue) $B^\pm \to J/\psi(\to ee)K^\pm$ and (black) $B^0 \to J/\psi(\to ee)K^0_S$ for all years combined.

8.4 Tagging calibration parameters for the signal

As described in Sec. 8.1, several flavour tagging algorithms exist at the LHCb experiment. All taggers are used, totalling two taggers for the SS and five for the OS. They are listed in Table 8.1. For each single tagger, a calibration function is determined on the associated control channels for the SS and OS individually. This is done on data, where the kinematical and topological differences are corrected with weights; see Sec. 8.3. The calibration functions are then applied to the signal data, where all taggers are combined into one OS and one SS tagger. The same could be done for the calibration of the combined OS and SS taggers, but a more sophisticated approach is used.

Table 8.1: List of calibrated tagging algorithms for the opposite side and same side.

OS	SS
OS Muon	SS Pion
OS Electron	SS Proton
OS Kaon	
OS Charm	
OS Vertex Charge	

The decay time of the selected $B^0 \to J/\psi K^*$ data sample is modelled including *CP* violation and all available flavour tagging information. More about this model is described in Ch. 9. By fitting the decay time with this model the calibration functions for the OS and SS tagger are determined. However, using only $B^0 \to J/\psi K^*$ decays the higher statistic and, thus, the more precise calibration parameters for the OS tagger determined from $B^\pm \to J/\psi K^\pm$ decays would be neglected. That is why those parameters are constrained with a Gaussian function with the mean and width from the calibration in the $B^\pm \to J/\psi K^\pm$ decays. This way, the whole statistic of both control channels is used. The fit to the decay time has the advantage that the production asymmetry, defined as the difference between the number of created $\overline{B}^0$ and B^0 mesons in the pp collision, and the flavour tagging efficiency asymmetries, defined as the difference between the tagging efficiency of $\overline{B}^0$ mesons and B^0 mesons, can be measured simultaneously. Furthermore, all flavour tagging calibration parameters are computed from one single fit. Thus, any correlations between the production asymmetry, the flavour tagging efficiency asymmetries and all flavour tagging calibration parameters are taken into account. A detailed description of this approach and how these parameters are included in the final *CP* violation model is given in Sec. 9.1.

The resulting flavour tagging performances for the combined OS and SS taggers on data can be seen in Table 8.2. The performances are similar for the two muon channels, which is expected because the same control channels are used and only the signal kinematic distributions differ. In contrast, the electron channel has a

Table 8.2: Flavour tagging performances of the combined taggers in the signal data samples after the entire selection for all years combined. The uncertainties include the statistical uncertainty of the data sample and for the tagging power also the uncertainty from the calibration parameters.

Decay	OS Combination		SS Combination	
	$\epsilon_{\text{tag, eff}}$ [%]	ϵ_{tag} [%]	$\epsilon_{\text{tag, eff}}$ [%]	ϵ_{tag} [%]
$B^0 \to J/\psi(\to \mu\mu)K^0_S$	$2.57 \pm 0.01 \pm 0.02$	35.80 ± 0.08	$1.16 \pm 0.01 \pm 0.03$	78.88 ± 0.07
$B^0 \to \psi(2S)K^0_S$	$2.51 \pm 0.04 \pm 0.02$	35.39 ± 0.30	$1.21 \pm 0.02 \pm 0.03$	79.41 ± 0.25
$B^0 \to J/\psi(\to ee)K^0_S$	$3.27 \pm 0.04 \pm 0.12$	36.98 ± 0.24	$1.98 \pm 0.02 \pm 0.18$	87.01 ± 0.17

higher performance. In the SS this can be explained due to the tighter selection and, therefore, a higher B^0 meson momentum. As the momentum is correlated to the mistag the tagging power increases. The second reason, which is more important for the improvement of the OS tagger, is the choice of the trigger lines. In the electron channel the lines are not only triggered on signal properties but also on the properties of the event independent of the signal. In events triggered independently of the signal candidates, the particles not included in the signal must be well-reconstructed. Therefore, the candidates essential for the flavour tagging are well-reconstructed leading to a higher flavour tagging performance. The same trigger selection is not used for both muon channels due to the excellent background suppression of the used trigger lines.

9 Extraction of *CP* violation parameters

The *CP* violation parameters are extracted from a fit to the decay time of the B^0 meson. The description of the decay time also considers the mixing of the neutral B^0 mesons, the *CP* violation and the resolution of the decay time. This results in a model that can be written as

$$\begin{aligned}\mathcal{P}^{CP}(t,\vec{d},\vec{\omega}) = \Theta(\vec{\xi})\epsilon(t)\int_0^\infty e^{-\Gamma t'}\Bigg[&\mathcal{S}(\vec{d},\vec{\omega})\sin(\Delta m t') + \mathcal{C}(\vec{d},\vec{\omega})\cos(\Delta m t')\\ &+ \mathcal{A}_{\Delta\Gamma}(\vec{d},\vec{\omega})\sinh\left(\frac{1}{2}\Delta\Gamma t'\right) + \cosh\left(\frac{1}{2}\Delta\Gamma t'\right)\Bigg]\mathcal{R}(t-t'|\sigma(t))\,\mathrm{d}t'.\end{aligned} \tag{9.1}$$

The parameter $\Theta(\vec{\xi})$ expresses external parameters constrained with a Gaussian function. This includes the eight flavour tagging calibration function parameters p_i, and Δp_i with $i = 0, 1$ for OS and SS, the production asymmetry $\mathcal{A}_{\text{prod}}$ defined as the difference of produced $\overline{B}^0$ and B^0 mesons in the *pp* collisions, the decay width Γ and the oscillation frequency of the B^0 meson Δm. The time-dependent selection and reconstruction efficiency, denoted as $\epsilon(t)$, is explained in detail in Sec. 7.1. The core of the decay time model is the exponential function with the decay width. The per-event resolution model $\mathcal{R}$ is estimated on simulation with more information given in Sec. 7.2. The parameters $\vec{d}$ and $\vec{\omega}$ are the tagging decisions and calibrated mistags, respectively, for OS and SS. The decay width difference $\Delta\Gamma$ of the B^0 mesons is set to zero. The *CP* violation parameters $\mathcal{S}$, $\mathcal{C}$ and $\mathcal{A}_{\Delta\Gamma}$ take the flavour tagging dilutions and intrinsic asymmetries into account. For tagged candidates, they are defined as

$$\begin{aligned}\mathcal{S}(\omega,d) = -(1+\mathcal{A}_{\text{det}})\ &\Bigg(d\varepsilon_{\text{tag}} - \frac{\Delta\varepsilon_{\text{tag}}}{2} - 2d\varepsilon_{\text{tag}}\langle\omega\rangle + d\frac{\Delta\varepsilon_{\text{tag}}}{2}\Delta\omega\\ &-\mathcal{A}_{\text{prod}}\left(\varepsilon_{\text{tag}} - d\frac{\Delta\varepsilon_{\text{tag}}}{2} - d\varepsilon_{\text{tag}}\Delta\omega + d\Delta\varepsilon_{\text{tag}}\langle\omega\rangle\right)\Bigg)\,S\end{aligned} \tag{9.2}$$

$$\mathcal{C}(\omega,d) = -\mathcal{S}(\omega,d)\times\frac{C}{S} \tag{9.3}$$

$$\begin{aligned}\mathcal{A}_{\Delta\Gamma} = \quad & (1+\mathcal{A}_{\mathrm{det}})\left(\varepsilon_{\mathrm{tag}} - d\frac{\Delta\varepsilon_{\mathrm{tag}}}{2} - d\varepsilon_{\mathrm{tag}}\Delta\omega + d\Delta\varepsilon_{\mathrm{tag}}\langle\omega\rangle \right.\\ & \left. - d\mathcal{A}_{\mathrm{prod}}\left(\varepsilon_{\mathrm{tag}} - d\frac{\Delta\varepsilon_{\mathrm{tag}}}{2} - 2\varepsilon_{\mathrm{tag}}\langle\omega\rangle + \frac{\Delta\varepsilon_{\mathrm{tag}}}{2}\Delta\omega\right)\right)A_{\Delta\Gamma}\end{aligned} \tag{9.4}$$

The detection asymmetry $\mathcal{A}_{\mathrm{det}}$ is zero due to the charge symmetrical final states. The tagging efficiency asymmetry $\Delta\varepsilon_{\mathrm{tag}}$ is defined as the difference of the tagging efficiency of $\overline{B}^0$ and B^0 mesons, while $\Delta\omega$ and $\langle\omega\rangle$ are defined as the difference and mean of the calibrated mistag for B^0 and $\overline{B}^0$ mesons. The remaining parameters S, C and $\mathcal{A}_{\Delta\Gamma}$ are the physical *CP* violation parameters defined in Eqs. (2.24) to (2.26). Independent *CP* violation fits are performed for each decay channel. Furthermore, fits are performed with separated and shared *CP* violation parameters for each track type. In addition, the fits are split into each year for the simulated data. All *CP* violation fits are performed on tagged candidates only because the sensitivity for the final *CP* violation parameters is the same. This way, any differences between tagged and untagged candidates, like the difference in the acceptance, see Sec. 7.1, can be ignored.

External parameters, *e.g.* the oscillation frequency of the B^0 meson, the production asymmetry or the flavour tagging calibration parameters, have uncertainties, which must be considered in the *CP* violation model. The approach behind this is discussed in Sec. 9.1. After the initialisation of the model, it has to be tested. These checks are performed on simulated data, where the *CP* violation parameters are determined for various complexity levels, described in Sec. 9.2. In the end, the results on data for the three decay channels are explained in Sec. 9.3.

9.1 External parameters

Physical parameters are used in the *CP* violation model, which are measured in different analyses. However, the uncertainty of these parameters must be considered. Therefore, the likelihood function, which is minimised to find the best parameters, is multiplied by a Gaussian function. The mean and sigma of the Gaussian function are chosen to account for the external parameters' mean and uncertainty. This is also called that the parameter is constrained. The following parameters are constrained:

- The mean lifetime τ of the B^0 mesons, and thus, the mean decay width Γ,
- The oscillation frequency Δm of the B^0 mesons,
- The four flavour tagging calibration parameters for OS and four for SS p_0, p_1, Δp_0 and Δp_1,
- The production asymmetry $\mathcal{A}_{\mathrm{prod}}$ of produced B^0 and $\overline{B}^0$ mesons

For the first two parameters, the mean and uncertainty are taken from Ref. [40]. In contrast, the other parameters are determined with one single fit to $B^0 \to J/\psi K^*$ decays. As briefly mentioned in Sec. 8.4, the decay time is fitted using the same model as for the signal channel as defined in Eqs. (9.1) to (9.4). This way, the flavour tagging calibration parameters, the flavour tagging efficiency asymmetries and the production asymmetry are determined. The model must be slightly changed to take into account that $B^0 \to J/\psi K^*$ decays are not *CP* eigenstates and have no *CP* violation. This is done by fixing the *CP* violation parameter to

$$S = \overline{S} = 0, \tag{9.5}$$

$$C = -\overline{C} = 1, \tag{9.6}$$

where S and C correspond to B^0 mesons and $\overline{S}$ and $\overline{C}$ to $\overline{B}^0$ mesons. Furthermore, not only tagged candidates are considered but also untagged candidates to disentangle the production asymmetry and the flavour tagging efficiency asymmetry. Both parameters can be determined because the decay is flavour-specific for both initial flavours of the B^0 mesons due to the charge of the kaon and pion. Moreover, the final state is no longer symmetrical and the detection asymmetry is considered as well. All flavour tagging parameters are left floating because they are used as input values for the *CP* violation model in the signal channels. To take the high statistic of the $B^\pm \to J/\psi K^\pm$ decays into account the flavour tagging calibration parameters of the OS tagger are constrained in the fit by Gaussian functions, where the resulting calibration parameters from the OS calibration with $B^\pm \to J/\psi K^\pm$ decays are used for the mean and sigma. The huge advantage of the single fit is that not only correlations between the OS and SS calibration parameters are considered and accessible for the final fit to data but also correlations between the production asymmetry, the flavour tagging calibration parameters and the flavour tagging efficiency asymmetry. Background candidates are omitted with sWeights and to account for kinematical and topological differences between signal and $B^0 \to J/\psi K^*$ decays GBweights are included. More details about these weights can be found in Secs. 8.2 and 8.3.

The sensitivity to the production asymmetry is lower for the electron channel than for the muon channel due to the smaller statistic. This would lead to higher uncertainty and a too-loose constraint in the *CP* violation model. Nevertheless, because the production asymmetry is the same for both decays, it is constrained by a Gaussian function in the electron channel with the results from the fit to the $J/\psi \to \mu\mu$ channel. This is not done for the flavour tagging parameters because the predicted mistag differs for all three final states. The determined flavour tagging efficiency asymmetry is compatible with zero but nevertheless applied and fixed in the *CP* violation model in the signal. The portability from this parameter is checked and included as a systematic uncertainty; see Sec. 10.2.

9.2 *CP* violation parameters on simulated samples

A very stringent check whether the used model describes the data and does not bias the result is a fit to simulated data, where the generation values of the *CP* violation parameters are known. In the following, three tests are described, where different complexity levels are used for the *CP* violation model.

CP violation parameters on simulated samples with the true initial flavour of the B^0 meson

In simulated data is access to the true flavour of the B^0 meson, also called true ID. This can be used to simplify the *CP* violation model by using these flavours for the tagging decision and fixing the estimated mistag to $\eta = 0$. This way, all uncertainties due to the flavour tagging are left out and the remaining parts of the model, *e.g.* the acceptance description, are tested. In Fig. 9.1 the results can be seen for S and C for $B^0 \to J/\psi(\to \mu\mu)K^0_S$ simulated decays. The fits are performed separately for each year of data taking and the red bands represent the weighted mean of all measurements. The results match the generated value of 0.7 for S and 0.0 for C. These values are chosen for the generation because these values are predicted by the SM and match previous measurements. The results of the other two final states are similar. This proves that the *CP* violation model can describe the data.

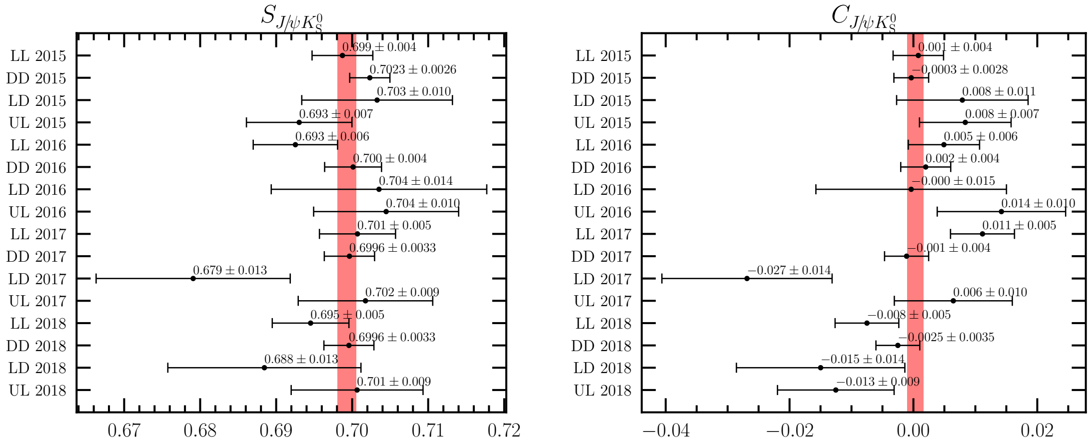

Figure 9.1: *CP* fit results of (left) S and (right) C of simulated $B^0 \to J/\psi(\to \mu\mu)K^0_S$ decays where the true flavour is used for the initial flavour of the B^0 mesons. The generated value is 0.7 and 0.0, respectively, which is roughly the measured value in previous measurements. The red bands represent the weighted mean of all measurements.

CP violation parameters on simulated samples with flavour tagging calibration with the true flavour

A complication is the usage of a flavour tagging calibration for the mistag η. The true IDs of the simulated signal data are used for calibration. This way, the mistag is calibrated, but the uncertainty of the portability of the flavour tagging calibration from the control channels to the signal channel is still omitted because only the signal simulated samples are used. Any constraints to the lifetime and oscillation frequency of the B^0 mesons and the production asymmetry are neglected as the initial values are known, and the flavour tagging calibration parameters and efficiencies are fixed in the fit for simplifications. In Fig. 9.2 the results are shown for S and C for $B^0 \to J/\psi(\to \mu\mu)K^0_\mathrm{S}$ simulated decays. The fits are performed separately for each year of data taking and the blue bands represent the weighted mean of all measurements. The weighted means of S and C differ from the simulated values of about 2σ. The result on S for $B^0 \to \psi(2S)K^0_\mathrm{S}$ differs around 2σ, too, while it matches the generated value for $B^0 \to J/\psi(\to ee)K^0_\mathrm{S}$ decays. On C the results match the generated values as well. Overall, the results fit the generated values in the electron channel, while they diverge for both muon channels. So, the calibration is not perfectly accurate. However, the uncertainty is smaller than on data and therefore, the discrepancy is less significant. In addition, it proves that the flavour tagging calibration, in principle, is possible, especially because the calibration from the control channels is the calibration later used on data.

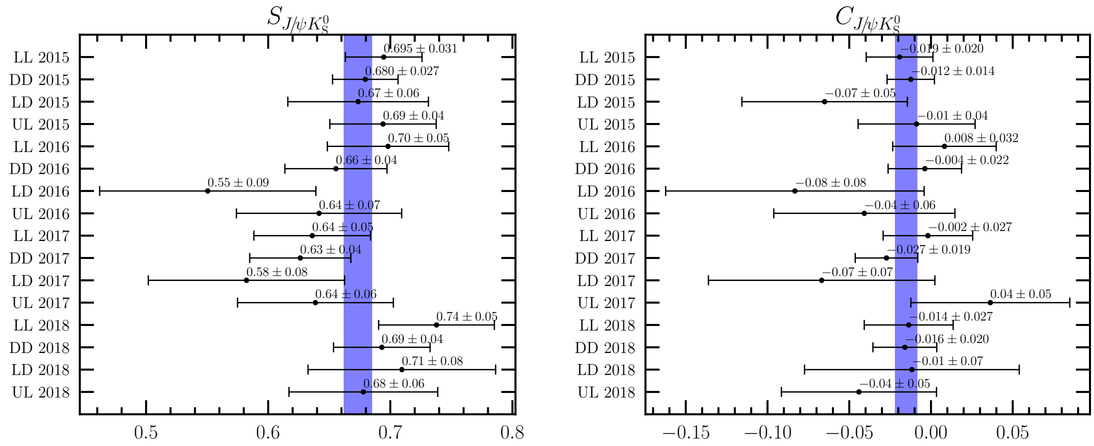

Figure 9.2: True calibration *CP* fit result of (left) S and (right) C of $B^0 \to J/\psi(\to \mu\mu)K^0_\mathrm{S}$ simulated decays. The generated value is 0.7 and 0.0, respectively. The blue bands represent the weighted mean of all measurements.

CP violation parameters on simulated samples with the nominal FT approach

The last complication step is the usage of flavour tagging calibrations determined on the simulated control channels and including all constraints. This way, the same procedure as in data is used except that generated data is used instead of recorded data. The results for the *CP* violation parameters S and C for simulated $B^0 \to J/\psi\,(\to \mu\mu)K^0_\mathrm{S}$ decays are shown in Fig. 9.3. The weighted means, represented by the blue bands, match the generated values, represented by the dashed red lines, with around 1σ, while the results are even closer for both simulated $B^0 \to \psi(2S)K^0_\mathrm{S}$ and $B^0 \to J/\psi\,(\to ee)K^0_\mathrm{S}$ decays except S in $B^0 \to \psi(2S)K^0_\mathrm{S}$ decays where the result diverges by 2σ. However, this difference is only 30 % of the statistical uncertainty of the data. Furthermore, the parameter C matches well and both *CP* violation parameters are correlated. Thus, the actual discrepancy is even less. The most plausible cause is the portability of the flavour tagging calibration, where the control channels are reconstructed with a J/ψ instead of a $\psi(2S)$. Moreover, the results are in better agreement than without using the control channels. But most importantly, the whole portability of the flavour tagging calibration is covered by a systematic uncertainty and, therefore, not investigated in even more detail. With all this, it is confirmed that the flavour tagging calibration from control channels is well enough described in the *CP* violation model.

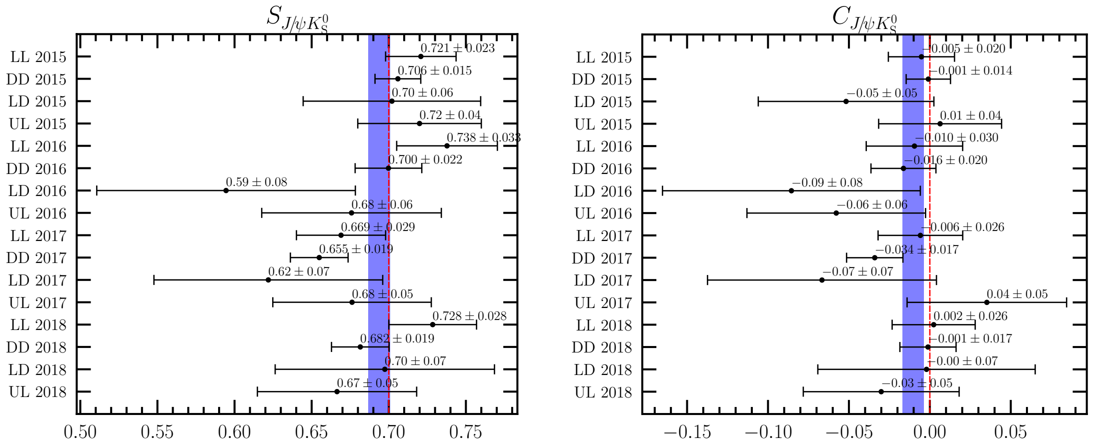

Figure 9.3: *CP* fit result of (left) S and (right) C of $B^0 \to J/\psi\,(\to \mu\mu)K^0_\mathrm{S}$ simulated decays. The generated value is 0.7 and 0.0, respectively. The blue bands represent the weighted mean of all measurements and the dashed red lines the generated values.

9.3 *CP* violation parameters on data

The values of the *CP* violation results of data were blinded until all cross-checks were performed and the whole model was settled to ensure that the strategy is not adjusted to achieve the expected results. The results after unblinding can be seen in Fig. 9.4 for all final states for all years of data taking combined separated for each track type. Within the $B^0 \to \psi(2S)K^0_S$ and $B^0 \to J/\psi(\to ee)K^0_S$ decays the *CP* violation parameters are compatible for each track type, while there are discrepancies, especially between LL and DD in $B^0 \to J/\psi(\to \mu\mu)K^0_S$ decays. This was studied in great detail and found likely to be a statistical fluctuation. More information can be found in Sec. 10.4 and Ref. [37]. The weighted combination, marked as a green band, for S is slightly bigger than 0.7, which is compatible with previous measurements by the LHCb experiment [32, 33] and with the world average [118]. The weighted combination are 0.716, 0.651 and 0.752 for $B^0 \to J/\psi(\to \mu\mu)K^0_S$, $B^0 \to \psi(2S)K^0_S$ and $B^0 \to J/\psi(\to ee)K^0_S$ decays, respectively. Within 1σ, they are all compatible with each other. The parameter C is expected to be zero, which is the case with a slight upward fluctuation in $B^0 \to J/\psi(\to ee)K^0_S$ and downward fluctuation for $B^0 \to \psi(2S)K^0_S$ decays. It can also be seen that the $J/\psi \to \mu\mu$ decay channel has by far the most sensitivity, which is as expected due to the higher branching fraction compared to the $\psi(2S) \to \mu\mu$ channel, the superior selection of the muon compared to $J/\psi \to ee$ decays and the two additional reconstruction types of the K^0_S meson.

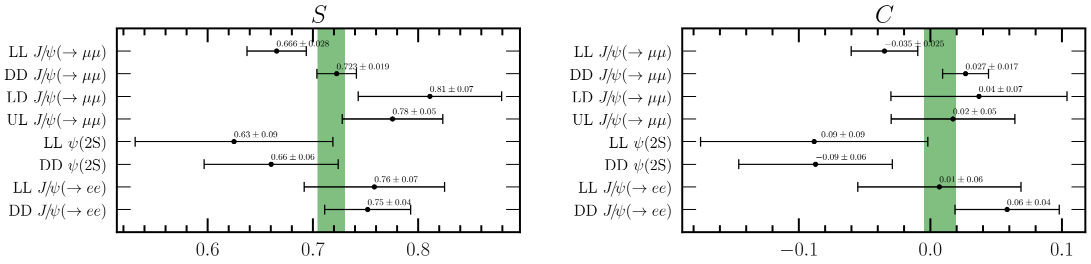

Figure 9.4: *CP* fit result of (left) S and (right) C for $B^0 \to J/\psi(\to \mu\mu)K^0_S$, $B^0 \to \psi(2S)K^0_S$ and $B^0 \to J/\psi(\to ee)K^0_S$ decays for all years of data taking combined individually for each track type. The green bands represent the weighted mean with statistical uncertainties only.

One way of representing these results is the time-dependent yield asymmetry of B^0 and $\overline{B}^0$ mesons

$$\mathcal{A}^{CP}(t) = S\sin(\Delta m_d t) - C\cos(\Delta m_d t) + \mathcal{I}, \tag{9.7}$$

where the offset $\mathcal{I}$ is caused by $\mathcal{A}_{\text{prod}}$, $\Delta\varepsilon_{\text{tag}}$ and $\Delta\omega$ and is small. The parameters S and C are the ones from above and the data points are corrected by the sWeights to use only signal candidates and by the dilution to account for the time resolution and flavour tagging. The result is shown in Fig. 9.5 for $B^0 \to J/\psi(\to \mu\mu)K^0_S$ decays.

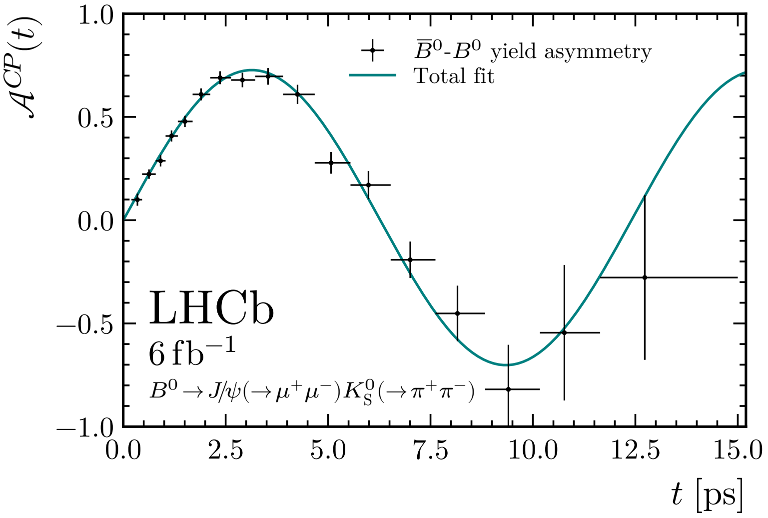

Figure 9.5: Time-dependent B^0-$\overline{B}^0$ yield asymmetry of $B^0 \to J/\psi(\to \mu\mu)K^0_S$ decays taken from Ref. [38].

The shape of the sinus term is evident with more than one period and the resulting parameters describe the data points accurately. The curve strikes almost the origin because the offset $\mathcal{I}$ is small and the parameter C is compatible with zero. Both asymmetry yields from the other decays look similar, only with higher uncertainties.

Effect of kaon regeneration and mixing

The signal decay $B^0 \to \psi K^0_S(\to \pi^+\pi^-)$ contains a K^0_S meson. However, due to the CP violation in the neutral kaon sector, it is also possible for a K^0_L meson to decay into two pions. This affects the CP violation parameters and needs to be considered. Moreover, the K^0_S and K^0_L mesons can mix and interfere differently with the detector material, leading to different CP violation parameters. With the detector material and the momenta of the kaons in the data samples it is possible to calculate the effect, the studies are detailed in Ref. [37]. The effect is smaller than -2×10^{-3} for S and around 3.5×10^{-3} for C, which is around 10% and 20% of the overall sensitivity. All results on data are corrected by these offsets.

10 Evaluation of systematic uncertainties and cross-checks

The systematic uncertainties due to model or strategy choices are essential to evaluate. A common way for this evaluation is the generation of pseudo-experiments following a PDF. The advantage is that this generation is faster and less computing expensive than a generation of data from first principles like Monte Carlo simulations, and, therefore, high precision tests can be achieved for various conditions. The generated pseudo-data is fitted with the *CP* violation PDF; see Eq. (9.1); and the difference to the generated values, the residual, is calculated. In addition, the residual divided by the fit uncertainty of the parameter, the pull, is beneficial because this is the fraction of the statistical uncertainty. This way, the pull gives insight into the importance of the specific systematic effect compared to the statistical uncertainty. All pseudo-data samples' pull and residual distributions can be described with a Gaussian function, where the deviation of the mean of the residual to zero is treated as a bias and should be included as a systematic uncertainty. The width of the Gaussian function should be close to the statistical uncertainty in the fits to data because the systematic uncertainty is neither overestimated nor underestimated in that case.

The nominal generation and assumptions of the parameters are explained in Sec. 10.1. In Sec. 10.2 all used systematic uncertainties are discussed: The method with the pseudo-data, the neglect of $\varDelta\varGamma$, the decay width difference between B^0 and $\overline{B}^0$ mesons, the decay time bias correction, the decay time bias model as well as the portability of the flavour tagging calibration and flavour tagging efficiency difference of B^0 and $\overline{B}^0$ mesons from the control channels. In Sec. 10.3 the total systematics and the combination of all three final states are given.

Throughout the analysis, many assumptions about simplifications of models which describe the data are made. Studying these assumptions and predicting the effect on the *CP* violation parameters is crucial to rule out any possible bias for the *CP* violation parameters. The assumptions comprise the time dependence of variables like the selection and reconstruction efficiency, the flavour tagging efficiency, the mistag and the invariant mass. Moreover, the correlation of the OS and SS tagger, the estimated production asymmetry, other independent measurements of the *CP* violation parameters, the value of the oscillation parameter $\varDelta m$ of the B^0 mesons and the difference between the *CP* violation parameters in the LL and DD reconstructed K^0_S mesons of $B^0 \to J/\psi(\to \mu\mu)K^0_\mathrm{S}$ decays are studied. These checks are discussed in Sec. 10.4.

10.1 Generation of pseudo-data

The generated pseudo-data contains four different components and, therefore, four different PDFs describing these components. They are the B^0 signal, the B_s^0 component, the combinatorial background and the partially reconstructed background. On data, no properties are available to distinguish all components. Therefore sWeights are used, which unfold single components from the data distributions. Furthermore, the PDFs are split into track types but combined for all years.

One step is the generation of the reconstructed invariant B^0 meson mass. The same model as in the fit to data is used, described in Ch. 6, with all parameters fixed to the results for both the signal and all background components. This way, the generated invariant B^0 meson mass is the same as on data. Afterwards, sWeights are extracted, which are included in the final *CP* violation model to access each of the four components. The decay time uncertainty and the mistag estimates for OS and SS are generated next. The distributions of both distributions cannot be easily described by a continuous function, as for the invariant B^0 meson mass. Therefore, the data is split into 60 and 100 evenly spaced bins, fine enough to be nearly continuous and coarse enough to allow for statistical fluctuations. The histograms are weighted with sWeights to account for the different decay components. The signal sWeights are used for the B^0 and B_s^0 components as well as the partially reconstructed background because they all originate from real B^0 meson decays. In contrast, the background sWeights are used for the combinatorial background. At last, the decay time and the tagging decisions for OS and SS are generated. They are generated using the same *CP* violation model as the fit to data, including the newly generated decay time uncertainty and mistag values. The values of external parameters in the PDF are listed in Table 10.1. The values are roughly the ones from previous measurements or a fit to data.

The pseudo-data is generated and fitted for each final state separately to get a systematic uncertainty for each final state.

Table 10.1: External parameters for the *CP* violation PDF in the generation for the B^0 and B_s^0 component as well as the combinatorial and partially reconstructed background.

Parameter	$B^0 \to \psi K^0_\mathrm{S}$	$B_s^0 \to \psi K^0_\mathrm{S}$	Part. reco. bkg.	Comb. bkg.
τ / ps	1.52	1.509	1.52	0.8
$\Delta\Gamma$ / ps	0	0.088	0	0
Δm / ps^{-1}	0.5065	17.757	0.5065	0.5065
S	0.7	-0.1	0.7	0
C	0	-0.3	0	0
$\mathcal{A}_{\Delta\Gamma}$	0	0.5	0	0

10.2 Systematic uncertainty estimation

In the following, all relevant sources of systematic uncertainties and how they are computed are described. This includes:

- The validation of the approach to generate pseudo-data and the usage of the *CP* violation PDF
- The fact that the parameter $\Delta\Gamma$ is neglected in the *CP* violation PDF
- The decay time bias correction
- The parameters of the decay time bias model
- The portability of the flavour tagging calibration function parameters from the control channels
- The portability of the flavour tagging efficiency asymmetry between B^0 and $\overline{B}^0$ mesons from the control channels

The systematic uncertainties due to the production asymmetry and the flavour tagging efficiency asymmetry are incorporated in a Gaussian constraint of the production asymmetry in the *CP* violation model; see Sec. 9.1. Thus, they are already contained in the statistical uncertainty. In the same way, the uncertainty of the flavour tagging calibration function parameters due to the limited statistics of the control channels is included in the statistical uncertainty.

Validation of pseudo-data generation

The first systematic uncertainty accounts for the method to generate and fit pseudo-data samples as well as the data describing PDF. The pseudo-data is generated, described in Sec. 10.1, and a fit in the same way as the data is performed; see Ch. 9 for details. This way, it is ensured that all other systematic uncertainties are unbiased or that the bias is taken into account. There are 6000 fits performed for $B^0 \to J/\psi(\to \mu\mu)K^0_S$ and 2500 for each other final state to have a sensitivity of $1\,\%$ and $2\,\%$ of the statistical uncertainty. The pull and residual distributions for $B^0 \to \psi(2S)K^0_S$ are shown in the top and bottom in Fig. 10.1 for S on the left and C on the right. The distributions for the other final states as well as all other considered systematics look similar. The systematic uncertainty for the used approach is mainly below $1\,\%$ and always negligible. Thus, the conclusion is that evaluating systematic uncertainties with pseudo-data is valid and the fit model is accurate.

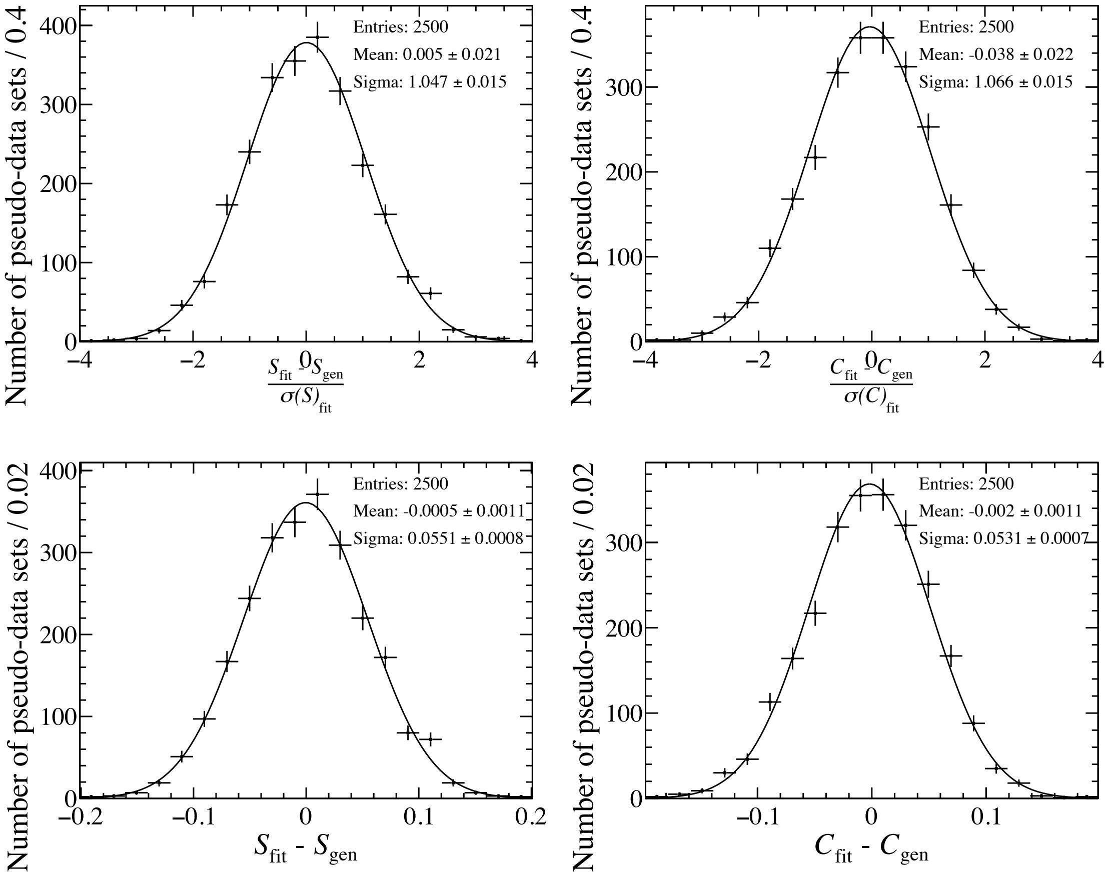

Figure 10.1: (Top) pull and (bottom) residual distribution for (left) S and (right) C for 2500 pseudo-experiments to validate the fit model and the generation of pseudo-data with a Gaussian function for each of the distributions for the $B^0 \to \psi(2S)K^0_S$ final state.

Neglect $\Delta\Gamma$ in the *CP* violation model

The parameter $\Delta\Gamma$ is small and compatible with 0 [40], and thus, set to 0 in the *CP* fit. However, any non-zero value would include the hyperbolic terms in the *CP* asymmetry; see Eq. (2.34). Therefore, a systematic uncertainty for the fact that it is neglected in the *CP* fit has to be computed. The pseudo-data is generated 1000 times with $\Delta\Gamma = \pm 0.0073\,1/\text{ps}$, corresponding to roughly 1σ up or down of the value. Besides $\Delta\Gamma$, the parameter $\mathcal{A}_{\Delta\Gamma}$ must also be set. The value $ADG = \pm\sqrt{1 - 0.7^2}$ is chosen because this satisfies the normalisation condition $S^2 + C^2 + {\mathcal{A}_{\Delta\Gamma}}^2 = 1$. Out of the four different options with the different signs of both parameters, only two are necessary, once with different signs and once with the same ones. Two options for the signs are enough because the two terms $\mathcal{A}_{\Delta\Gamma}\sinh(\Delta\Gamma t)$ and $\cosh(\Delta\Gamma t)$ in the *CP* violation PDF depend linear and quadratically of $\Delta\Gamma$, respectively. So only the linear term is relevant and the sign of this term can either be negative or positive. Without loss of generality, the parameter $\mathcal{A}_{\Delta\Gamma}$ is chosen to be always negative, while $\mathit{\Delta\Gamma}$ changes the sign for the two options. The nominal approach with $\mathit{\Delta\Gamma} = 0$ is selected in the fit to the generated pseudo-data. The pull and residual change the sign for both options, which is expected. From the two resulting values the bigger one is chosen as the systematic uncertainty to be more conservative. The systematic uncertainty is one of the systematic uncertainties with the highest impact on the overall systematic uncertainty. It is between 2 % and 11 % of the statistical uncertainty for C and between 3 % and 29 % for S. This means that the total uncertainty of the CP violation parameters is still dominated by the statistical uncertainty.

Decay time bias correction

At first, a consistency check is performed to study the necessity of a decay time bias correction. This bias is estimated and explained in Sec. 7.3. It is implemented as a shift in the mean of the resolution for each candidate of pseudo-data for $B^0 \to J/\psi(\to \mu\mu)K^0_\mathrm{S}$ decays. In the CP fit the decay time is not corrected. After evaluating 1100 pseudo-data samples, a significant bias in C is observed. Thus, a correction is mandatory and a systematic uncertainty of any remaining decay time bias after the correction is added.

The pseudo-data to study the systematic uncertainty of the decay time bias correction is generated with a negative shift in the mean of the resolution, while the decay time bias correction is included in the CP violation model. Thus, the bias is included in the generation and corrected in the model with the same magnitude and no significant difference is expected. After 2000 pseudo-data sets in $B^0 \to J/\psi(\to \mu\mu)K^0_\mathrm{S}$ and 2048 in $B^0 \to J/\psi(\to ee)K^0_\mathrm{S}$ and $B^0 \to \psi(2S)K^0_\mathrm{S}$ the systematic uncertainty in S is between 1 % and 6 % of the statistical uncertainty. The effect in C is even smaller between 2 % and 5 %. Thus, the decay time bias correction works well and the systematic uncertainty is negligible compared to the statistical uncertainty.

Decay time bias model

The estimated parameters for the decay time bias correction have an uncertainty. In the CP violation model, the uncertainty of such external parameters is accounted for with constraints by a Gaussian function. This is not possible due to technical reasons. However, the parameters can be randomly chosen from a Gaussian function with the nominal value as the mean and the uncertainty of the parameters as sigma. With these values the mean of the resolution is negatively shifted in the generation and the decay time is corrected in the CP violation model with the nominal values of the calibration function. There are 2000 pseudo-data sets generated and the systematic uncertainty in S is between 3 % and 4 % of the statistical uncertainty. In the parameter C the systematic is between 2 % and 18 %. As expected, the impact on C is higher because a decay time bias affects the shorter decay times more and C

is more sensitive at shorter decay times. However, the uncertainty is small enough that improving the decay time bias model is unnecessary.

Flavour tagging portability

The flavour tagging calibration is calculated on the control channels $B^0 \to J/\psi K^*$ and $B^\pm \to J/\psi K^\pm$, see Ch. 8 for more details. Because the mistag distributions differ between the control and signal channels, a systematic uncertainty for the portability is mandatory. For the portability, the difference between a calibration calculated on the control channels and the signal channel is estimated. However, it is impossible to determine a calibration on signal data because the signal decays are not self-tagging. Thus, simulated samples are used. First, the calibration is computed on simulated signal decays using the true IDs for the true mistag rate. Then, the calibration is calculated on simulated data of both control channels using the true IDs for the true mistag rate similarly. The GBweights to account for kinematical and topological differences are taken into account. In the end, three different sets of calibration parameters for OS and SS (simulated signal decays, simulated $B^\pm \to J/\psi K^\pm$ decays and simulated $B^0 \to J/\psi K^*$ decays) are estimated. With these calibration parameters the measured mistag ω is calculated in bins of the predicted mistag η. The differences can be seen in Fig. 10.2. The calibrated mistag ω differences are roughly linear in the predicted mistag η but also tiny.

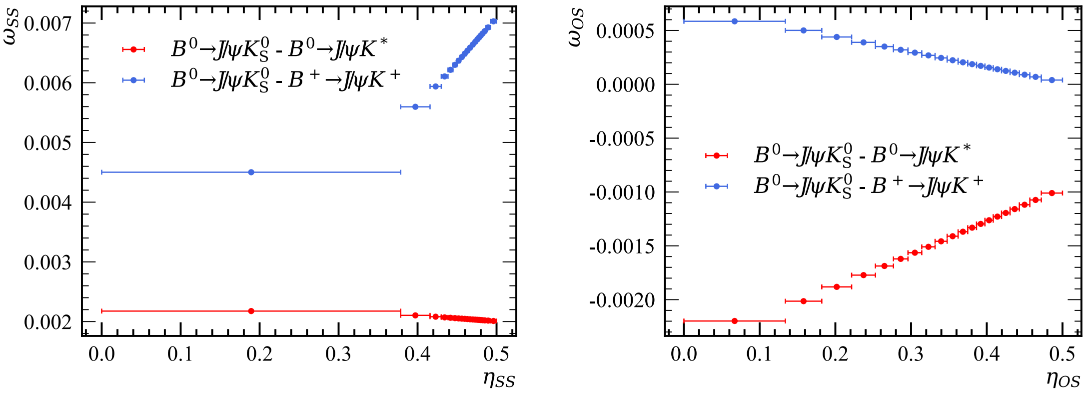

Figure 10.2: Difference of the calibrated mistag ω in bins of the predicted mistag η for (left) SS and (right) OS for $B^0 \to J/\psi(\to \mu\mu)K^0_S$ decays with calibrations from simulated $B^0 \to J/\psi(\to \mu\mu)K^0_S$ and $B^\pm \to J/\psi K^\pm$ and $B^0 \to J/\psi K^*$ decays.

For the systematic uncertainty, 400 (100) pseudo-data samples are generated in the nominal way for $B^0 \to J/\psi(\to \mu\mu)K^0_S$ ($B^0 \to J/\psi(\to ee)K^0_S$ and $B^0 \to \psi(2S)K^0_S$) to achieve a sensitivity below 1 % of the statistical uncertainty. Furthermore, another predicted mistag η branch is added. This η distribution is changed such that the calibrated mistag ω using the calibration calculated from the simulated signal decays and the calibrated mistag ω using the calibration from the control channels have the shown differences in Fig. 10.2.

Two *CP* fits are performed for each toy sample, once with the nominal mistag and once with the corrected mistag. The accounted systematic is the mean of the differences in S and C. The effect on C is at most 1.1 % of the statistical sensitivity, but S is more significant with around 30 % in both muon channels and 6 % in the electron channel. This is one of the most dominant systematics. The explicit values are given in Table 10.2.

Table 10.2: Absolute and relative systematic uncertainties for each final state's flavour tagging calibration portability.

	rel. $\sigma(S)$ [%]	abs. $\sigma(S)$	rel. $\sigma(C)$ [%]	abs. $\sigma(C)$
$B^0 \to J/\psi(\to \mu\mu)K^0_S$	−33.5	−0.004 97	0.5	0.000 07
$B^0 \to \psi(2S)K^0_S$	−31.0	−0.016 47	0.18	0.000 09
$B^0 \to J/\psi(\to ee)K^0_S$	−5.8	−0.0021	1.1	0.000 38

Flavour Tagging efficiency asymmetry portability

The flavour tagging efficiencies of B^0 and $\overline{B}^0$ mesons differ slightly, resulting in an asymmetry $\Delta\epsilon$. However, the value cannot be estimated in signal data and is, therefore, taken from the control channels, described in Sec. 9.1. The asymmetry is included in the *CP* violation model as a fixed value for the OS and SS tagger. This is justified because adding its uncertainty to the Gaussian constraint of the production asymmetry does not change the sensitivity of the *CP* violation parameters. Nevertheless, a systematic uncertainty is assigned to address the portability from the control channels.

For the systematic uncertainty, the asymmetry is calculated for the OS and SS tagger separately in the control and signal channels on simulated data, where the true flavour of the B^0 mesons is known. The nominal *CP* fit on data $\Delta\epsilon$ is varied by these differences up and down separately for OS and SS, resulting in four different fits. The higher differences to the nominal result in OS and SS are summed in quadrature to yield the total assigned systematic uncertainty. This results in an effect for C between 6 % and 11 % for the different signal channels and between 5 % and 9 % for S. This shows that the systematic is relevant, but the final result is still limited by the statistical uncertainty.

More details to calculate the flavour tagging efficiency asymmetry and its systematic uncertainty are given in Ref. [37].

10.3 Summary of systematic uncertainties

All systematic uncertainties for all final states are listed in Tables 10.3 to 10.5. The systematic uncertainties for the combination of all decays are shown in Table 10.6. The combination is calculated as the average of the single decays. The arithmetic average is used for the correlated uncertainty of the validation of the pseudo-data generation and the *CP* fit. In contrast, for all other systematic uncertainties the weighted average is used with the weight $w = 1/s^2$ and the sensitivity s. As in the single final states, the larger uncertainty from the two options for the $\Delta\Gamma$ uncertainty is chosen.

Table 10.3: Summary of the systematic uncertainties in % of the statistical uncertainty and in absolute terms. The values are evaluated for $B^0 \to J/\psi(\to \mu\mu)K^0_S$ decays. The larger of the two deviations for $\Delta\Gamma_d$ is chosen for the total systematic uncertainty.

$B^0 \to J/\psi(\to \mu\mu)K^0_S$	rel. $\sigma(S)$ [%]	abs. $\sigma(S)$	rel. $\sigma(C)$ [%]	abs. $\sigma(C)$
Fit validation	−1.8	−0.0004	0.1	<0.0001
Neglecting $\Delta\Gamma_d$ same sign	−28.5	−0.0053	−11.1	−0.0017
Neglecting $\Delta\Gamma_d$ opposite sign	27.6	0.0051	7.3	0.0011
Decay time bias correction	−3.9	−0.0007	−5.0	−0.0008
Decay time bias correction model	2.6	0.0004	−2.0	−0.0003
Flavour tagging portability	−33.3	−0.0050	0.5	0.0001
Flavour tagging $\Delta\epsilon$ portability	8.7	0.0013	10.7	0.0016
Total	45.0	0.0074	16.0	0.0025

Table 10.4: Summary of the systematic uncertainties in % of the statistical uncertainty and in absolute terms. The values are evaluated for $B^0 \to J/\psi(\to ee)K^0_S$ decays. The larger of the two deviations for $\Delta\Gamma_d$ is chosen for the total systematic uncertainty.

$B^0 \to J/\psi(\to ee)K^0_S$	rel. $\sigma(S)$ [%]	abs. $\sigma(S)$	rel. $\sigma(C)$ [%]	abs. $\sigma(C)$
Fit validation	−0.5	−0.0003	0.0	0.0002
Neglecting $\Delta\Gamma_d$ same sign	−15.4	−0.0058	−5.1	−0.0030
Neglecting $\Delta\Gamma_d$ opposite sign	21.6	0.0077	11.1	0.0040
Decay time bias correction	−5.7	−0.0015	−4.1	−0.0012
Decay time bias correction model	2.9	0.0013	−17.9	−0.0062
Flavour tagging portability	−5.8	−0.0021	1.1	0.0004
Flavour tagging $\Delta\epsilon$ portability	4.7	0.0017	6.0	0.0020
Total	24.0	0.0084	22.0	0.0077

Table 10.5: Summary of the systematic uncertainties in % of the statistical uncertainty and in absolute terms. The values are evaluated for $B^0 \to \psi(2S)K^0_S$ decays. The larger of the two deviations for $\Delta\Gamma_d$ is chosen for the total systematic uncertainty.

$B^0 \to \psi(2S)K^0_S$	rel. $\sigma(S)$ [%]	abs. $\sigma(S)$	rel. $\sigma(C)$ [%]	abs. $\sigma(C)$
Fit validation	−0.5	−0.0005	−3.8	−0.0020
Neglecting $\Delta\Gamma_d$ same sign	−3.4	−0.0015	5.6	0.0014
Neglecting $\Delta\Gamma_d$ opposite sign	13.0	0.0059	2.4	0.0011
Decay time bias correction	1.2	0.0001	1.7	0.0008
Decay time bias correction model	4.1	0.0025	−8.9	−0.0036
Flavour tagging portability	−31.2	−0.0165	0.2	0.0001
Flavour tagging $\Delta\epsilon$ portability	5.5	0.0029	6.2	0.0030
Total	34.0	0.0179	13.0	0.0053

Table 10.6: Summary of the systematic uncertainties in % of the statistical uncertainty and in absolute numbers. The values are computed from the single final state numbers with the arithmetic average in the fit validation and the weighted average in the other uncertainties with weight $w = 1/s^2$ with the sensitivity s. The larger of the two deviations for $\Delta\Gamma_d$ is chosen for the total systematic uncertainty.

	rel. $\sigma(S)$ [%]	abs. $\sigma(S)$	rel. $\sigma(C)$ [%]	abs. $\sigma(C)$
Fit validation	−2.9	−0.0004	−4.9	−0.0006
Neglecting $\Delta\Gamma_d$ same sign	−38.4	−0.0051	−13.7	−0.0017
Neglecting $\Delta\Gamma_d$ opposite sign	41.2	0.0055	12.1	0.0015
Decay time bias correction	−5.6	−0.0007	−6.1	−0.0007
Decay time bias correction model	4.9	0.0007	−10.6	−0.0013
Flavour tagging portability	−39.9	−0.0053	0.9	0.0001
Flavour tagging $\Delta\epsilon$ portability	10.3	0.0014	14.2	0.0017
Total	58.9	0.0078	23.7	0.0029

10.4 Validation of approach

Many cross-checks are performed to validate the assumptions and simplifications included in the *CP* violation model and estimate their impact on the *CP* violation parameters. This includes:

- The time dependence of the selection and reconstruction efficiency
- The time dependence of the flavour tagging efficiency
- The time dependence of the mistag
- The time dependence of the reconstructed invariant B^0 meson mass
- The correlation between the OS and SS tagger

- The value of the production asymmetry
- The difference between the *CP* violation parameters in the LL and DD reconstructed K^0_S mesons of $B^0 \to J/\psi(\to \mu\mu)K^0_\mathrm{S}$ decays
- Time-integrated measurements of the *CP* violation parameters
- B^0 and $\overline{B}^0$ independent measurements of the *CP* violation parameters
- The evaluation of the oscillation frequency Δm

In the following, they are discussed in more detail.

Time-dependent selection and reconstruction efficiency

The time-dependent selection and reconstruction efficiency, also called acceptance, is explained in detail in Sec. 7.1. An inaccurate modelled acceptance would directly affect the oscillation of the B^0 mesons because it affects the number of selected candidates and, thus, the shape of the decay time. Moreover, it would influence the *CP* violation parameters S and C. That is why a cross-check for the acceptance is required. The number of knots of the cubic spline is increased to 16 to improve the precision of the function to rule out that the acceptance function cannot accurately describe the time-dependent selection and reconstruction efficiency. The positions of the knots are set such that the distance is increasing quadratically like $\mathrm{p}_i = (\frac{i}{15})^2 \cdot (\mathrm{p}_\mathrm{max} - \mathrm{p}_\mathrm{min}) + \mathrm{p}_\mathrm{min}$ with $i \in [0, 15]$, where $\mathrm{p}_\mathrm{min} = 0.2\,\mathrm{ps}$ and $\mathrm{p}_\mathrm{max} = 15\,\mathrm{ps}$ are the minimum and maximum of the decay time range. The difference between the resulting *CP* parameters and the nominal ones is negligible. Thus, no change in the acceptance function is necessary.

Time-dependent tagging efficiency

The tagging efficiency is time-dependent but treated as constant in the *CP* violation model. Therefore, 100 pseudo-data samples of $B^0 \to J/\psi(\to \mu\mu)K^0_\mathrm{S}$ decays are generated similarly to the systematic uncertainties to analyse this effect; see Sec. 10.1 for more details. After the generation some candidates are set to untagged. The candidates are randomly selected but chosen such that the shape of the time dependence of the tagging efficiency is the same as on data. The effect of the time dependence of the tagging efficiency can be seen in Fig. 10.3 for one pseudo-data sample. The time dependence of the OS tagger is small except for the first two bins, while the SS tagger has a significant time dependence. This is expected because the OS tagger is more independent of the signal kinematics than the SS tagger. To validate the effect of the time dependence, two *CP* fits were performed. In one fit, the nominal tagging decisions are used, where no time dependence is included in the pseudo-data and in the other, the adjusted tagging decisions are used. The tagging efficiency is reduced by 4.79 % in SS and 2.06 % in OS to account for the reduced overall tagging efficiency. Untagged candidates are included in the *CP* violation model to save computing resources because this cross-check was performed before the nominal approach was changed to use only tagged candidates. The mean of the differences between both *CP* fit results are shown in Table 10.7. The effect on the *CP* violation parameters is negligible and a constant tagging efficiency does not bias the result.

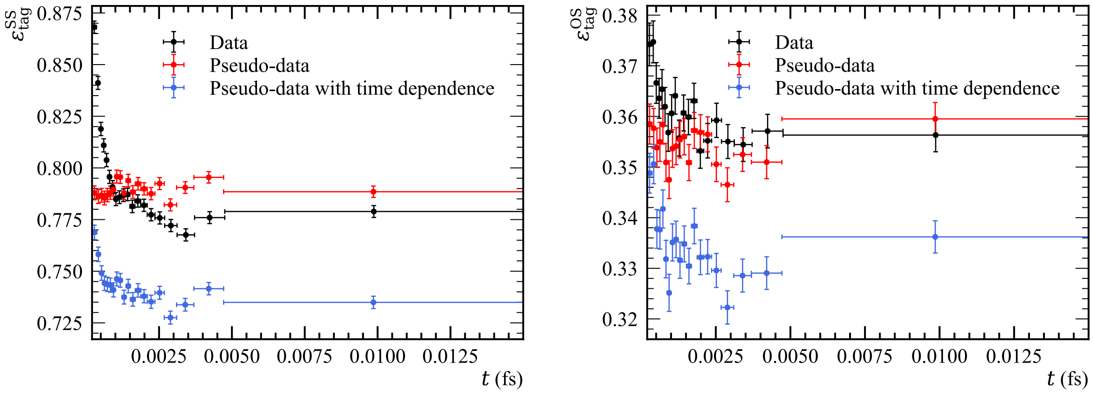

Figure 10.3: Tagging efficiency in bins of the decay time for the (left) SS tagger and (right) OS tagger. In the pseudo-data samples, the tagging decision is set to untagged randomly for some events to match the data distribution.

Table 10.7: Mean of the differences of pseudo-data with fixed tagging efficiency and changed tagging efficiency to match the time dependence for 100 pseudo-data samples for S and C for $B^0 \to J/\psi(\to \mu\mu)K^0_S$ decays.

Cross check	Mean of the differences
Tagging eff. change C	0.0004 ± 0.0003
Tagging eff. change S	-0.0001 ± 0.0004

Time-dependent mistag

Besides the tagging efficiency, the uncalibrated mistag is time-dependent, too. However, this dependence is not included in the *CP* violation model and the mistag is treated as constant in the generation of the pseudo-data. The time dependence is not significant in OS but measurable in SS, which can be seen in Fig. 10.4, where the mean of the mistag of the tagged candidates is shown in bins of the decay time for sweighted data of $B^0 \to J/\psi(\to \mu\mu)K^0_S$ decays. The dependence is mainly present in the first three bins of the decay time. Therefore, the candidates of the pseudo-data in these bins are set to untagged, beginning with the candidates

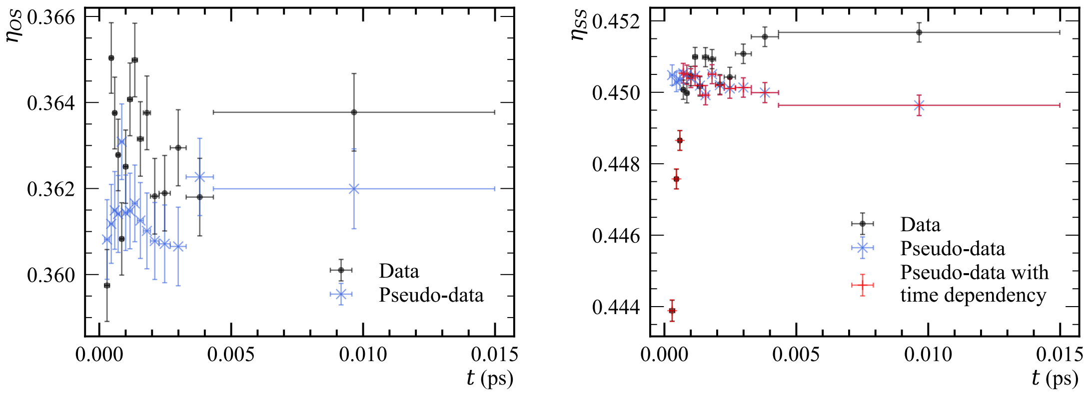

Figure 10.4: Mistag in bins of decay time for tagged candidates of $B^0 \to J/\psi(\to \mu\mu)K^0_S$ of the (left) OS and (right) SS tagger combination for sweighted data, sweighted pseudo-data and sweighted pseudo-data with calibrated mistag in the first three bins. The mistag is adjusted by setting events to untagged with high mistag.

with the highest mistag until the newly calculated mistag matches the mistag in data. This way, a new mistag distribution is created, where the time dependence is included. The mean of the differences of the *CP* violation parameter with 100 pseudo-data for both mistag distributions is

$$\Delta \mathrm{S} = 0.000\,25 \pm 0.000\,01, \tag{10.1}$$

$$\Delta \mathrm{C} = 0.000\,23 \pm 0.000\,02. \tag{10.2}$$

The uncertainty of the parameters x is given as the uncertainty of the mean value as

$$\sigma^2(x) = \frac{\sum_i (x_i - \overline{x})^2}{N(N-1)} \tag{10.3}$$

with the mean $\overline{x}$ and the number of pseudo-data candidates N. The difference between both options is small for S and C and the dependence does not have to be included in the *CP* violation model.

Time dependence of the reconstructed invariant B^0 meson mass

The sWeights are computed by describing the invariant mass of the B^0 meson to project out the signal from the background. In the *CP* violation model they are applied to the decay time of the B^0 meson. This is only valid if both variables are uncorrelated. Thus, it is necessary to study this correlation. The cross-check is performed on simulated $B^0 \to J/\psi(\to \mu\mu)K^0_S$ decays. The difference between reconstructed and true decay time and between reconstructed B^0 mass and true B^0 mass is calculated and can be seen for the LL and DD categories in Fig. 10.5.

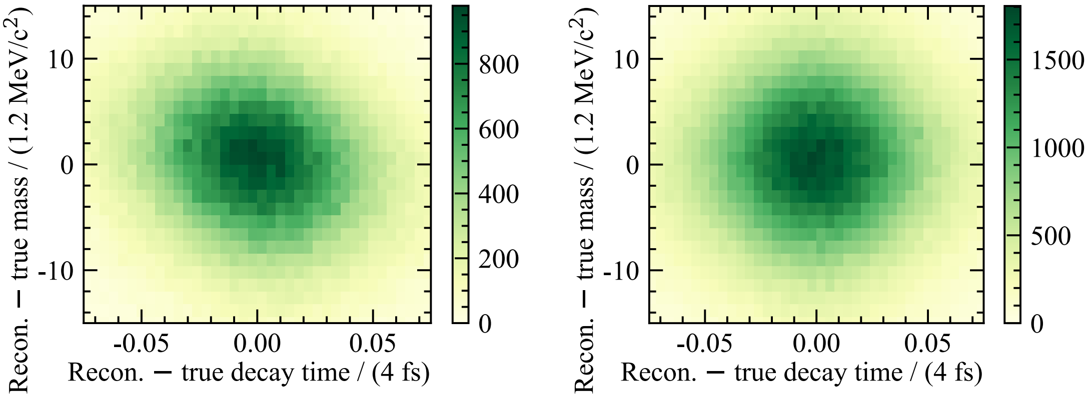

Figure 10.5: 2D histogram of the difference between reconstructed and true decay time against the difference of reconstructed and true mass for $B^0 \to J/\psi(\to \mu\mu)K^0_S$ for (left) LL and (right) DD.

A small correlation for LL reconstructed candidates is visible. Therefore, the difference between reconstructed and true decay time is calculated in bins of the mass difference. To quantify the effect of the correlation 250 pseudo-data samples of $B^0 \to J/\psi(\to \mu\mu)K^0_S$ decays are generated, where the simulation is used as a target. The decay time of these pseudo-data samples is constant in the mass but can be changed to duplicate the correlation in data. The resulting distributions are shown in Fig. 10.6 for one pseudo-data sample for LL and DD. The variance of the data points is the uncertainty of the mean value. It is calculated as

$$\frac{\sum_i (x_i - \overline{x})^2}{N(N-1)} \tag{10.4}$$

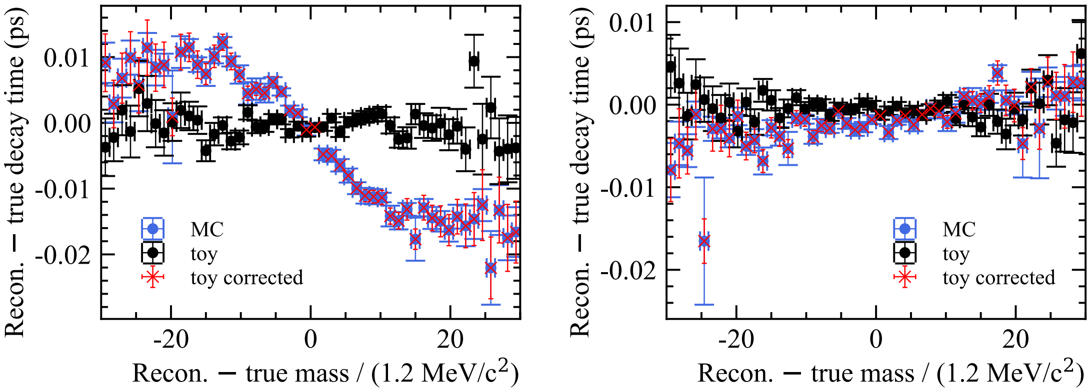

Figure 10.6: Decay time difference of reconstructed and true decay time in bins of the difference of reconstructed and true mass for $B^0 \to J/\psi(\to \mu\mu)K^0_S$ for (left) LL and (right) DD.

with the number of events N in each bin, the mean time resolution of each bin $\overline{x}$ and the time difference x_i for each candidate i in each bin. In the end, the *CP* violation model is fitted once with the raw generated decay time and once with the adjusted decay time. The mean of the difference in S and C is negligible and is listed in Table 10.8.

Due to the tiny effect and the fact that this is already the final state with the highest sensitivity, the cross-check for both other final states is omitted.

Table 10.8: The difference in S and C from a *CP* fit between the nominal approach and including the corrected decay time to study the impact of mass and decay time correlation.

Cross-check	Mean of the differences
Time mass correlation change C	$(-4.85 \pm 0.16) \times 10^{-4}$
Time mass correlation change S	$(0.03 \pm 0.10) \times 10^{-4}$

Correlation between OS and SS tagger

The OS and SS tagger combinations are assumed to be uncorrelated in the *CP* violation model. To validate this assumption the OS and SS taggers are combined in one single tagger in the $B^0 \to J/\psi(\to \ell\ell)K^*(\to K^\pm\pi^\mp)$ control channels with $\ell = \mu,\ e$. The kinematic variables are weighted to match the signal distributions. The correlation of the tagging decisions is up to 1.17 %, which is negligible. The dilution-weighted correlation of the mistag is between 1.13 to 2.1 %.

The independence is visualised for the mistag as well. On the left side of Fig. 10.7 the mistag distributions of the OS and SS tagger are shown for all final states combined, where no significant correlation can be seen. In the middle, the mistag is presented for all candidates tagged by the OS tagger independent of the SS tagger, only tagged by the OS tagger and tagged by both taggers. The same is done on the right, where OS and SS are swapped. The distributions are similar, indicating uncorrelated mistags of both taggers.

Production asymmetry

The *CP* violation parameters depend moderately on the production asymmetry $\mathcal{A}_{\text{prod}}$. As explained in Sec. 9.1, the value is constrained by a Gaussian function in the *CP* fit and extracted from a fit to $B^0 \to J/\psi K^*$ decays. Thus, its uncertainty is included in the statistical uncertainty. However, it is still beneficial to evaluate whether the mean of $\mathcal{A}_{\text{prod}}$ is sensible. No analysis is published for a measurement of $\mathcal{A}_{\text{prod}}$ at the LHCb experiment at a centre-of-mass energy of $\sqrt{s} = 13\,\text{TeV}$. It only exists one paper with data collected in 2011 and 2012 [119] at a centre-of-mass energy of 7 and 8 TeV. The measured value depends on the transverse momentum and the pseudorapidity of the B^0 meson. Using the kinematic from the selected

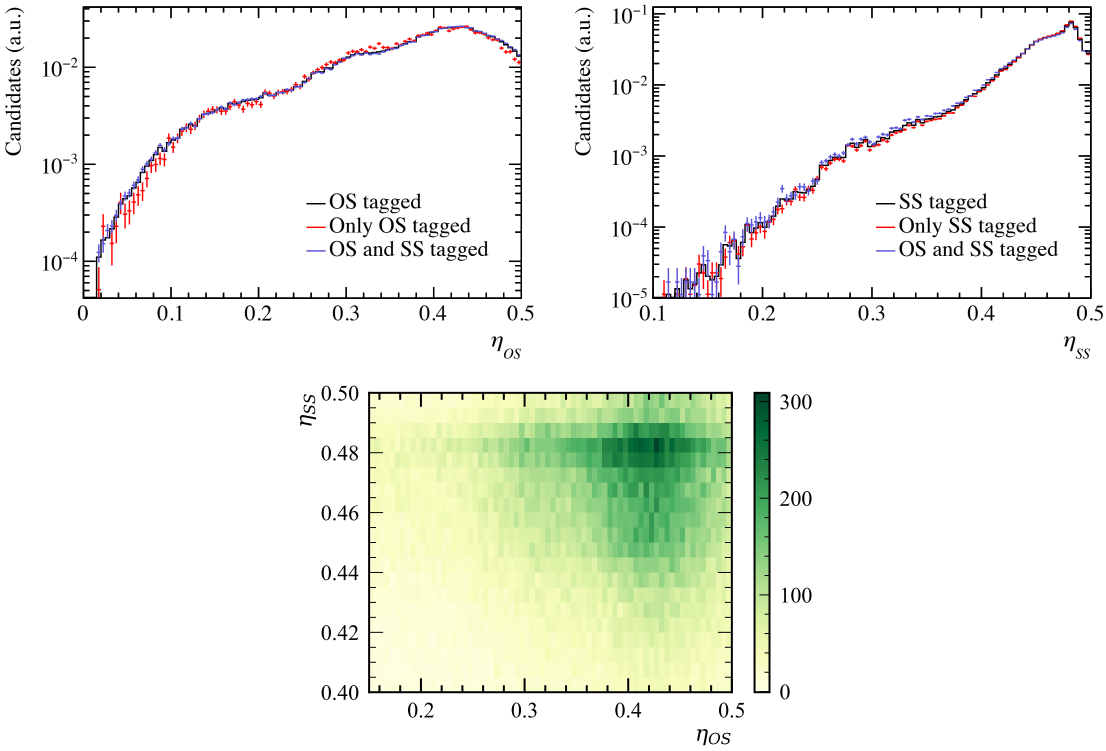

Figure 10.7: (Left) 2D histogram of the OS and SS mistag for all signal candidates combined when both taggers have a decision. (Middle) OS and (right) SS mistag distributions for all signal candidates combined, where (black) the single tagger, (red) only the single tagger and (blue) both taggers have a decision.

$B^0 \to J/\psi(\to \mu\mu)K^0_S$ decays, the scaled production value is $(-1.2 \pm 0.6)\,\%$. This is around 1.5σ from the fit value. Therefore, 2000 (1000) pseudo-data samples are generated with this alternative production asymmetry and constrained to the nominal value in the *CP* fit for the $J/\psi \to \mu\mu$ ($J/\psi \to ee$ and $\psi(2S) \to \mu\mu$) channel. The effect for the parameter C is between $9\,\%$ and $29\,\%$ of the statistical uncertainty, while it is between $1\,\%$ and $17\,\%$ for S. This is significant but similar in size to the Gaussian constraint applied to the production asymmetry in the *CP* violation model. Therefore, this effect is already considered and no additional change must be done.

Differences between *CP* violation parameters in LL and DD in $B^0 \to J/\psi(\to \mu\mu)K^0_S$

The *CP* violation parameters S and C differ between the two samples of LL and DD reconstructed K^0_S mesons in $B^0 \to J/\psi(\to \mu\mu)K^0_S$ decays. The difference has a significance of 2.17σ for a two-sided test statistic with two degrees of freedom.

In total, 23 different types of checks were performed, including fits in bins of variables, fits with different selection requirements, using the SS and OS flavour tagging algorithms separately, no kinematic reweighting for the flavour tagging control channels, individual flavour tagging calibration for each track type, different lower and upper decay time ranges and with a calculated decay time neglecting information from the kaon vertex. No physical indications from these checks were found and the difference is assumed to be a statistical fluctuation. More information about these checks can be found in Ref. [37].

Time-integrated measurements

All previously mentioned measurements of the *CP* violation parameters are time-dependent. An orthogonal approach is to measure the parameters time-integrated. This is done for only tagged candidates of simulated and pseudo-data samples for $B^0 \to J/\psi(\to \mu\mu)K^0_S$ decays. The *CP* asymmetry in the simplified case with $\Delta\Gamma = 0$, $t_{\min} = 0$ and without acceptance effect is expressed as

$$\mathcal{A}_{\text{int}}{}^{\text{obs}} = \frac{\int_{t_{\min}}^{\infty} \Gamma^{\text{obs}}(\overline{B}^0 \to f)\,\mathrm{d}t - \int_{t_{\min}}^{\infty} \Gamma^{\text{obs}}(B^0 \to f)\,\mathrm{d}t}{\int_{t_{\min}}^{\infty} \Gamma^{\text{obs}}(\overline{B}^0 \to f)\,\mathrm{d}t + \int_{t_{\min}}^{\infty} \Gamma^{\text{obs}}(B^0 \to f)\,\mathrm{d}t} \tag{10.5}$$

$$= (1 - \omega^{B^0} - \omega^{\overline{B}^0})\frac{\Delta m\tau S_{\text{int}} - C_{\text{int}}}{1 + (\Delta m\tau)^2}. \tag{10.6}$$

In addition, the time-integrated asymmetry $\mathcal{A}_{\text{int}}$ can be determined as the dilution-corrected number of B^0 and $\overline{B}^0$ mesons

$$\mathcal{A}_{\text{int}} = \frac{N_{B^0} - N_{\overline{B}^0}}{N'_{B^0} + N'_{\overline{B}^0}}, \tag{10.7}$$

with $N = \sum_i w_i D_i$ and $N' = \sum_i w_i D_i^2$ for B^0 and $\overline{B}^0$ candidates. No significant differences are found and more information can be found in Ref. [37].

B^0 and $\overline{B}^0$ independet measurements

In the nominal approach, the B^0 and $\overline{B}^0$ mesons are fitted simultaneously resulting in a simultaneous normalisation of the model for both mesons. This must not be correct because B^0 and $\overline{B}^0$ mesons have different distributions, especially for the flavour tagging. Two independent measurements for B^0 and $\overline{B}^0$ mesons in the $J/\psi \to \mu\mu$ channel are performed to validate this method. The details can be found in Ref. [37], but no significant differences to the nominal results are found.

Evaluation of the oscillation frequency Δm

The oscillation frequency Δm is constrained by a Gaussian function with the world average for the mean and sigma in the *CP* violation model. This is valid because the effect of Δm is around 0.5 ‰ for B^0 mesons. The advantage of the constraint is that the uncertainties on the *CP* violation parameters decrease using the input from different measurements, which are more sensitive to the value of Δm. An additional fit was performed for all data combined, where Δm was left floating and the resulting value matches the world average. Hence, no additional systematic uncertainty is necessary.

In summary, many cross-checks are performed with no significant impact on the *CP* violation parameters. Therefore, no additional changes for the *CP* violation model or any additional systematic uncertainties are necessary.

11 Results and combination of decay channels

The data for the time-dependent *CP* violation measurement presented in this thesis is recorded at the LHCb experiment between 2015 and 2018. It corresponds to an integrated luminosity of $6\,\mathrm{fb}^{-1}$ and involves the decays $B^0 \to J/\psi(\to \mu\mu)K^0_\mathrm{S}$, $B^0 \to \psi(2S)(\to \mu\mu)K^0_\mathrm{S}$ (abbreviated as $\psi(2S)K^0_\mathrm{S}$) and $B^0 \to J/\psi(\to ee)K^0_\mathrm{S}$ with $K^0_\mathrm{S} \to \pi^+\pi^-$. The resulting *CP* violation parameters with statistic and systematic uncertainties are given as

$$\begin{aligned}
S_{J/\psi(\to\mu\mu)K^0_\mathrm{S}} &= 0.716 \pm 0.015\,(\mathrm{stat.}) \pm 0.007\,(\mathrm{syst.})\,,\\
C_{J/\psi(\to\mu\mu)K^0_\mathrm{S}} &= 0.010 \pm 0.014\,(\mathrm{stat.}) \pm 0.003\,(\mathrm{syst.})\,,\\
S_{\psi(2S)K^0_\mathrm{S}} &= 0.649 \pm 0.053\,(\mathrm{stat.}) \pm 0.018\,(\mathrm{syst.})\,,\\
C_{\psi(2S)K^0_\mathrm{S}} &= -0.087 \pm 0.048\,(\mathrm{stat.}) \pm 0.005\,(\mathrm{syst.})\,,\\
S_{J/\psi(\to ee)K^0_\mathrm{S}} &= 0.754 \pm 0.037\,(\mathrm{stat.}) \pm 0.008\,(\mathrm{syst.})\,,\\
C_{J/\psi(\to ee)K^0_\mathrm{S}} &= 0.042 \pm 0.034\,(\mathrm{stat.}) \pm 0.008\,(\mathrm{syst.})\,,
\end{aligned}$$

with correlation coefficients between S and C of 0.446, 0.503 and 0.374 for the $J/\psi(\to \mu\mu)K^0_\mathrm{S}$, $\psi(2S)K^0_\mathrm{S}$ and $J/\psi(\to ee)K^0_\mathrm{S}$ decays, respectively. All three decay channels are compatible with each other within 2σ. The highest tension is between $B^0 \to \psi(2S)(\to \mu\mu)K^0_\mathrm{S}$ and $B^0 \to J/\psi(\to ee)K^0_\mathrm{S}$ decays, while the result of the $B^0 \to J/\psi(\to \mu\mu)K^0_\mathrm{S}$ decays is in between. The uncertainties for all variables are dominated by the statistical uncertainty, which will decrease with more data in the future. The world average of all previous measurements including a charmonium final state is given as $S_\text{world average} = 0.699 \pm 0.017$ and $C_\text{world average} = -0.005 \pm 0.015$ [118]. This agrees with the results within 2σ and shows that the single measurement with $B^0 \to J/\psi(\to \mu\mu)K^0_\mathrm{S}$ decays already has a higher sensitivity. Thus, this measurement supersedes the combination of all previous measurements for this type of decay.

The parameter C is a measure of the direct *CP* violation, which is not present in the SM for $B^0 \to \psi K^0_\mathrm{S}$ decays. The results reflect this, while the $B^0 \to \psi(2S)K^0_\mathrm{S}$ decays have the highest deviation with 1.7σ. If no higher-order effects like loop diagrams, which are highly suppressed in the SM, are considered, the parameter S is equal to $\sin(2\beta)$. This simplification is valid up to 1° [58–60] for the value of β, which is at the edge of the current sensitivity. The parameter S is measured around 0.71, which corresponds to $\beta = 22.6°$.

All three decay channels are combined into one data sample to increase the sensitivity even more. The decay-specific parameters, all flavour tagging parameters, the per-event resolution, the acceptance and the decay time bias correction function parameters, stay the same. The production asymmetry, the lifetime, the B^0 oscillation frequency and both CP violation parameters S and C are shared between the decay channels. This results in

$$\begin{aligned} S_{\psi K^0_S} &= 0.717 \pm 0.013\,(\text{stat.}) \pm 0.008\,(\text{syst.})\,, \\ C_{\psi K^0_S} &= 0.008 \pm 0.012\,(\text{stat.}) \pm 0.003\,(\text{syst.})\,, \end{aligned}$$

with a correlation coefficient of 0.441. An increase of the world average of all previous measurements with a charmonium in the final state combined of around 10% and 20% for S and C, respectively, is achieved [118]. This also leads to the most accurate time-dependent asymmetry yield from the LHCb experiment, which can be seen in Fig. 11.1. The yield asymmetry is dominated by $S\sin(\Delta mt)$, which results in the oscillating shape of the asymmetry with the amplitude given by the parameter S. The parameter C shifts the fit curve out of the origin. However, this shift is hardly visible because the parameter is tiny and compatible with 0. The majority of data is at short decay times, resulting in higher uncertainties at high decay times. Nonetheless, over one oscillation period is visible.

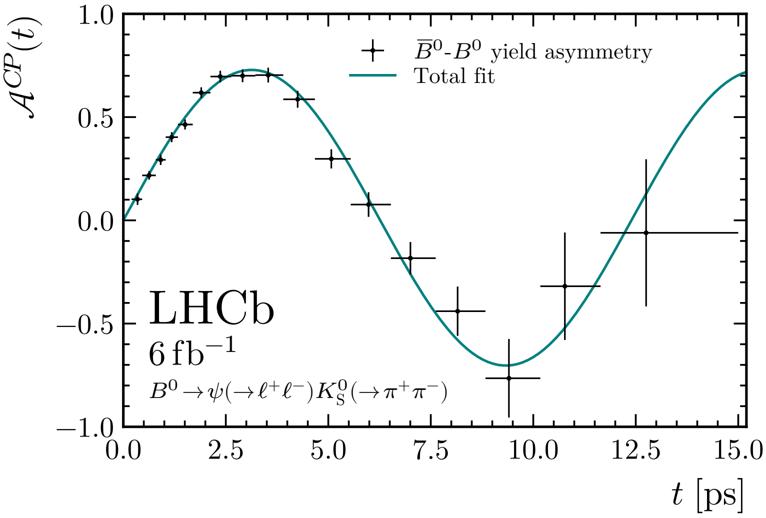

Figure 11.1: Time-dependent B^0-$\overline{B}^0$ yield asymmetry of all three decay channels combined taken from Ref. [38].

A comparison with previous measurements from the LHCb experiment with these final states can be seen in Fig. 11.2. The details of these analyses are given in Refs [32, 33]. Although the mean values change mildly, all measurements are compatible. The more efficient selection and the higher amount of recorded data increases the sensitivity significantly. Furthermore, the order of the final states with the highest sensitivity remains unchanged. A combination of these results is performed using GAMMACOMBO [120], where the results are mainly driven by the new measurements. It results in

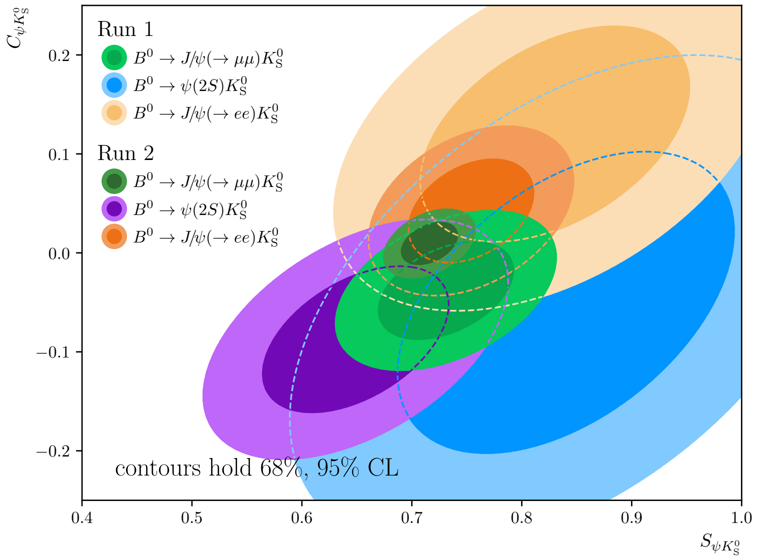

Figure 11.2: Measurement results of S and C for $B^0 \to J/\psi(\to \mu\mu)K^0_S$, $B^0 \to J/\psi(\to ee)K^0_S$ and $B^0 \to \psi(2S)(\to \mu\mu)K^0_S$ decays with the LHCb experiment from data samples collected between 2011 and 2012 (Run 1) [32, 33] and between 2015 and 2018 (Run 2) presented in this thesis.

$$\begin{aligned} S^{\text{LHCb}}_{\psi K^0_S} &= 0.724\,28 \pm 0.013\,27\,(\text{stat.}) \pm 0.0055\,(\text{syst.}), \\ C^{\text{LHCb}}_{\psi K^0_S} &= 0.004\,49 \pm 0.011\,23\,(\text{stat.}) \pm 0.0028\,(\text{syst.}). \end{aligned}$$

The systematic uncertainties from the previous measurements were rescaled if new measurements of external parameters reduced the uncertainty of these parameters. Additionally, the correlations of systematic uncertainties are considered in the combination. It can be seen that the decrease of the statistical uncertainty is insignificant and only within its rounding. This illustrates the importance and the high sensitivity of the measurement presented in this thesis.

The comparison with previous measurements from the Belle and BaBar experiment is shown in Fig. 11.3. This new result fits in perfectly and increases the compatibility between the e^-e^+ and the pp collision measurements. Moreover, it can be seen that the new result has the highest sensitivity for the *CP* violation parameters S and C. The uncertainties of both positron-electron colliders are not stretched because S and C are nearly uncorrelated in these measurements. This is the case because, in contrast to the LHCb experiment, decay time differences between two B^0 mesons are measured. On the one hand, the signal B^0 meson and, on the other hand, the B^0 meson, which is also created at the e^-e^+ collision and is used to determine the flavour of the mesons.

The combination of all these measurements leads to a preliminary new world average of

$$S_{\text{world average}} = 0.708 \pm 0.011, \tag{11.1}$$
$$C_{\text{world average}} = 0.006 \pm 0.010. \tag{11.2}$$

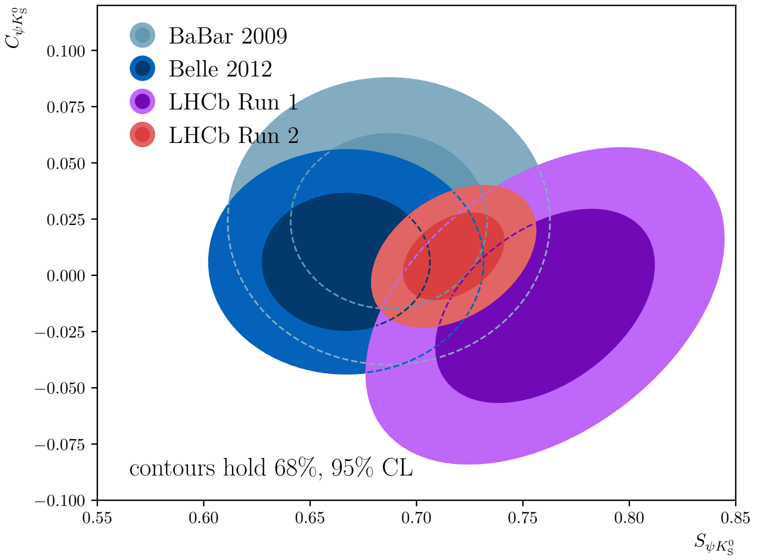

Figure 11.3: Measurement results of S and C from the Belle, BaBar and LHCb experiment.

12 Summary and outlook

The Standard Model of particle physics is the most accurate description of fundamental interactions and its predictions are confirmed in many experiments. However, there are open questions and observations which cannot be explained by the SM, *e.g.* the matter-antimatter asymmetry [23] in the universe. One of Sakharov's conditions [25] to explain this asymmetry is *CP* violation. Although *CP* violation is included in the SM, the amount of *CP* violation is insufficient to explain the matter-antimatter asymmetry completely. Therefore, it is necessary to study *CP* violation in more detail to find an aspect of the theory where physics beyond the Standard Model can be exploited. One of the most sensitive observables of *CP* violation is $\sin(2\beta)$. The cleanest and most accurate decay to determine $\sin(2\beta)$ both experimental and theoretical is $B^0 \to \psi K^0_S$ with the K^0_S meson decaying into two pions and the charmonium into two electrons or muons. The experimental advantage is the huge number of signal candidates because the decay can occur at tree level, the efficient selection and reconstruction of the particles and the large oscillation frequency with negligible detector resolution effects. Moreover, the high boost of the B^0 meson, and thus, the high decay time and flight distance, helps to distinguish signal and background candidates. In addition, the second B^0 meson created at the *pp* collision can be used for the flavour tagging of the signal B^0 meson and increase the effective tagging efficiency. The benefit for the theoretical side is the possibility to calculate the observable perturbatively, where the corrections are minor and the fact that the *CP* violation in $B^0 \to \psi K^0_S$ decays depends mainly on $\sin(2\beta)$.

One of the best-suited experiments in the world for this measurement is the LHCb experiment at CERN. The analysed data sample presented in this thesis is collected between 2015 and 2018 with *pp* collisions with a center-of-mass energy of $\sqrt{s} = 13\,\text{TeV}$ corresponding to an integrated luminosity of $6\,\text{fb}^{-1}$ and over 430 000 $B^0 \to \psi K^0_S$ candidates. The decay time dependent *CP* violation measurement in $B^0 \to J/\psi(\to \mu\mu)K^0_S$, $B^0 \to \psi(2S)(\to \mu\mu)K^0_S$ and $B^0 \to J/\psi(\to ee)K^0_S$ with $K^0_S \to \pi^+\pi^-$ results in

$$\begin{aligned}
S_{J/\psi(\to\mu\mu)K^0_S} &= 0.716 \pm 0.015\,(\text{stat.}) \pm 0.007\ \ (\text{syst.})\,,\\
C_{J/\psi(\to\mu\mu)K^0_S} &= 0.010 \pm 0.014\,(\text{stat.}) \pm 0.003\ \ (\text{syst.})\,,\\
S_{\psi(2S)K^0_S} &= 0.649 \pm 0.053\,(\text{stat.}) \pm 0.018\ \ (\text{syst.})\,,\\
C_{\psi(2S)K^0_S} &= -0.087 \pm 0.048\,(\text{stat.}) \pm 0.005\ \ (\text{syst.})\,,\\
S_{J/\psi(\to ee)K^0_S} &= 0.754 \pm 0.037\,(\text{stat.}) \pm 0.008\ \ (\text{syst.})\,,\\
C_{J/\psi(\to ee)K^0_S} &= 0.042 \pm 0.034\,(\text{stat.}) \pm 0.008\ \ (\text{syst.})\,,
\end{aligned}$$

with correlation coefficients between S and C of 0.446, 0.503 and 0.374 for the three final states, respectively. The first uncertainty corresponds to the statistical uncertainty and the second to the systematic. The parameter S is in first order the same as $\sin(2\beta)$, which is the most precise single measurements in the world and in good agreement with each other. The parameter C is compatible within all decay channels and compatible with 0, which is the expectation of the SM. In addition, the results agree with previous measurements with data collected in 2011 and 2012 by the LHCb experiment [32, 33], which can be seen in Fig. 12.1.

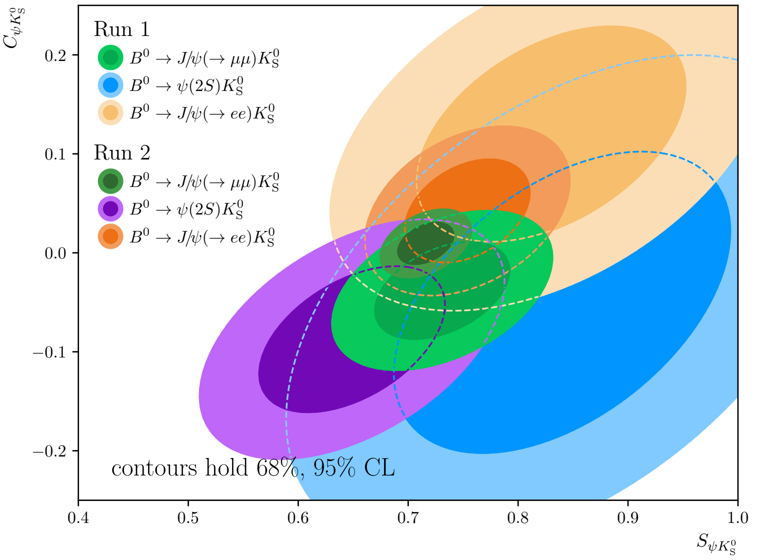

Figure 12.1: Measurement results of S and C for $B^0 \to J/\psi(\to \mu\mu)K^0_S$, $B^0 \to J/\psi(\to ee)K^0_S$ and $B^0 \to \psi(2S)(\to \mu\mu)K^0_S$ decays with the LHCb experiment from data samples collected between 2011 and 2012 (Run 1) [32, 33] and between 2015 and 2018 (Run 2) presented in this thesis.

Besides the single measurements, a combination of all three decay channels is performed as well. It results in

$$\begin{aligned} S_{\psi K^0_S} &= 0.717 \ \pm 0.013 \ \text{(stat.)} \pm 0.008 \ \text{(syst.)}\,, \\ C_{\psi K^0_S} &= 0.008 \ \pm 0.012 \ \text{(stat.)} \pm 0.003 \ \text{(syst.)}\,, \end{aligned}$$

with a correlation coefficient between S and C of 0.441. This is more precise than the world average of all previous measurements with a charmonium in the final state combined. It is an increase of around 10% and 20% for S and C, respectively [118]. From these results, the CKM angle β is calculated to

$$\beta = 22.9 \pm 0.6\,, \tag{12.1}$$

which agrees with the world average within 1σ. This is at a precision where higher-order effects are not negligible anymore [58–60]. Possible measurements to determine these higher-order effects are analyses of the decay time dependent CP violation in $B^0 \to J/\psi \pi^+\pi^-$ or $B_s^0 \to J/\psi K_S^0$ decays because penguin contributions play an important role. Therefore, the effective β_{eff} value is measured and can be used to calibrate the measurement in $B^0 \to \psi K_S^0$ decays.

A simple combination of the world average and the new measurement would lead to

$$S_{\text{world average}} = 0.708 \pm 0.011\,, \tag{12.2}$$

$$C_{\text{world average}} = 0.006 \pm 0.010\,. \tag{12.3}$$

All results presented in this thesis are limited by the statistical uncertainty, which means the results will improve with more collected data. All data from the LHCb experiment is used in the presented thesis. However, after an upgrade phase, where nearly the complete LHCb detector was renewed, the data-taking period started at the beginning of 2023 and will proceed with additional upgrade phases up to 2042. The estimated integrated luminosity is $350\,\text{fb}^{-1}$ [121], which is nearly a factor 60 in increase of the amount of data compared to today. With the same selection and effective tagging efficiency, the sensitivity would increase by more than a factor of seven, achieving permille uncertainty for the CKM angle β. Moreover, the trigger system to select the raw data is adjusted for the new data-taking period, where a software-based selection replaces the first hardware selection step. This way, the selections are more effective, resulting in even more data to analyse. With all this in mind, systematic uncertainties can be more crucial in future analyses. However, the largest systematics are due to the $\Delta\Gamma$ term and the flavour tagging portability, which improve with more accurate analyses due to more data. Furthermore, a new flavour tagging approach is in preparation, where the whole event is analysed within a deep neural network. First results indicate an significant increase in the performance in neutral B_d meson decays.

Bibliography

[1] D. J. Griffiths, *Introduction to elementary particles*, TextBook Physics, Wiley, New York, NY, 1987.

[2] M. E. Peskin and D. V. Schroeder, *An Introduction to quantum field theory*, Addison-Wesley, Reading, USA, 1995.

[3] S. L. Glashow, *Partial-symmetries of weak interactions*, Nucl. Phys. **22** (1961) 579.

[4] A. Salam and J. C. Ward, *Electromagnetic and weak interactions*, Phys. Lett. **13** (1964) 168.

[5] S. Weinberg, *A model of leptons*, Phys. Rev. Lett. **19** (1967) 1264.

[6] C. S. Wu *et al.*, *Experimental test of parity conservation in beta decay*, Phys. Rev. **105** (1957) 1413.

[7] J. H. Christenson, J. W. Cronin, V. L. Fitch, and R. Turlay, *Evidence for the* 2π *decay of the* K_2^0 *meson*, Phys. Rev. Lett. **13** (1964) 138.

[8] J. J. Aubert *et al.*, *Experimental observation of a heavy particle* J, Phys. Rev. Lett. **33** (1974) 1404.

[9] J.-E. Augustin *et al.*, *Discovery of a narrow resonance in* e^+e^- *annihilation*, Phys. Rev. Lett. **33** (1974) 1406.

[10] D0 Collaboration, S. Abachi *et al.*, *Search for high mass top quark production in* $p\bar{p}$ *collisions at* $\sqrt{s} =$ *1.8 TeV*, Phys. Rev. Lett. **74** (1995) 2422.

[11] CDF Collaboration, F. Abe *et al.*, *Observation of top quark production in* $\overline{p}p$ *collisions with the Collider Detector at Fermilab*, Phys. Rev. Lett. **74** (1995) 2626.

[12] K. Kodama *et al.*, *Observation of tau neutrino interactions*, Phys. Lett. **B504** (2001) 218.

[13] ATLAS Collaboration, G. Aad *et al.*, *Observation of a new particle in the search for the Standard Model Higgs boson with the ATLAS detector at the LHC*, Phys. Lett. **B716** (2012) 1, `arXiv:1207.7214`.

[14] CMS Collaboration, S. Chatrchyan *et al.*, *Observation of a new boson at a mass of* 125 *GeV with the CMS experiment at the LHC*, Phys. Lett. **B716** (2012) 30, `arXiv:1207.7235`.

[15] LHCb collaboration, R. Aaij *et al.*, *Analysis of neutral B-meson decays into two muons*, Phys. Rev. Lett. **128** (2022) 041801, `arXiv:2108.09284`.

[16] LHCb collaboration, R. Aaij *et al.*, *Measurement of the* $B_s^0 \to \mu^+\mu^-$ *decay properties and search for the* $B^0 \to \mu^+\mu^-$ *and* $B_s^0 \to \mu^+\mu^-\gamma$ *decays*, Phys. Rev. **D105** (2022) 012010, `arXiv:2108.09283`.

[17] Super-Kamiokande Collaboration, Y. Fukuda *et al.*, *Evidence for oscillation of atmospheric neutrinos*, Phys. Rev. Lett. **81** (1998) 1562.

[18] SNO Collaboration, Q. R. Ahmad *et al.*, *Measurement of the rate of* $\nu_e + d \to p + p + e^-$ *interactions produced by* ^8B *solar neutrinos at the Sudbury Neutrino Observatory*, Phys. Rev. Lett. **87** (2001) 071301.

[19] SNO Collaboration, Q. R. Ahmad *et al.*, *Direct evidence for neutrino flavor transformation from neutral-current interactions in the Sudbury Neutrino Observatory*, Phys. Rev. Lett. **89** (2002) 011301.

[20] Planck Collaboration, N. Aghanim *et al.*, *Planck 2018 results. VI. Cosmological parameters*, Astron. Astrophys. **641** (2020) A6, `arXiv:1807.06209`, [Erratum: Astron.Astrophys. 652, C4 (2021)].

[21] V. Trimble, *Existence and nature of dark matter in the universe*, Annual Review of Astronomy and Astrophysics **25** (1987) 425.

[22] M. S.Turner and D. Huterer, *Cosmic acceleration, dark energy, and fundamental physics*, Journal of the Physical Society of Japan **76** (2007) 111015.

[23] L. Canetti, M. Drewes, and M. Shaposhnikov, *Matter and antimatter in the universe*, New Journal of Physics **14** (2012) 095012.

[24] G. Gamow, *Expanding universe and the origin of elements*, Phys. Rev. **70** (1946) 572.

[25] A. D. Sakharov, *Violation of CP invariance, C asymmetry, and baryon asymmetry of the universe*, Soviet Physics Uspekhi **34** (1991) 392.

[26] T. S. Virdee, *Beyond the standard model of particle physics*, Philosophical Transactions of the Royal Society A: Mathematical, Physical and Engineering Sciences **374** (2016) 20150259.

[27] A. Abada *et al.*, *FCC-ee: The Lepton Collider*, The European Physical Journal Special Topics **228** (2019) 261.

[28] A. Abada *et al.*, *FCC-hh: The Hadron Collider*, The European Physical Journal Special Topics **228** (2019) 755.

[29] W. Heisenberg, *Über den anschaulichen Inhalt der quantentheoretischen Kinematik und Mechanik*, Z. Phys. **43** (1927) 172.

[30] N. Cabibbo, *Unitary symmetry and leptonic decays*, Phys. Rev. Lett. **10** (1963) 531.

[31] M. Kobayashi and T. Maskawa, *CP-violation in the renormalizable theory of weak interaction*, Prog. Theor. Phys. **49** (1973) 652.

[32] LHCb collaboration, R. Aaij *et al.*, *Measurement of CP violation in* $B^0 \to J/\psi K^0_S$ *decays*, Phys. Rev. Lett. **115** (2015) 031601, `arXiv:1503.07089`.

[33] LHCb collaboration, R. Aaij *et al.*, *Measurement of CP violation in* $B^0 \to J/\psi K^0_S$ *and* $B^0 \to \psi(2S) K^0_S$ *decays*, JHEP **11** (2017) 170, `arXiv:1709.03944`.

[34] BaBar Collaboration, B. Aubert *et al.*, *Measurement of time-dependent CP asymmetry in* $B^0 \to c\bar{c}K^{(*)0}$ *decays*, Phys. Rev. **D79** (2009) 072009, `arXiv:0902.1708`.

[35] Belle Collaboration, I. Adachi *et al.*, *Precise measurement of the CP violation parameter* $\sin 2\phi_1$ *in* $B^0 \to (c\bar{c})K^0$ *decays*, Phys. Rev. Lett. **108** (2012) 171802, `arXiv:1201.4643`.

[36] P. Mackowiak, *Measurements of beauty hadron to charmonium decays*, PhD thesis, Technische Universität Dortmund, 2021, doi: 10.17877/DE290R-22118.

[37] V. Jévtic, *Precision measurement of CP-violation parameters with the LHCb experiment*, PhD thesis, Technische Universität Dortmund, 2023, in preparation.

[38] LHCb collaboration, R. Aaij *et al.*, *Measurement of CP violation in* $B^0 \to \psi(\to \ell^+\ell^-)K^0_S(\to \pi^+\pi^-)$ *decays*, Phys. Rev. Lett. **132** (2024) 021801, `arXiv:2309.09728`.

[39] F. Meier, *Measurements of* $\sin 2\beta$ *using charmonium and open charm decays at LHCb*, PhD thesis, Technische Universität Dortmund, 2016, doi: 10.17877/DE290R-17736.

[40] Particle Data group, R. L. Workman *et al.*, *Review of particle physics*, Prog. Theor. Exp. Phys. **2022** (2022) 083C01.

[41] K. G. Wilson, *Confinement of quarks*, Phys. Rev. D **10** (1974) 2445.

[42] LHCb collaboration, R. Aaij *et al.*, *Observation of the resonant character of the* $Z(4430)^-$ *state*, Phys. Rev. Lett. **112** (2014) 222002, `arXiv:1404.1903`.

[43] LHCb collaboration, R. Aaij *et al.*, *Observation of $J/\psi p$ resonances consistent with pentaquark states in $\Lambda_b^0 \to J/\psi p K^-$ decays*, Phys. Rev. Lett. **115** (2015) 072001, `arXiv:1507.03414`.

[44] P. W. Higgs, *Broken symmetries and the masses of gauge bosons*, Phys. Rev. Lett. **13** (1964) 508.

[45] R. P. Feynman, *Space-time approach to quantum electrodynamics*, Phys. Rev. **76** (1949) 769.

[46] L. Landau, *On the conservation laws for weak interactions*, Nuclear Physics **3** (1957) 127.

[47] J. S. Schwinger, *The theory of quantized fields. 1.*, Phys. Rev. **82** (1951) 914.

[48] G. Lüders, *On the equivalence of invariance under time reversal and under particle-antiparticle conjugation for relativistic field theories*, Kong. Dan. Vid. Sel. Mat. Fys. Med. **28N5** (1954) 1.

[49] W. Pauli, *Niels Bohr and the development of physics: Essays dedicated to Niels Bohr on the occasion of his seventieth birthday*, McGraw-Hill, 1955.

[50] L. Wolfenstein, *Parametrization of the Kobayashi-Maskawa matrix*, Phys. Rev. Lett. **51** (1983) 1945.

[51] C. Jarlskog, *Commutator of the quark mass matrices in the standard electroweak model and a measure of maximal CP nonconservation*, Phys. Rev. Lett. **55** (1985) 1039, Erratum ibid. **58** (1987) 1698.

[52] C. Jarlskog, *A basis independent formulation of the connection between quark mass matrices, CP violation and experiment*, Z. Phys. **C29** (1985) 491.

[53] E. Schrödinger, *Quantisierung als Eigenwertproblem*, Annalen der Physik **384** (1926) 361.

[54] V. Weisskopf and E. Wigner, *Berechnung der natürlichen Linienbreite auf Grund der Diracschen Lichttheorie*, Z. Phys. **63** (1930) 54.

[55] V. Weisskopf and E. Wigner, *Über die natürliche Linienbreite in der Strahlung des harmonischen Oszillators*, Z. Phys. **65** (1930) 18.

[56] NA48, V. Fanti *et al.*, *A new measurement of direct CP violation in two pion decays of the neutral kaon*, Phys. Lett. B **465** (1999) 335, `arXiv:hep-ex/9909022`.

[57] LHCb collaboration, R. Aaij *et al.*, *Observation of CP violation in charm decays*, Phys. Rev. Lett. **122** (2019) 211803, `arXiv:1903.08726`.

[58] P. Frings, U. Nierste, and M. Wiebusch, *Penguin contributions to CP phases in $B_{d,s}$ decays to charmonium*, Phys. Rev. Lett. **115** (2015) 061802, `arXiv:1503.00859`.

[59] M. Z. Barel, K. De Bruyn, R. Fleischer, and E. Malami, *In pursuit of new physics with $B_d^0 \to J/\psi K^0$ and $B_s^0 \to J/\psi\phi$ decays at the high-precision frontier*, J. Phys. G **48** (2021) 065002, `arXiv:2010.14423`.

[60] K. De Bruyn and R. Fleischer, *A roadmap to control penguin effects in $B_d^0 \to J/\psi K_S^0$ and $B_s^0 \to J/\psi\phi$*, JHEP **03** (2015) 145, `arXiv:1412.6834`.

[61] B. Aubert *et al.*, *The babar detector*, Nuclear Instruments and Methods in Physics Research Section A: Accelerators, Spectrometers, Detectors and Associated Equipment **479** (2002) 1, Detectors for Asymmetric B-factories.

[62] A. Abashian *et al.*, *The belle detector*, Nuclear Instruments and Methods in Physics Research Section A: Accelerators, Spectrometers, Detectors and Associated Equipment **479** (2002) 117, Detectors for Asymmetric B-factories.

[63] Belle-II, T. Abe *et al.*, *Belle II Technical Design Report*, `arXiv:1011.0352`.

[64] CKMfitter group, J. Charles *et al.*, *Current status of the standard model CKM fit and constraints on $\Delta F = 2$ new physics*, Phys. Rev. **D91** (2015) 073007, `arXiv:1501.05013`, updated results and plots available at `http://ckmfitter.in2p3.fr/`.

[65] BaBar collaboration, J. P. Lees *et al.*, *Measurement of CP asymmetries and branching fractions in charmless two-body B-meson decays to pions and kaons*, Phys. Rev. **D87** (2013) 052009, `arXiv:1206.3525`.

[66] Belle collaboration, I. Adachi *et al.*, *Measurement of the CP violation parameters in $B^0 \to \pi^+\pi^-$ decays*, Phys. Rev. **D88** (2013) 092003, `arXiv:1302.0551`.

[67] LHCb collaboration, R. Aaij *et al.*, *First measurement of time-dependent CP violation in $B_s^0 \to K^+K^-$ decays*, JHEP **10** (2013) 183, `arXiv:1308.1428`.

[68] LHCb collaboration, R. Aaij *et al.*, *Measurement of the CKM angle γ in $B^\pm \to DK^\pm$ and $B^\pm \to D\pi^\pm$ decays with $D \to K_S^0 h^+h^-$*, JHEP **02** (2021) 0169, `arXiv:2010.08483`.

[69] LHCb collaboration, R. Aaij *et al.*, *Measurement of CP asymmetry in $B_s^0 \to D_s^\mp K^\pm$ decays*, JHEP **03** (2018) 059, `arXiv:1712.07428`.

[70] LHCb collaboration, R. Aaij *et al.*, *First observation of the decay $B_s^0 \to K^-\mu^+\nu_\mu$ and measurement of $|V_{ub}|/|V_{cb}|$*, Phys. Rev. Lett. **126** (2021) 081804, `arXiv:2012.05143`.

[71] LHCb collaboration, R. Aaij *et al.*, *Precise determination of the $B_s^0-\bar{B}_s^0$ oscillation frequency*, Nature Physics **18** (2022) 1, `arXiv:2104.04421`.

[72] ATLAS Collaboration, G. Aad *et al.*, *The ATLAS experiment at the CERN Large Hadron Collider*, JINST **3** (2008) S08003.

[73] ALICE Collaboration, K. Aamodt *et al.*, *The ALICE experiment at the CERN LHC*, JINST **3** (2008) S08002.

[74] CMS Collaboration, S. Chatrchyan *et al.*, *The CMS experiment at the CERN LHC*, JINST **3** (2008) S08004.

[75] LHCb collaboration, A. A. Alves Jr. *et al.*, *The LHCb detector at the LHC*, JINST **3** (2008) S08005.

[76] LHCb collaboration, *LHCb VELO (VErtex LOcator): Technical Design Report*, CERN-LHCC-2001-011.

[77] R. Aaij *et al.*, *Performance of the LHCb Vertex Locator*, JINST **9** (2014) P09007, `arXiv:1405.7808`.

[78] D. Francesca, *LHCb detector and trigger performance in Run II*, EPJ Web of Conferences **164** (2017) 01016.

[79] LHCb collaboration, *LHCb reoptimized detector design and performance: Technical Design Report*, CERN-LHCC-2003-030.

[80] LHCb collaboration, R. Aaij *et al.*, *LHCb detector performance*, Int. J. Mod. Phys. **A30** (2015) 1530022, `arXiv:1412.6352`.

[81] LHCb collaboration, *LHCb magnet: Technical Design Report*, CERN-LHCC-2000-007.

[82] LHCb collaboration, *LHCb inner tracker: Technical Design Report*, CERN-LHCC-2002-029.

[83] P. d'Argent *et al.*, *Improved performance of the LHCb Outer Tracker in LHC Run 2*, JINST **12** (2017) P11016, `arXiv:1708.00819`.

[84] M. Adinolfi *et al.*, *Performance of the LHCb RICH detector at the LHC*, Eur. Phys. J. **C73** (2013) 2431, `arXiv:1211.6759`.

[85] F. P. Albicocco *et al.*, *Long-term operation of the multi-wire-proportional-chambers of the LHCb muon system*, Journal of Instrumentation **14** (2019) P11031.

[86] C. Abellan Beteta *et al.*, *Calibration and performance of the LHCb calorimeters in Run 1 and 2 at the LHC*, `arXiv:2008.11556`, submitted to JINST.

[87] C. Coca *et al.*, *The hadron calorimeter prototype beam-test results*, tech. rep., CERN, Geneva, Oct, 2000.

[88] The LHCb Collaboration, *Tracking strategies used in LHCb*, `https://twiki.cern.ch/twiki/bin/view/LHCb/LHCbTrackingStrategies`, Sep, 2022.

[89] R. Aaij *et al.*, *Design and Performance of the LHCb trigger and full real-time reconstruction in Run 2 of the LHC*, JINST **14** (2019) P04013, `arXiv:1812.10790`.

[90] T. Sjöstrand, S. Mrenna, and P. Skands, *PYTHIA 6.4 physics and manual*, JHEP **05** (2006) 026, `arXiv:hep-ph/0603175`.

[91] T. Sjöstrand, S. Mrenna, and P. Skands, *A brief introduction to PYTHIA 8.1*, Comput. Phys. Commun. **178** (2008) 852, `arXiv:0710.3820`.

[92] I. Belyaev *et al.*, *Handling of the generation of primary events in Gauss, the LHCb simulation framework*, J. Phys. Conf. Ser. **331** (2011) 032047.

[93] D. J. Lange, *The EvtGen particle decay simulation package*, Nucl. Instrum. Meth. **A462** (2001) 152.

[94] P. Golonka and Z. Was, *PHOTOS Monte Carlo: A precision tool for QED corrections in Z and W decays*, Eur. Phys. J. **C45** (2006) 97, `arXiv:hep-ph/0506026`.

[95] N. Davidson, T. Przedzinski, and Z. Was, *PHOTOS interface in C++: Technical and physics documentation*, Comp. Phys. Comm. **199** (2016) 86, `arXiv:1011.0937`.

[96] Geant4 collaboration, S. Agostinelli *et al.*, *Geant4: A simulation toolkit*, Nucl. Instrum. Meth. **A506** (2003) 250.

[97] Geant4 collaboration, J. Allison *et al.*, *Geant4 developments and applications*, IEEE Trans. Nucl. Sci. **53** (2006) 270.

[98] R. Aaij *et al.*, *The Moore project*, `https://lhcbdoc.web.cern.ch/lhcbdoc/moore/`, Sep, 2022.

[99] R. Aaij *et al.*, *The Brunel project*, `http://lhcbdoc.web.cern.ch/lhcbdoc/brunel/`, Sep, 2022.

[100] R. Aaij *et al.*, *The DaVinci project*, `https://lhcbdoc.web.cern.ch/lhcbdoc/davinci/`, Sep, 2022.

[101] W. D. Hulsbergen, *Decay chain fitting with a Kalman filter*, Nucl. Instrum. Meth. **A552** (2005) 566, `arXiv:physics/0503191`.

[102] T. Chen and C. Guestrin, *XGBoost: A scalable tree boosting system*, in *Proceedings of the 22nd ACM SIGKDD International Conference on Knowledge Discovery and Data Mining*, KDD '16, (New York, NY, USA), pp. 785–794, ACM, 2016. doi: 10.1145/2939672.2939785.

[103] A. Bevan, R. G. Goñi, T. Stevenson, and T. Stevenson, *Support vector machines and generalisation in HEP*, J. Phys. Conf. Ser. **898** (2017) 072021, `arXiv:1702.04686`.

[104] M. Pivk and F. R. Le Diberder, *sPlot: A statistical tool to unfold data distributions*, Nucl. Instrum. Meth. **A555** (2005) 356, `arXiv:physics/0402083`.

[105] Y. Xie, *sFit: A method for background subtraction in maximum likelihood fit*, `arXiv:0905.0724`.

[106] M. Paterno, *Calculating efficiencies and their uncertainties*, .

[107] D. Martínez Santos and F. Dupertuis, *Mass distributions marginalized over per-event errors*, Nucl. Instrum. Meth. **A764** (2014) 150, `arXiv:1312.5000`.

[108] G. A. Cowan, D. C. Craik, and M. D. Needham, *RapidSim: An application for the fast simulation of heavy-quark hadron decays*, Comput. Phys. Commun. **214** (2017) 239, `arXiv:1612.07489`.

[109] C. de Boor, *A practical guide to splines*, vol. 27 of *Applied Mathematical Sciences*, Springer-Verlag New York, 1978.

[110] S. P. Venkateshan and P. Swaminathan, *Chapter 5 - interpolation*, in *Computational Methods in Engineering* (S. P. Venkateshan and P. Swaminathan, eds.), pp. 213–254. Academic Press, Boston, 2014. doi: https://doi.org/10.1016/B978-0-12-416702-5.50005-3.

[111] LHCb collaboration, R. Aaij *et al.*, *Measurements of the B^+, B^0, B^0_s meson and Λ^0_b baryon lifetimes*, JHEP **04** (2014) 114, `arXiv:1402.2554`.

[112] K. Heinicke, *Optimization of Flavour Tagging Algorithms for the LHCb Experiment*, Master's thesis, Technische Universität Dortmund, 2016.

[113] K. Heinicke, *Strange oscillating beauty-mesons*, PhD thesis, Technische Universität Dortmund, 2021, doi: http://dx.doi.org/10.17877/DE290R-22378.

[114] Q. Führing and V. Jevtić, *lhcb-ftcalib: LHCb Flavour Tagging calibration software*, , `https://gitlab.cern.ch/lhcb-ft/lhcb_ftcalib`.

[115] T. Skwarnicki, *A study of the radiative cascade transitions between the Upsilon-prime and Upsilon resonances*, PhD thesis, Institute of Nuclear Physics, Krakow, 1986, DESY-F31-86-02.

[116] A. Rogozhnikov, *Reweighting with Boosted Decision Trees*, J. Phys. Conf. Ser. **762** (2016) 012036, `arXiv:1608.05806`, `https://github.com/arogozhnikov/hep_ml`.

[117] R. E. Bellmann, *Dynamic Programming*, Dover Publications, Inc., USA, 2003.

[118] Heavy Flavor Averaging Group, Y. Amhis *et al.*, *Averages of b-hadron, c-hadron, and τ-lepton properties as of 2018*, Eur. Phys. J. **C81** (2021) 226, `arXiv:1909.12524`, updated results and plots available at `https://hflav.web.cern.ch`.

[119] LHCb collaboration, R. Aaij *et al.*, *Measurement of B^0, B_s^0, B^+ and Λ_b^0 production asymmetries in 7 and 8 TeV proton-proton collisions*, Phys. Lett. **B774** (2017) 139, `arXiv:1703.08464`.

[120] M. Kenzie *et al.*, *GammaCombo: A statistical analysis framework for combining measurements, fitting datasets and producing confidence intervals*, doi: 10.5281/zenodo.3371421.

[121] LHCb collaboration, *LHCb Framework TDR for the LHCb Upgrade II Opportunities in flavour physics, and beyond, in the HL-LHC era*, CERN-LHCC-2021-012.

Danksagung

Ich möchte zuerst Professor Spaan danken, dass er mir die Möglichkeit gab, meine Doktorarbeit bei ihm zu schreiben. Es ist sehr traurig, dass er zu früh von uns gegangen ist. Die hilfreichen Diskussionen und Anregungen waren immer sehr willkommen. Des Weiteren möchte ich mich bei Johannes Albrecht bedanken, der sich bereit erklärt hat, die Betreuung zu übernehmen und in der turbulenten Zeit so vieles möglich gemacht hat. So musste ich mir keine großen Sorgen um die Finanzierung und auch um die Verlängerung meines Vertrags machen.

Meiner Zweitgutachterin Chris Delitzsch möchte ich ebenfalls danken, für die einfache und unkomplizierte Zusammenarbeit und Kommunikation. Meiner Prüfungskommission mit Herrn Hövel und Herrn Sternemann möchte ich für die Arbeit und die schnelle Terminfindung bei der Disputation danken.

Natürlich kann auch keine Arbeit ohne die Unterstützung von Freunden, Kollegen und Familie geschafft werden. Da gilt mein Dank allen in der Arbeitsgruppe in der Uni. Die lockere und nette Arbeitsatmosphäre hat mir immer viel Spaß gemacht und das Arbeiten auch an stressigen Tagen vereinfacht. Ohne eure viele Arbeit beim Lesen und Kommentaregeben meines Aufschriebs wären viele weitere holprige Stellen im Text verblieben. Der Bullshit Talk auf dem Weg in die Mensa und die vielen Traditionen werden mir auf jeden Fall in Erinnerung bleiben.

Besonders gilt mein Dank meinen direkten Bürokollegen zu früheren Zeiten mit Maggi, Philipp, Martin, Holger und Patrick wie auch später mit Maik, Quentin und Vukan. Ihr habt das Arbeiten im Büro verschönert, was mir während der Coronazeit sehr gefehlt hat.

Die Analyse in der Doktorarbeit habe ich in enger Kooperation zusammen mit Patrick und Vukan absolviert. Für die gegenseitige Hilfe jederzeit möchte ich mich bei euch bedanken. Es war mir eine Freude mit euch zusammen zu arbeiten.

Als ich neu nach Dortmund für den Masterstudiengang gekommen bin, kannte ich noch keinen, aber ich hatte das Glück schnell eine Freundesgruppe zu finden. Da gilt mein Dank Tim, Mario, Vanessa, Jasmin, Felix und Nico. Ohne eure Hilfe hätte ich es wahrscheinlich nicht geschafft alle meine Prüfungen im Master und später auch meine Doktorarbeit zu absolvieren. An die 2 Wochen ”leben wie der Durchschnittsstudentünd die gemeinsamen Urlaube denke ich mit Freude zurück.

Für die Zeit im Fitnessstudio möchte ich mich bei Nico bedanken. Einen besseren, verrückteren Trainingspartner hätte ich mir nicht vorstellen können. Bei Maik bedanke ich mich für die große Hilfe beim Umzug und die Spaziergänge zur Galerie, um den Kopf frei zu bekommen.

Den letzten Teil meiner Arbeit musste ich schreiben, als ich bereits in Braunschweig gearbeitet habe. Daher gilt mein Dank auch der Arbeitsgruppe im Speziellen

mit Moritz, Calvin, Noria und Christopher, die mir beim Einarbeiten in das neue Thema der Kometenforschung geholfen haben und die auch mal langweiligere Arbeiten auflockern. Christopher danke ich nochmals besonders, für das Jobangebot und die vielen Abende mit einem guten Wein.

Am Ende danke ich meiner Familie für die große Unterstützung zu jeder Zeit, die mir die Sicherheit gegeben hat, mich auf meine Arbeit konzentrieren zu können. Ohne euch hätte ich nicht meinen Hobbys als Ausgleich von der Arbeit so gut nachgehen können. Danke dass ich euch habe.